

Electronic Thesis and Dissertation Repository

4-2-2015 12:00 AM

Methods and Results Toward Measuring Magnetic Fields in Star-Forming Regions

Scott C. Jones, *The University of Western Ontario*

Supervisor: Martin Houde, *The University of Western Ontario*

A thesis submitted in partial fulfillment of the requirements for the Doctor of Philosophy degree in Astronomy

© Scott C. Jones 2015

Follow this and additional works at: <https://ir.lib.uwo.ca/etd>



Part of the [Instrumentation Commons](#), [Physical Processes Commons](#), and the [Stars, Interstellar Medium and the Galaxy Commons](#)

Recommended Citation

Jones, Scott C., "Methods and Results Toward Measuring Magnetic Fields in Star-Forming Regions" (2015). *Electronic Thesis and Dissertation Repository*. 2718.
<https://ir.lib.uwo.ca/etd/2718>

This Dissertation/Thesis is brought to you for free and open access by Scholarship@Western. It has been accepted for inclusion in Electronic Thesis and Dissertation Repository by an authorized administrator of Scholarship@Western. For more information, please contact wlsadmin@uwo.ca.

METHODS AND RESULTS TOWARD
MEASURING MAGNETIC FIELDS IN
STAR-FORMING REGIONS

(THESIS FORMAT: INTEGRATED-ARTICLE)

by

Scott Jones

Faculty of Science
Department of Physics and Astronomy

Submitted in partial fulfillment
of the requirements for the degree of
Doctor of Philosophy

School of Graduate and Postdoctoral Studies
The University of Western Ontario
London, Ontario, Canada
April, 2015

© Scott Jones 2015

Abstract

Star formation is a fundamental process in the evolution of the cosmos. Yet given the abundance of stellar constituents, it remains preeminent as to why the number of stars is not correspondingly large. If we cannot satisfactorily explain how stars are formed, then many further avenues of research are hindered.

This thesis furthers means to probe one of the foremost theories as to the relative lack of stars, interstellar magnetic fields. These fields have been observationally verified on multiple scales. I will use the most direct method to probe magnetic fields in known star-forming regions, polarization, at millimetre/submillimetre wavelengths. In particular I will focus on the effect that magnetic fields have on the emission produced by rotational molecular transitions.

Much of the background behind the study of magnetic fields, and their deduction through submillimetre polarimetry, will be developed in Chapter 1. Here I provide an overview of not only the role that magnetic fields may play in star formation, but also the competing theories of turbulence and magnetohydrodynamic waves. The various manifestations of polarization will also be covered, including polarized molecular transitions.

Chapter 2 will look at one of the most well-studied star-forming regions, Orion KL, through observations of a newly discovered water maser transition at 620.701 GHz. Interstellar masers allow different environments to be probed, regions where more complex activity has created a population imbalance between rotational energy levels.

The remaining two chapters will present methods and data from the Four-Stokes-Parameter Spectral-Line Polarimeter at the Caltech Submillimeter Observatory. I will look at considerations that must be made when a small map is collected by way of quantifying the amount of instrumental polarization. Spurious polarization signals

may pervade the outer edges of the telescope beam, leading to a misrepresentation of the true amount of source polarization. Chapter 3 details the methods involved in removing sidelobes plus the other sources of instrumental polarization, while Chapter 4 goes on to present the actual data to which these techniques have been applied. The data itself is of the molecular transition ^{12}CO ($J = 2 \rightarrow 1$), prominent within the protostellar source OMC-2 FIR 4.

Keywords: Magnetic fields, Star formation, Astronomical Instrumentation, Submillimetre, Orion Molecular Cloud

Co-Authorship

The majority of the work comprising this thesis either has already been, or will soon be published in a peer-reviewed journal. These papers could not have been possible without the efforts of their respective co-authors, which I must here acknowledge.

An incarnation of Chapter 2 has appeared in the *Astronomy and Astrophysics* journal, volume 567, as of July 2014. The data presented there was made available to us courtesy of Prof. Martin Harwit, Cornell University, who has dedicated much of his Guaranteed Observing Time as the *Herschel*/HIFI Mission Scientist to this project. The science inspiration came from a previous paper by Harwit, M., Houde, M., et al. (2010, *A&A*, 521, L51), who made the first astronomical detection of the 621 GHz maser transition of ortho water vapour in oxygen-rich supergiant star VY Canis Majoris. Dr. Harwit also provided invaluable guidance during the creation of the paper, frequently facilitating helpful communication with the remainder of the co-authorship.

While it is not anticipated that Chapter 3 will attempt to be published, the results that it inspired in Chapter 4 will soon be submitted to the *Astrophysical Journal*. This paper will be co-authored with Martin Houde and Talayeh Hezareh, who first built FSPPol and described its construction and operation in a follow-up paper in 2010 with Dr. Houde. Certainly the methods that we used towards removing the instrumental polarization were heavily based upon a similar technique employed by Dr. Hezareh in her 2013 paper of Non-Zeeman circular polarization measurements in SNR IC 443.

Acknowledgements

There were many key contributors to this thesis without whose assistance this work could never have come to fruition. I must first and foremost thank my supervisor, Dr. Martin Houde, who provided patient guidance and support through each of the projects that make up this work. His input significantly enhanced the scientific merit of the final product, while his experience during the many observing runs was essential. There were many people who made sure these runs went smoothly, including Diana Bisel, Simon Radford, Ed Bupil, Allen Guyer, Pat Nelson and Hiroshige Yoshida at the CSO, while Hiroko Shinnaga, Ruisheng Peng, Darren Dowell, John Vaillancourt, Giles Novak, Nicholas Chapman, Tyler Desjardins, Lisa May Walker, Maryam Tabeshian, Dave Stock and Cam Wipper assisted with the observations. Special thanks also go to Martin Harwit, Carolyn M^cCoey and Talayeh Hezareh on whose previous work I built on extensively and each of whom were always very keen to answer pertinent questions.

I must also thank the members of my supervisory committee at Western, Aaron Sigut and John Landstreet, who kept me honest at all of my committee meetings. The front office staff, particularly Clara Buma, Jodi Guthrie and Jackie McLean, were always most eager to help me with anything relevant to my time as a student.

Finally, a nod to all of the members of the Conspiracy, with whom many an evening of treachery and intrigue were shared during times not devoted to my thesis.

Contents

Abstract	ii
Co-authorship	iv
Acknowledgements	v
Contents	vi
List of Tables	x
List of Figures	xi
List of Abbreviations	xiii
1 Introduction	1
1.1 Molecular Clouds	1
1.1.1 Clumps and Cores	3
1.2 Support Mechanisms	4
1.2.1 Turbulence	4
1.2.2 Magnetic Fields	6
1.2.3 Magnetohydrodynamic (MHD) Waves	7
1.2.4 Ambipolar Diffusion	10
1.3 Polarimetric Methods	11
1.3.1 Stokes Parameters	13

1.3.1.1	Stokes I	13
1.3.1.2	Stokes Q	13
1.3.1.3	Stokes U	14
1.3.1.4	Stokes V	14
1.3.1.5	Normalized Stokes Parameters	15
1.3.2	Dust Polarization	16
1.3.3	Zeeman Effect	18
1.3.4	Goldreich-Kylafis Effect	24
1.3.5	Chandrasekhar-Fermi (CF) Method	26
1.4	Conclusion	30
	Bibliography	31
2	Polarisation Observations of $\text{H}_2\text{O } J_{K_{-1}K_1} = 5_{32} - 4_{41}$ 620.701 GHz	
	Maser Emission with HERSCHEL/HIFI in Orion KL	34
2.1	Introduction	34
2.2	Observations	36
2.2.1	HIFI Observations	36
2.2.2	Effelsberg Observations	38
2.3	Methods/Results	38
2.3.1	Polarisation Analysis	38
2.3.2	HIFI data	39
2.3.2.1	Pointing Effects on Maser Polarisation Measurements	41
2.3.3	22 GHz (Effelsberg) Data	43
2.4	Conclusion	44
3	Methods Toward Recovering a Polarization Signal from the Four-	
	Stokes-Parameters Spectral-Line Polarimeter	48
3.1	Introduction	48

3.2	The Four-Stokes-Parameter Spectral-Line Polarimeter (FSPPol) . . .	50
3.2.1	Instrumental Polarization	55
3.3	Description of the Simulations	58
3.4	Correcting for Spurious Forms of Polarization	59
3.4.1	Reduction of Beam Squint through Map Alignment	59
3.4.2	Removing Other Forms of Instrumental Polarization	65
3.4.2.1	Simulating IP Removal	69
3.5	Conclusion	77
	Bibliography	79
4	The Detection of Non-Zeeman Circular Polarization of CO Rotational Lines in OMC-2 FIR 4¹	82
4.1	Introduction	82
4.2	Observations	85
4.2.1	OMC-2 FIR 4	87
4.3	Data Processing	88
4.4	Results	92
4.5	Discussion	94
4.6	Conclusion	104
5	Conclusion and Future Plans	108
A	Summary of Herschel/HIFI and Effelsberg Observations	112
B	Herschel/HIFI Maps of 621 GHz Water Maser	115
C	Discussion on Pointing Errors	118
D	Polarization of HCN	121

¹From Jones, S. C., Houde, M., and Hezareh, T. 2015, ApJ, to be submitted

List of Tables

1.1	Observed Zeeman Effect Line Intensities (Crutcher et al. 1993)	21
3.1	Summary of simulation results for removal of remaining types of instrumental polarization.	75
A.1	Summary of HIFI observations conducted in 2011 and 2012.	113
A.2	Summary of Effelsberg observations conducted in 2011 and 2012. . . .	114

List of Figures

1.1	A schematic of the polarization states for a Zeeman split molecule. . .	21
1.2	Polarimetric map of OMC-1.	28
2.1	Stokes I (top) and the polarised flux pI (bottom) for the 621 GHz water maser line based on an analysis of all six epochs combined. . .	42
2.2	Polarisation properties of the 22 GHz water maser transition as measured at Effelsberg on 21 March 2011.	45
3.1	Schematic of FSPPol within the elevation tube of the CSO.	52
3.2	Schematic of the CSO telescope and the propagation of the beam through the associated optics.	53
3.3	Angles used to measure the polarization state of incoming radiation at the CSO.	54
3.4	Stokes I contours measured at the Arecibo telescope by Heiles et al. (2001a).	57
3.5	Illustration of the alignment of a Stokes V signal with $\simeq 3''$ pointing errors.	63
3.6	Effect of pointing corrections on an unpolarized source.	65
3.7	Sequence of products from simulations to establish the amount of instrumental polarization.	71
3.8	Footprint of simulated data both prior to and after zero-padding. . .	73
3.9	Final two products in attempt to recover 2% polarization from a simulated source.	74

3.10	Variation of polarization levels for a simulated source with R.A. position.	76
3.11	Stokes I and V spectra for a simulated source upon removal of all sources of IP.	78
4.1	Stokes I and V intensity maps for the unpolarized standard, Jupiter.	91
4.2	Stokes I and V polarization maps for OMC-2 FIR 4.	93
4.3	Instrumental polarization map retrieved from the convolution of Jupiter's Stokes V with the Stokes I of OMC-2 FIR 4.	95
4.4	Stokes I and V polarization spectra for a single position from the OMC-2 FIR 4 intensity maps.	96
4.5	Stokes I spectra at each offset position from OMC-2 FIR 4, along with points of detected circular polarization.	97
4.6	Stokes V spectra for each offset position from OMC-2 FIR 4.	98
4.7	Symmetric circular polarization spectra for the ^{12}CO ($J = 2 \rightarrow 1$) transition as rendered by the anisotropic resonant scattering model of Houde et al. (2013).	102
4.8	Antisymmetric circular polarization spectra for the ^{12}CO ($J = 2 \rightarrow 1$) transition as rendered by the anisotropic resonant scattering model of Houde et al. (2013).	103
B.1	Map of 621 GHz emission, measured with HIFI, corresponding to dataset 2-H in TableA.1	116
B.2	Same as Figure B.1 but for dataset 6b-H in Table A.1.	117
D.1	Variation in the wide-band HCN spectrum from 2011 to 2012, as measured with HIFI	122

List of Abbreviations

ALMA	Atacama Large Millimetre Array
AP	Artificial Polarization
APE	Absolute Pointing Error
CCAT	Cerro Chajnantor Atacama Telescope
CF	Chandrasekhar-Fermi
CSO	Caltech Submillimetre Observatory
DEC	Declination
DMC	Dwarf Molecular Cloud
FIR	Far InfraRed
FSPPol	Four-Stokes-Parameter Spectral-Line Polarimeter
FWHM	Full-Width-Half-Magnitude
GMC	Giant Molecular Cloud
HEXOS	<i>Herschel</i> /HIFI Observations of EXtraordinary Sources
HIFI	Heterodyne Instrument for the Far Infrared
HIPE	<i>Herschel</i> Interactive Processing Environment
HPBW	Half-Power Beam-Width
HRS	High-Resolution Spectrometer
HWP	Half-Wave Plate
IP	Instrumental Polarization
IRAM	Institut de Radioastronomie Millimétrique
ISM	InterStellar Medium
JCMT	James Clerk Maxwell Telescope
LCP	Left-Circularly Polarized
LOS	Line-Of-Sight
LSR	Local Standard of Rest
LVG	Large Velocity Gradient
MHD	MagnetoHydroDynamics

MPIfR	Max-Planck-Institut für Radioastronomie
NRAO	National Radio Astronomy Observatory
OMC	Orion Molecular Cloud
OTF	On-The-Fly
PA	Position/Polarization Angle
pI	polarization Intensity
POS	Plane-Of-Sky
QWP	Quarter-Wave Plate
RA	Right Ascension
RAT	Radiative Alignment Torque
RCP	Right-Circularly Polarized
SCUBA-2	Submillimetre Common-User Bolometer Array-2
SED	Spectral Energy Distribution
SMM	Submillimetre/Millimetre
SNR	Supernova Remnant
WBS	Wide-Band Spectrometer

Chapter 1

Introduction

The fundamental process of star formation, although crucially important in the evolution of our Galaxy, remains a topic of controversy. Furthermore, a comprehensive theory is paramount to unraveling countless other mysteries of the Universe. The recycling that occurs as interstellar gas coalesces into a fledgling star before being expelled upon its death impacts heavily upon the constitutive elements of the intervening interstellar medium (ISM). These are the same elements that may have been present immediately after the Big Bang, and that drive galactic evolution. Additionally, there is strong evidence for the creation of planetary bodies in the accretionary disk of forming stars. For all the prevailing theories and observational effort, astronomers remain humbled in the breadth of their knowledge of the most basic building block in astronomy.

1.1 Molecular Clouds

The star formation scenario unfolds deep within large, dense complexes of molecular gas called clouds (Crutcher et al. 1993). These, in turn, can be further subdivided into diffuse molecular clouds (DMCs), giant molecular clouds (GMCs) and dark clouds or

complexes with high visual extinction. Of these, DMCs never produce any stars, while dark clouds harbour dense cores or so-called Bok globules, where nascent protostars have been observed. Giant molecular clouds are the most massive and therefore rely on their own self-gravity to constrain their large gas content. While the defining properties of GMCs are often fuzzy, it is typically assumed that they require a mass of $\sim 10^5 M_{\odot}$, a volume of $\sim 10^5 \text{ pc}^3$ and a mean column density of $3 - 6 \times 10^{21} \text{ cm}^{-2}$ (Levy 1993). Their distribution is preferential to the spiral arms of our Galaxy and is further influenced by stellar winds and shocks that sweep up the gas. The molecular composition of the clouds can be largely determined from rotational spectroscopy, which in turn can allow the study of other physical conditions (Tielens 2005). For one, molecular clouds are extremely cold ($\sim 10 \text{ K}$ on average), such that thermal pressure is only a mild factor in the dynamic pressure balance of the cloud. Rather, some other mechanism(s) must be responsible for opposing the gravitational force of contraction, and maintaining a force equilibrium in those structures without any embedded stars or stellar precursors (Stahler & Palla 2004). The primary constituent in these regions is molecular hydrogen; it is not until the later stages of the star's evolution that heavier elements begin production.

During their lifetime of some 3×10^7 years, about 3 percent of the mass of a molecular cloud is used to create stars (Stahler & Palla 2004). Given the total H_2 content of the Galactic disk ($2 \times 10^9 M_{\odot}$), this is equivalent to a star formation rate of approximately $2 M_{\odot} \text{ yr}^{-1}$. The large majority of giant molecular clouds are formed in the plane of the Galaxy, where self-shielding from ultraviolet radiation permits the accumulation of molecular clumps. Among these GMCs, most will eventually form O or B stars and associations, whose resulting radiation ultimately leads to the dispersal of the clouds themselves. In particular there is a strong trend toward decreasing molecular mass in the regions surrounding massive stars/star clusters with the age of the cluster (see Figure 3.8 of Stahler et al., 2004). Nevertheless, for reasons

that will be discussed imminently, the star formation rate continues to be much less than would be expected given the abundance of molecular hydrogen in the Milky Way.

1.1.1 Clumps and Cores

Within any molecular cloud there exists a series of local density enhancements known as clumps. Characterized by their larger column densities and optical depths, it is essentially a set of clumps embedded in an interclump medium that collectively comprise a molecular cloud. Most of the inferences of the structure of a cloud require an optically thin molecule (optical depth $\Delta\tau_\nu \ll 1$), often taken to be ^{13}CO . Containing most of the cloud's hydrogen, clumps have mean H_2 densities of $\sim 10^2 - 10^3 \text{ cm}^{-3}$, while their mass distribution is thought to obey a relationship $M \propto R^{2.5}$ (Carr 1987) that appears to be independent of the cloud under study (Levy 1993).

There is a further division of density structure within clumps which inevitably hosts the star formation process. These highest density regions are known as *cores*. Using ammonia as a tracer, sensitive to a density of $n_{\text{H}_2} \sim 10^4 \text{ cm}^{-3}$, cores are thought to have masses of $\sim 1 M_\odot$, sizes of about 10^{-1} pc , and equivalent temperatures of approximately 10 K. Embedded protostars within these cores can be identified from their spectral energy distribution (SED), or as they blow out their surrounding envelopes (Shu et al. 1987). Theoretically, there is a critical value above which gravitational collapse becomes unavoidable. These cores are called *supercritical* ($M_{\text{core}} > M_{\text{cr}}$). Together with the opposite scenario, whereby $M_{\text{core}} < M_{\text{cr}}$, termed the *subcritical* regime, it is clear that there must be competing forces at play within these stellar nurseries. While the concept of self-gravitation is easily understood, it was realized early on that thermal forces alone were not sufficient to sustain an equilibrium.

1.2 Support Mechanisms

In order for a gaseous complex to be stable, it must obey the relation

$$2\mathcal{T} + 2U + \mathcal{W} + \mathcal{M} = 0, \quad (1.1)$$

where \mathcal{T} is the total kinetic energy of the ensemble, U is the thermal energy of random motion, \mathcal{W} is the gravitational potential energy and \mathcal{M} is the energy contained within the magnetic field. The energy working to contract the mass, \mathcal{W} , must be balanced by those sources that provide support. Such would lead to what is called “virial equilibrium”. If the critical mass M_{cr} of a clump or core is less than the mass of the object, then gravitational collapse should occur on free-fall timescales. However the number of observed stars is much too low in order for this to be the case. Instead, if one or some of rotation, magnetic fields or turbulence provide sufficient support, then $M < M_{\text{cr}}$. In this thesis I will focus most heavily on the latter two support mechanisms.

1.2.1 Turbulence

A turbulent fluid can be thought of as any that exhibits random fluctuations in its flow over time. At the same time this definition is somewhat contradictory, as turbulent flows are often manifestations of small-scale irregularities propagated onto a larger, more systematic motion scale (Larson 1981). Such a fluid can be further qualified as either compressible or incompressible, regimes in which completely different theoretical treatments are required. These distinctions will be qualified later in this section.

Detailed study into turbulence in the ISM was initiated by the discovery of spectral line widths too wide to be fully accounted for by thermal motions. This result is

strengthened by Larson (1981), who empirically determined the relation

$$\sigma \propto L^{0.38} \quad (1.2)$$

for velocity dispersion σ and cloud size L , across a range of length scales. Such a power-law dependence agrees well with that first identified by Kolmogorov (1941) for subsonic, incompressible and homogeneous turbulent flows, of $\sigma \propto L^{1/3}$. Whilst most of interstellar turbulence is supersonic, this agreement is nevertheless encouraging. In the supersonic realm, dissipation can occur at larger scales and hence a decrease in the amount of energy at the subsequent smaller scales would be expected. Indeed, this is reflected in the steeper slope of the Larson relation.

The Kolmogorov (1941) theory is best used to describe incompressible turbulence, which ably captures the basis of most terrestrial applications. In this model, energy dissipation occurs on the smallest length scales, after cascading down through eddies of decreasing size. If l is the interaction scale of gas within a clump, and v is the turbulent velocity, then the rate of energy loss will be proportional to v^3/l (Shu et al. 1987). As such, kinetic energy $E \propto v^2 \propto k^{-11/3}$ for wavenumber $k = 2\pi/\lambda$ (MacLow & Klessen 2004). There is no contribution from a density term because of the nature of incompressibility. On large scales energy injection is driven, while at the smallest scales the viscosity takes over and energy is dissipated in a more random fashion. In between is the so-called inertial range, where the flow can be studied independently of either driving or viscosity.

Turbulence in the ISM however, is in reality fundamentally different. Due to stellar winds, supernovae explosions and expanding HII regions, there are frequent density fluctuations and hence the turbulence is compressible. Among the major differences, shock waves are now capable of dissipating energy across much more disparate scale sizes. The suspected source of these shocks are supernovae. The time frame for

dissipation is estimated through numerical simulations as

$$t_{diss} \approx 0.5 \frac{d}{\sigma}, \quad (1.3)$$

where d is the cloud diameter and σ is defined as before (McKee & Ostriker 2007). Therefore, within the amount of time required to traverse the cloud, the crossing time, turbulence will have decayed. To continue to act as a viable support mechanism and thus prevent gravitational collapse, the turbulent motions will have to be constantly replenished.

1.2.2 Magnetic Fields

The existence of a pervasive magnetic field in the ISM is revealed by the polarization of starlight by intervening dust grains. The uniform alignment of the grains, to be expounded in Section 1.3.2, with their long axes perpendicular to the field, leads to enhanced absorption of the electric field vector of the radiation along this direction. What remains is to quantify the effect of the magnetic field term, \mathcal{M} , in Equation (1.1) versus the other support mechanisms. The ratio of the magnetic force strength to self-gravity is given by

$$\frac{\mathcal{M}}{|\mathcal{W}|} \equiv \frac{|\mathbf{B}|^2 R^3}{6\pi} \left(\frac{GM^2}{R} \right)^{-1} = 0.3 \left(\frac{B}{20\mu\text{G}} \right)^2 \left(\frac{R}{25\text{pc}} \right)^4 \left(\frac{M}{10^5 M_\odot} \right)^{-2} \quad (1.4)$$

for a magnetic field \mathbf{B} threading a spherical cloud of radius R and mass M (Stahler & Palla 2004). The representative B value in Equation (1.4) is an average over measurements from surrounding dark clouds, and towards the lower end of those values detected in warm HI complexes within giant clouds. Typically, the strength of B can range from 10 μG for cold, inactive clouds (Troland et al. 1996), to ~ 1

mG in the dense gas ($\sim 10^5 \text{ cm}^{-3}$) of GMCs (Tan et al. 2013). Clearly this is a non-negligible force that significantly impacts the star formation process. But how do we determine the magnitude of \mathbf{B} ? What mass is needed to overcome the support offered by a magnetic flux?

Inside a cloud, a magnetic field exerts a Lorentz force on all ions, while the neutral particles remain unaffected. Rather, their movement throughout the cloud is indirectly constrained through collisions with the ions, which are tied to the field lines. Therefore, as collapse is attempted, the magnetic field is compressed but otherwise largely unchanged. Contractions in a direction perpendicular to the field lines will be repelled with a force proportional to the strength of the field. To overcome a magnetic flux Φ_B , the necessary critical mass is (Mouschovias & Spitzer 1976)

$$M_{c\Phi} = \frac{c_1}{3\pi} \left(\frac{5}{G} \right)^{1/2} \Phi_B \equiv c_1 x M, \quad (1.5)$$

where c_1 and x are constants required to conform to the virial theorem. In other words, for $M < M_{c\Phi}$ the cloud is termed *subcritical* and the magnetic support will prevent any collapse. Some additional physical effect is required to divest the cloud from the field and overcome flux freezing (see Section 1.2.4). Similarly, if $M > M_{c\Phi}$ then collapse will proceed, despite the presence of Φ_B . Often a core will accumulate the requisite mass through annexation of a series of smaller cores. This can occur solely through gravitational interaction or as collisions occur between thermally active elements.

1.2.3 Magnetohydrodynamic (MHD) Waves

One of the main reasons why magnetic fields are so effective at preventing, or delaying, gravitational collapse is due to a phenomenon known as *flux freezing*. That is to say that magnetic field lines respond to all changes in the gaseous medium as if they were

tied to it, and the medium were tied to the field lines. One consequence of this is that as a magnetically supported cloud begins to coalesce and increase in density, the field lines are moved closer together, also increasing \mathbf{B} . Mathematically, flux freezing is expressed in the ideal MHD equation,

$$\frac{\partial \mathbf{B}}{\partial t} = \nabla \times (\mathbf{u} \times \mathbf{B}) \quad (1.6)$$

which follows from expressions for Ampère's, Ohm's and Faraday's laws and where \mathbf{u} is the local velocity of the neutral particles (Stahler & Palla 2004). If this equation holds, then the magnetic flux will not change over a period of time Δt , a result that proceeds directly from Gauss' law. At some point, the strength of the field must drop off prior to star formation. If, instead, magnetic flux is conserved throughout contraction, then eventually its magnitude would become much larger than in any fully formed star type. In reality, Equation (1.6) contains an additional term on the right-hand side

$$\frac{\partial \mathbf{B}}{\partial t} = \nabla \times (\mathbf{u} \times \mathbf{B}) - \nabla \times \left(\frac{c^2}{4\pi\sigma} \nabla \times \mathbf{B} \right), \quad (1.7)$$

where c is the speed of light in vacuum and σ is the electrical conductivity, to represent the effects of Ohmic dissipation. It turns out that in clumps within molecular clouds σ is very large, and therefore over the time scales of interest, Ohmic dissipation can be neglected. Some other means is required to offset flux freezing.

In weakly ionized plasmas, including molecular clouds, a full treatment of the diffusivity extends beyond the one extra term in Equation (1.7). Indeed, the complete rendition of Ohm's law appears as

$$\mathbf{E} = \frac{1}{c} \left[-\mathbf{u} \times \mathbf{B} + \frac{4\pi}{c} \left(\eta \mathbf{j} + \alpha \mathbf{j} \times \frac{\mathbf{B}}{B} + \beta \mathbf{j}_\perp \right) \right] \quad (1.8)$$

where \mathbf{j} and \mathbf{j}_\perp are the current density and its component perpendicular to \mathbf{B} , and η , α and β are the magnetic diffusivity (found in Equation (1.7)), Hall and Pederson coefficients, respectively (Li & Houde 2008). In GMCs, $\beta \gg \alpha \gg \eta$ and thus the Pederson coefficient is often named the effective magnetic diffusivity. This term is defined as

$$\beta = \frac{B^2}{4\pi n_i \mu \nu_i} \quad (1.9)$$

where n_i is the ion density and μ is the mean reduced mass for collisions involving ions and neutrals at the rate ν_i . When $\frac{4\pi}{c} \beta \mathbf{j}_\perp$ is greater than the convective term, $\mathbf{u} \times \mathbf{B}$, there will be a decoupling of the ions from the neutrals, a process known as *ambipolar diffusion* (see §1.2.4).

Additionally, flux freezing can transmit any irregularities in the thermal flow structure as deviations in the magnetic field. Magnetic tension, while attempting to restore the field orientation, will create waves that will travel along field lines. These are known as magnetohydrodynamic (MHD) waves. These create disturbances in the velocity field as well. As a result, there are two modes of MHD waves that need to be considered within the framework of the dispersion relation. Those that are propagated parallel to the velocity fluctuations (longitudinal) and those that run perpendicular (transverse). The latter results in a velocity V_A , the Alfvén velocity, defined as

$$V_A \equiv \left(\frac{B_0}{\sqrt{4\pi\rho_0}} \right), \quad (1.10)$$

where B_0 and ρ_0 are the mean magnetic field strength and density before perturbation, respectively. The support provided by MHD waves is the gradient of the pressure, where

$$P_{wave} = \frac{1}{16\pi} |\delta\mathbf{B}|^2 \quad (1.11)$$

for a perturbation in the magnetic field $\delta\mathbf{B}$. While we have quantified another source of support, Alfvén waves may ultimately disperse in a pseudo-random fashion, inciting comparison with models of turbulence. Recently, efforts have been made to measure the effects of MHD turbulence in dense clouds (Hildebrand et al. 2009; Houde et al. 2009, 2011)

1.2.4 Ambipolar Diffusion

The astrophysical community currently accepts the process of ion-neutral drift, or ambipolar diffusion, as the means by which magnetic support is dissipated. Electrons and ions are tied to the field, whereas neutral particles are only subject to gravity. Essentially, they will traverse the tethered magnetic field at a different speed than the charged particles, creating density enhancements that lower the critical mass needed for collapse (MacLow & Klessen 2004). The neutrals “drift” across with a speed $\mathbf{v}_{\text{drift}} = \mathbf{u}_i - \mathbf{u}$, which, when incorporated into Equation (1.6) leads to

$$\frac{\partial\mathbf{B}}{\partial t} = \nabla \times (\mathbf{u} \times \mathbf{B}) + \nabla \times (\mathbf{v}_{\text{drift}} \times \mathbf{B}). \quad (1.12)$$

In equilibrium, the Lorentz and drag forces must balance,

$$\frac{1}{4\pi}(\nabla \times \mathbf{B}) \times \mathbf{B} = \alpha\rho_i\rho_n\mathbf{v}_{\text{drift}} \quad (1.13)$$

where α is a coupling coefficient

$$\alpha = \langle\sigma v\rangle / (m_i + m_n) \quad (1.14)$$

insofar as m_i and m_n are the mean masses of the ions and neutrals, respectively, σ is the ion-neutral cross-section and ρ_i and ρ_n the densities (MacLow & Klessen 2004). Solving for the drift velocity $\mathbf{v}_{\text{drift}}$, and assuming a cloud of diameter L , a timescale

for ambipolar diffusion can then be calculated as

$$\frac{L}{\mathbf{v}_{\text{drift}}} = \frac{4\pi\alpha\rho_i\rho_n L}{(\nabla\times\mathbf{B})\times\mathbf{B}} = (25 \text{ Myr}) \left(\frac{B}{3 \mu\text{G}}\right)^{-2} \left(\frac{n_n}{10^2 \text{ cm}^{-3}}\right)^2 \left(\frac{L}{1 \text{ pc}}\right)^2 \left(\frac{\chi}{10^{-6}}\right). \quad (1.15)$$

For a small ionization fraction χ , ion-neutral drift is the primary process driving the evolution of a core as it nears collapse. Typically, diffusion takes 10-20 times longer than free-fall collapse. Presumably, the core must wait over this period for the magnetic field to be damped and star formation to ensue. This may be one reason for the smaller than expected star formation rate.

1.3 Polarimetric Methods

Magnetic fields in star-forming regions are most widely studied using polarization imaging. In this way, the structure of the field can be determined, whether the region being probed is an entire molecular cloud, a small clump, a stellar disk or a galactic arm. All types of radiation contain perpendicular oscillating electric and magnetic fields, wherein the former determines the polarization state. In particular, astronomers are most interested in the intensity of radiation, defined as proportional to the square of the magnitude of the electric field.

A linearly polarized electromagnetic wave has an orientation that repeats every π radians (Heiles 2002). For any arbitrary position angle, χ , there are both horizontal and vertical contributions to the total polarization. These can be summarized in a column vector known as the *Jones vectors*. Consider an electric disturbance defined as

$$E_x = E_{x_0} e^{i(2\pi\nu t + \delta_x)} \quad (1.16)$$

$$E_y = E_{y0} e^{i(2\pi\nu t + \delta_y)} \quad (1.17)$$

where E_{x0} and E_{y0} are the magnitudes in the usual two-dimensional coordinate system (Clarke 2010), and δ_x and δ_y are the associated phase delays. In general, the Jones vector can be stated as

$$\mathbf{E} = \begin{bmatrix} E_x \\ E_y \end{bmatrix}. \quad (1.18)$$

After rotation of the coordinate axes by χ radians,

$$\mathbf{E} = |\mathbf{E}| \begin{bmatrix} \cos \chi \\ \sin \chi \end{bmatrix} \quad (1.19)$$

and the radiation is linearly polarized. Furthermore, when the phase delays in Equations (1.16) and (1.17) are combined into a single phase lag ϕ ,

$$\mathbf{E} = \begin{bmatrix} E_{x0} e^{i2\pi\nu t} \\ E_{y0} e^{i2\pi\nu t} e^{i\phi} \end{bmatrix}. \quad (1.20)$$

Here, the essence is conveyed: that E_y trails E_x by a phase ϕ (Heiles 2002). Most generally, when ϕ does not equal zero or ninety degrees, \mathbf{E} is elliptically polarized. That is, the tip of the vector \mathbf{E} traces out an ellipse as it travels over time. In so doing, it can rotate either clockwise or counterclockwise as seen by the receiver, classifying the vector as left circularly polarized (LCP) and right circularly polarized (RCP) respectively, when there is no linear polarization component. That is, when $\phi = \pm 90^\circ$, we have the special case of circular polarization.

1.3.1 Stokes Parameters

Unlike the example presented thus far, naturally occurring radiation is composed of many vibrations, with an array of frequencies, orientations and phases. Such a wave cannot be defined by a solitary polarization as before, but rather each disturbance must be measured separately. Altogether, the same cumulative state of polarization may be achieved, but more than likely there is some degree of incoherence, or unpolarization. The Jones vectors cannot account for such a scenario (Heiles 2002). As a result, while there are three parameters used to identify the type of polarization, a fourth is sometimes necessary to constrain how much of the radiation is, in fact, polarized. As a set, these four variable are called the *Stokes parameters*.

1.3.1.1 Stokes I

By combining the two orthogonal polarizations in the vertical (Y) and horizontal (X) directions, we first obtain the Stokes I parameter, as introduced by George Stokes in 1852 (Stokes 1852)

$$I \propto E_X^2 + E_Y^2 = E_{0^\circ}^2 + E_{90^\circ}^2 \quad (1.21)$$

where each of the electric field components has been squared so as to yield the respective powers. Thus, Stokes I gives an indication of the total power in the radiation. This same definition holds for elliptical polarization, where

$$I \propto E_{\text{RCP}}^2 + E_{\text{LCP}}^2. \quad (1.22)$$

1.3.1.2 Stokes Q

The Stokes Q parameter differs mechanistically from Equation (1.21) in that the two orthogonal components are now differenced

$$Q \propto E_X^2 - E_Y^2 = E_{0^\circ}^2 - E_{90^\circ}^2 \quad (1.23)$$

Physically however, Equation (1.23) now represents the amount of polarization in either the vertical or the horizontal direction. For instance, if $E_Y^2 = 0$, then $Q = I$ and all polarization is in the horizontal direction. The reverse leads to $Q = -I$ and complete vertical polarization. However, to completely characterize the linear polarization state, one must also consider linear polarization of the field at an angle $\chi = 45^\circ$, in which case $Q = 0$.

1.3.1.3 Stokes U

To fully categorize the linear polarization, the Stokes U parameter is used:

$$U = E_{45^\circ} - E_{-45^\circ} \quad (1.24)$$

With both Q and U , the linear polarization is completely characterized.

1.3.1.4 Stokes V

In the same way that E_X and E_Y are orthogonal, so too are the two circular polarization states, named right- and left-handed, or RCP and LCP. By taking a difference one obtains Stokes V :

$$V = E_{\text{RCP}}^2 - E_{\text{LCP}}^2 \quad (1.25)$$

Unlike linear polarization, which required two Stokes parameters and four separate intensity measurements, Stokes V completely encapsulates, alone, any circular polarization state.

1.3.1.5 Normalized Stokes Parameters

The fractional amount of linear and circular polarization can be expressed as

$$p = \frac{(Q^2 + U^2)^{1/2}}{I_u + I_p} \quad (1.26)$$

and

$$v = \frac{V}{I_u + I_p} \quad (1.27)$$

respectively, where I_p and I_u are the polarized and unpolarized components of the total flux. In an analogous fashion, each of the Stokes parameters individually may be normalized, and it is this quantity that is almost exclusively measured in astronomical polarimetry. That is, $q = Q/I$, $u = U/I$ and $v = V/I$, where $I = I_u + I_p$. As a result, the level of polarization is given by

$$p = (q^2 + u^2)^{1/2}. \quad (1.28)$$

The position angle, χ , which specifies the orientation of linear polarization, is evaluated from (Hildebrand et al. 2000)

$$\theta = 0.5 \arctan(u/q). \quad (1.29)$$

Finally, using Equations (1.28) and (1.29), the following two relationships are often quite useful

$$Q = pI \cos(2\theta) \quad (1.30)$$

$$U = pI \sin(2\theta). \quad (1.31)$$

1.3.2 Dust Polarization

Interstellar dust grains are prevalent in star-forming clouds, emitting thermal radiation that must be accounted for in any infrared/submillimeter survey. In some cases, the thermal radiation itself can be polarized as high as $\sim 10\%$, while in others the dust serves to polarize light from background stars. Aligned silicate grains will absorb most preferentially at $\sim 10 \mu\text{m}$, where there is a polarization peak (Aitken et al. 1986), but transmitted polarized light is detected from 5-25 μm . Grains that are radiatively heated will emit at longer infrared wavelengths normally between 60 and 600 μm . Both scenarios provide a means for mapping the orientation of the plane of the sky component of the magnetic field.

Dust grains in the presence of a magnetic field will align themselves with their spin axis parallel to the direction of the field. The surrounding gas or radiation torque (see below) will impart kinetic energy to the grain, causing it to rapidly rotate. Eventually, damping processes (Purcell 1979) will align the spin axis along the axis with the greatest rotational inertia: the short axis (Hildebrand 1988). When intervening starlight is absorbed by the particles the observed radiation will give a measure both of the optical depth, and, if combined with other data, the strength of the field (see §1.3.5). Once aligned, the plane in which most of the absorption of the electric field vector takes place, the long axis, will be perpendicular to the field. As a result, light passing through will be polarized in a direction parallel to the field lines. Once this practice is applied to dense clouds with infrared background or embedded sources, scattering off the grains, out of the line-of-sight, becomes problematic.

Similarly, the polarization of emission from magnetically aligned grains is dependent on the direction of alignment, as caused by the field (Hildebrand 1988). This time, the strongest emitted component of the electric field vector \mathbf{E} is along the long axis of the grain, resulting in a polarization direction perpendicular to the field.

Therefore, for regions where polarization from selective absorption and grain emission are both measured, the two planes of polarization should be approximately orthogonal.

Both means of polarization require a certain amount of alignment of the individual dust grains in a common direction. The initial quandary however, is how such an aligning mechanism can act given the frequency of collisions between gas molecules and dust grains, especially in a dense cloud. Although there are some competing theories, including those that do not, in fact, require a magnetic field, the following will elaborate on the magnetic processes most widely accepted.

The most obvious way to align any spinning body is directly, as analogous to a compass needle (Spitzer & Tukey 1951). This requires an exorbitantly large torque however, in order to quench the precession about the field lines. Such a torque must be of a magnitude near the kinetic energy of rotation ($\sim kT$) and therefore Spitzer and Tukey (1951) had to assume a meager temperature of the gas of 10^0 K (Davis Jr. & Greenstein 1951). In regions of higher temperature, such as HII regions or diffuse emission nebulae, clearly this will not do. Instead, one of two things must occur: either the angular velocity must be damped in between collisions, or a series of small nonconservative torques must act to pivot the grain towards alignment. Davis Jr. and Greenstein (1951) defined a phenomenon known as *paramagnetic relaxation*, whereby any component of a grain's rotation perpendicular to the field is eliminated. Once the magnetic field \mathbf{B} has introduced a magnetization \mathbf{m} to the grain, the torque $\mathbf{m} \times \mathbf{B}$ will act to slowly remove these components and thus produce alignment. However, this process takes place at a much slower pace than would be needed to overcome the misaligning effects of collisions with gas molecules.

Purcell (1979) noted that interstellar grains undergo suprathreshold rotation, or routine additional torques that amplify the rotation rates, courtesy of three different phenomena. These include H_2 formation on the surface of grains, photoelectron

emission after absorption of a UV photon, and fluctuations in the so-called “accommodation coefficient” that determines how responsive the dust is to interaction with other gases. Purcell (1979) suggested that if the grain surface maintained consistency, then these torques might be long-lived enough to allow paramagnetic relaxation to bring them into alignment with the field.

The most recent and most promising theory for grain alignment is that by radiative torques (RATs), as first proposed by Dolginov and Mytrophanov (1976). The interaction of grains with the radiation field will cause superthermal rotation (Draine & Weingartner 1997) and ultimately alignment (Lazarian & Hoang 2007). The torques that are responsible are a result of differential scattering of right- and left-hand circular components by a grain with a net helicity (Andersson et al. 2011). Additionally, they are a function of the grain size, the density of the radiation field and its wavelength, and the degree of anisotropy. Radiation that is the same in all directions is not effective at aligning the grains in this manner. In fact, there is an additional efficiency factor in the torque expression that depends on the angle between the magnetic field and the anisotropy direction, Ψ . Attempts have been made to probe this behaviour for dust grains with stellar radiation dominated by only one source. By observing the polarization in the dust cloud relative to different background stars, one can get a handle on how the alignment efficiency varies with Ψ . The radiative alignment mechanism, unlike some of the prevailing theories, solves the issue of a grain never achieving sufficient angular momentum, and therefore making paramagnetic relaxation unfeasible.

1.3.3 Zeeman Effect

While the idea of magnetic fields threading molecular clouds is theoretically sound, their presence is much harder to deduce observationally. Troland and Heiles (1982) were the first to employ the Zeeman splitting of molecular lines toward this end.

The hydroxyl radical, OH, while convenient as a tracer of gas in molecular clouds, is more frequently used as a probe of this effect. Rampant in the radio bands of large telescopes at 1665 and 1667 MHz, OH is nevertheless very weak in emission relative to the absorption features created by strong continuum backgrounds. This adversely affects the sensitivity that can be attained in these types of observations. Nevertheless, OH is especially suitable for probing dark, dense clouds, where deducing magnetic field strengths is most difficult (Crutcher et al. 1993).

A molecule subjected to a magnetic field \mathbf{B} will see its energy modified by an amount

$$\Delta E_{mag} = -\boldsymbol{\mu} \cdot \mathbf{B} \quad (1.32)$$

where μ is the molecule's magnetic moment in a given quantum state. When the field is introduced, there is a change in energy ΔE_{mag} from the unperturbed, $\mathbf{B} = 0$ case. The OH molecule has an unpaired electron with both an orbital angular momentum \mathbf{L} and a spin angular momentum, \mathbf{S} . The electron is attracted towards the internuclear axis, creating a torque that causes \mathbf{L} to precess around the nuclear bond between the two atoms. Another torque is exerted on the spin angular momentum by a magnetic field set up by the movement of the remaining electrons and the two nuclei. The end result is that both \mathbf{L} and \mathbf{S} are rapidly precessing around the axis defined by the O-H bond. Together with the angular momentum of the axis itself \mathbf{O} , as each of the two nuclei rotate, the total orbital and electron spin angular momentum is given by $\mathbf{J} = \mathbf{L} + \mathbf{S} + \mathbf{O}$ (Stahler & Palla 2004). Finally, the H nucleus makes a small spin angular momentum contribution, \mathbf{I} , that is the final term in the total angular momentum $\mathbf{F} = \mathbf{J} + \mathbf{I}$. The energy ΔE_{mag} , is proportional to \mathbf{F} through its associated quantum number M_F . The complete expression is

$$\Delta E_{mag} = -g\mu_B M_F B \quad (1.33)$$

where g is known as the *Landé g -factor*, a dimensionless quantity. In this analysis, g , a function of every quantum number but M_F , is set to unity. Recalling that energy is related to frequency through Planck's constant, the frequency splitting becomes

$$\Delta\nu_{mag} = \left(\frac{b}{2}\right) B \quad (1.34)$$

where b wraps all our constants together, and the factor $1/2$ is included so as to centre the splitting with respect to the unperturbed line. The Zeeman splittings for the 1665 and 1667 MHz lines have the values 3.27 and 1.96 Hz μG^{-1} , respectively.

Quantum selection rules for electric dipolar transitions limit ΔM_F to 0 and ± 1 only, meaning lines are observed at ν_0 , $\nu_0 + \Delta\nu_{mag}$ and $\nu_0 - \Delta\nu_{mag}$ exclusively. These are known as the π -, σ_L - and σ_R - transitions, so called because of their polarization states, which are crucially dependent on the angle of observation relative to the direction of the magnetic field (Stahler & Palla 2004). When the two are perpendicular, all three lines appear, with the $\Delta M_F = 0$, π line twice the amplitude of the symmetric σ lines. From this vantage point, each of the lines are linearly polarized; the π line oscillating in a direction parallel to the field, and the two shifted lines perpendicular to the field. Conversely, for an observer aligned parallel to the magnetic field, only two lines are visible: the σ_R line, which appears to be rotating counter-clockwise to the observer, and the σ_L line, which rotates in an opposite, clockwise sense. By our accepted definitions, these lines are thus right- and left-circularly polarized, respectively.

Even the intensity of the lines depends strongly on the angle θ between the line of sight and the direction of \mathbf{B} . Table 1.1 lists the observed intensities of polarized OH radiation towards dark clouds for: $I(\nu - \nu_0)$ proportional to the intensity at

frequency ν , ν_z the Zeeman-induced frequency shift, and the intensities T_r , T_l , T_{\parallel} and T_{\perp} for detectors sensitive to right- and left-circularly polarized radiation and parallel and perpendicular to the magnetic field.

Table 1.1: Observed Zeeman Effect Line Intensities (Crutcher et al. 1993)

Polarized Intensities	Zeeman Components		
	$\nu_0 - \nu_z$	ν_0	$\nu_0 + \nu_z$
T_r	$T(\nu - \nu_0 + \nu_z)(1 - \cos \theta)^2$	$2T(\nu - \nu_0)(\sin \theta)^2$	$T(\nu - \nu_0 - \nu_z)(1 + \cos \theta)^2$
T_l	$T(\nu - \nu_0 + \nu_z)(1 + \cos \theta)^2$	$2T(\nu - \nu_0)(\sin \theta)^2$	$T(\nu - \nu_0 - \nu_z)(1 - \cos \theta)^2$
T_{\parallel}	$2T(\nu - \nu_0 + \nu_z)(\cos \theta)^2$	$4T(\nu - \nu_0)(\sin \theta)^2$	$2T(\nu - \nu_0 - \nu_z)(\cos \theta)^2$
T_{\perp}	$2T(\nu - \nu_0 + \nu_z)$	0	$2T(\nu - \nu_0 - \nu_z)$

Calculation of the above intensities is made easier if the line width $\Delta\nu \ll \nu_z$, such that each of the lines can be separately identified. If each of T_{\parallel} and T_{\perp} can be measured, then the direction of \mathbf{B} can be ascertained. Furthermore, the Stokes parameters also provide vital information about the field and can be calculated from the intensities in Table 1.1. In so doing, one finds that

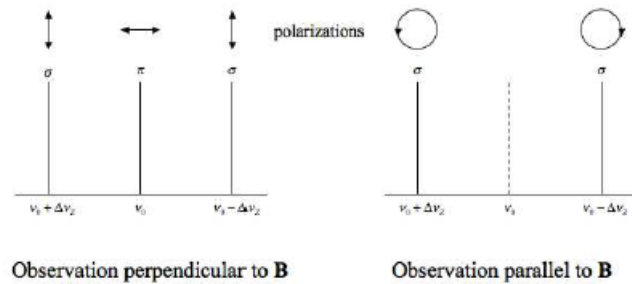


Fig. 1.1.— A schematic of the polarization states for a Zeeman split molecule.

$$\begin{aligned}
I &= T_r + T_l \\
&= 2T(\nu - \nu_0 + \nu_z)(1 + \cos^2 \theta) + 4T(\nu - \nu_0) \sin^2 \theta \\
&\quad + 2T(\nu - \nu_0 - \nu_z)(1 + \cos^2 \theta)
\end{aligned} \tag{1.35}$$

$$\begin{aligned}
V &= T_r - T_l \\
&= [4T(\nu - \nu_0 + \nu_z) - 4T(\nu - \nu_0 - \nu_z)] \cos \theta \\
&= \left(\frac{dI}{d\nu} \right) \nu_z \cos \theta
\end{aligned} \tag{1.36}$$

$$\begin{aligned}
Q &= (T_{\parallel} \cos \phi + T_{\perp} \sin \phi) - (T_{\parallel} \sin \phi + T_{\perp} \cos \phi) \\
&= 2[-T(\nu - \nu_0 + \nu_z) + 2T(\nu - \nu_0)] (\cos \phi - \sin \phi) \\
&= -\frac{1}{4} \left(\frac{d^2 I}{d\nu^2} \right) (\cos \phi - \sin \phi) (\nu_z \sin \theta)^2
\end{aligned} \tag{1.37}$$

$$\begin{aligned}
U &= [T_{\parallel} \cos(45^\circ - \phi) + T_{\perp} \sin(45^\circ - \phi)] \\
&\quad - [T_{\parallel} \sin(45^\circ - \phi) + T_{\perp} \cos(45^\circ - \phi)] \\
&= 2[-T(\nu - \nu_0 + \nu_z) + 2T(\nu - \nu_0) - T(\nu - \nu_0 - \nu_z)] \sqrt{2} \sin \phi \\
&= -\frac{1}{4} \left(\frac{d^2 I}{d\nu^2} \right) (\sqrt{2} \sin \phi) (\nu_z \sin \theta)^2
\end{aligned} \tag{1.38}$$

where ϕ is the position angle of \mathbf{B} in the plane of the sky. The derivatives in each of Equations (1.36), (1.37) and (1.38) are only applicable however when $\nu_z \ll \Delta\nu$ as is the case for all non-maser lines in molecular clouds. Theoretically, it is possible to determine $|\mathbf{B}| \sin \theta$, the component of the magnetic field perpendicular to the line-of-sight, from Equations (1.37) and (1.38). However, both depend on the second

derivative of the intensity and are thus quite small and difficult to measure. Therefore, only Stokes V and I are measured observationally.

As must be true, Equation (1.36) has no prevailing dependence on the unshifted frequency ν_0 . The right- and left-circularly polarized intensities are measured from the standpoint of an observer parallel to the magnetic field, where the π line does not emit. Detecting Stokes V leads to a measure of the magnetic field component parallel to the line-of-sight, $|\mathbf{B}| \cos \theta$, equivalent to the spectrum that would be obtained for a field of strength $|\mathbf{B}|$ at an angle θ to the line-of-sight. Once Crutcher et al. (1983) measured the Stokes V -spectrum, they then fit the derivative of the Stokes I spectrum in order to find B_{\parallel} .

Instrumental polarization can also arise when attempting to probe the magnetic field strength. An important phenomenon which must be considered is that of “beam squint”, a misalignment of the two telescope beams susceptible to right- and left-circularly polarized radiation. If not pointed in the same direction, distortions in the Stokes V -spectrum can emulate that predicted from the Zeeman effect, making it difficult to separate the two. This is because the presence of a velocity gradient in OH absorption in front of a continuum source between where the two beams are pointed will lead to a V -spectrum that will replicate the Zeeman effect. Specifically, beam squint effects will be introduced if the axis of the photon-collecting feed horn is not parallel to that of the reflecting surface (Troland & Heiles 1982). In turn, there may be unique differences in the beam displacements upon changes in right ascension (RA) and declination (DEC) that must be accounted for. Beam squint effects are especially troublesome given the small field strengths being probed. In order to alleviate this concern, multiple lines are observed with different Zeeman splitting factors. The beam squint will remain the same across the lines, providing an accessible way to disentangle the effects. Another, more crude option involves constantly polarization and position switching so as to produce the desired alignment between the right- and

left-handedly polarized beams (Crutcher et al. 1999; Falgarone et al. 2008; Hezareh & Houde 2010). This, however, requires very precise control of the tracking of the instrument in order to compensate for relatively small positional errors.

1.3.4 Goldreich-Kylafis Effect

The Zeeman splitting technique is the only direct way of measuring magnetic field strengths, and even still, can only probe the line-of-sight (los) component, due to the relative weakness of the Stokes Q and U spectra (see §1.3.3). Most of the time, the field strengths within molecular clouds are not sufficient to split the molecular line, and instead only broaden it. Following the discussion of §1.3.3, all three ΔM_F transitions will then fall at the same position, $\sim \nu_0$. The techniques of Goldreich and Kylafis (1981) however, can still resolve the direction of polarization of the line emission as either parallel or perpendicular to the magnetic field in the plane of the sky. Originally, the authors predicted spectral lines of around 10% linear polarization, for clouds of low, anisotropic optical depths. They began with a molecule with two rotational states and angular momenta, which was later extended by Deguchi and Watson (1984) to multiple rotation states and radiative transitions (Cortes et al. 2005). By including these additional terms, the polarization levels were reduced by a factor of 2. Cortes (2005) further extended the calculations to include an external source term representing dust emission. Ultimately, the authors wished to determine a fractional linear polarization

$$P = \frac{I_{\perp} - I_{\parallel}}{I_{\perp} + I_{\parallel}} \quad (1.39)$$

for the intensities I_{\perp} and I_{\parallel} perpendicular and parallel to the magnetic field in the plane of the sky. These intensities are found in the equations of radiative transfer, which are valid only under a very key assumption. Namely, there must be a large

velocity gradient (LVG), the so-called Sobolev approximation, where the line width $\Delta\nu$, Zeeman splitting $g\mu_0 B$ and natural line width γ obey the relation $\Delta\nu \gg g\mu_0 B \gg \gamma$.

For velocity gradients that are smaller in directions parallel to the magnetic field, there will be larger optical depths than perpendicular to the field, where the gradient is larger. As a result, radiation will be preferentially absorbed along the field lines, resulting in larger populations of the magnetic substates leading to $\Delta M_F = \pm 1$ (or σ) transitions, which peaks in a direction parallel to the field. Meanwhile, the $\Delta M_F = 0$ (the π transition) radiation peaks in directions perpendicular to the field lines, and thus will have smaller populations (Cortes et al. 2005). In an isotropic environment, the populations of all the substates are identical, and there is no net polarization in any observable direction. That is, the π - and σ - lines will combine to give zero polarization. Conversely, if one of the π - or σ - lines begets a larger population, then there will be a net polarization in the corresponding direction. For instance, if the $\Delta M_F = \pm 1$ substates have a larger population, then the σ -radiation will be stronger, and the radiation will be linearly polarized in the direction of polarization of the σ -radiation. Since there is more absorption occurring parallel to the field, the radiation will be polarized perpendicular to the magnetic field. In general, for a magnetic field in the plane of the sky, the default polarization directions are as in Figure 1.1, where the π -lines are polarized parallel to the field lines, and the σ -lines are polarized perpendicular to the field.

Cortes (2005) also considered the inclusion of an external source of radiation. If, for example, it were directed perpendicular to the field lines, then the magnetic substates leading to the $\Delta M_F = 0$ (π line) transition would be more rapidly excited than those leading to $\Delta M_F = \pm 1$ (σ) transitions. Excitation of the intervening molecules would lead to a greater velocity gradient, and, as before, a larger population. The π radiation will be stronger and will therefore determine the net polarization

direction, parallel to the magnetic field. Typically, this external source of radiation is in the form of dust in the cloud. In cases where both velocity gradients and dust are present, the polarization direction is dependent on the relative effectiveness of the two causes of anisotropy (Cortes et al. 2005).

1.3.5 Chandrasekhar-Fermi (CF) Method

Chandrasekhar and Fermi (1953) determined the strength of the magnetic field in the spiral arms of our Galaxy through the magnetic orientation of interstellar dust grains. As was stated earlier, light passing through magnetically aligned grains will experience different amounts of absorption parallel and perpendicular to the direction of alignment (see §1.3.2). Hiltner (1951; 1949) measured the amount of extinction of background starlight towards a large sample of stars, establishing that it is polarized independent of wavelength. Additionally, radiation that was unreddened, appearing the same as it might when originally emitted, exhibited no polarization. This confirmed that absorption by interstellar dust grains was responsible for the measured polarization. According to the analysis of §1.3.2, this type of polarization should be parallel to the direction of the magnetic field lines. However, pre-existing polarization maps (Hiltner 1951) showing that the magnetic field is parallel to the arm in which we are positioned are only partly validated by observations. Indeed, there are many irregularly distributed deviances in the direction of polarization. On average, there is a small angular offset from the axis along which the spiral arm is aligned, α . Chandrasekhar and Fermi sought to establish a relationship between this angular offset and the magnitude of the magnetic field. The analysis that follows derives from attempts to reconcile the aforementioned discrepancy.

Another possible interpretation of the incomplete alignment of the polarization with the magnetic field lines may be that the lines of force fluctuate along their length. In this case, any particular line will have transverse oscillations, y , given by

$$y = a \cos k(x - Vt) \quad (1.40)$$

as it is laterally displaced in the x direction. The lateral propagation of the magnetic lines of force, traveling at the Alfvén speed V , must be equal to the corresponding velocities of the turbulent gas in the spiral arm because of flux freezing. The turbulent motions of the gas will move at a speed of $\frac{1}{3}v^2$, where v is the root mean square velocity of the gas ensemble. Then,

$$\overline{\dot{y}^2} = \frac{1}{3}v^2, \quad (1.41)$$

where \dot{y} is the time derivative of Equation (1.40). Furthermore, if y' is the derivative with respect to x and represents the fluctuations in the magnetic force lines from a straight line in the plane of the sky, then

$$\overline{y'^2} = \alpha^2. \quad (1.42)$$

With Equations (1.40), (1.41) and (1.42), Chandrasekhar and Fermi derived an expression for the magnetic field strength in the plane of the sky as a function of the dispersion, α :

$$B_{pos} = \sqrt{\frac{4}{3}\pi\rho}\frac{v}{\alpha}, \quad (1.43)$$

where ρ is the density of diffuse matter affected by the magnetic force lines and v is the dispersion in velocity of the matter tied to the magnetic field. Here, as already stated, α must be deduced from polarization vectors mapping the region of interest, such as in Figure 1.2 (Vaillancourt et al. 2008), while the velocity of the gas can be inferred from spectral line profiles of well-known molecular species.

The methods of Chandrasekhar and Fermi (1953), while commonly accepted today

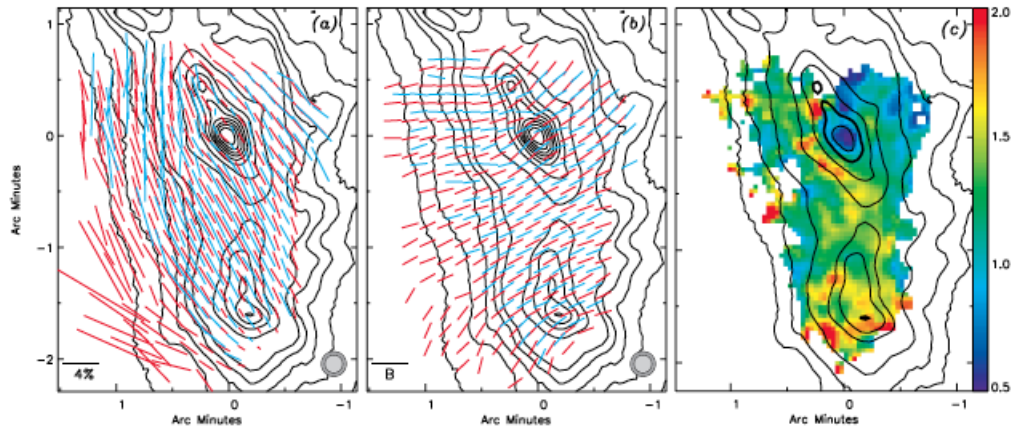


Fig. 1.2.— Polarimetric map of OMC-1. (a) 350 μm flux contours with superposed 350 (red) and 450 (blue) μm polarization vectors. (b) Inferred B -field orientation (plane of the sky). (c) Scale gives the polarization ratio between the two wavelengths shown in (a). *Figure courtesy of Vaillancourt et al. 2008*

as the best way to determine the plane of sky component of the magnetic field, still have their shortcomings. For one, Equation (1.43) is only valid for small angular deviations α . Also, the magnetic field must be close enough to the plane of the sky - that is, the inclination with respect to the line-of-sight is not a variable that can be considered (Houde et al. 2004). Houde (2004) has devised an extension to the CF method that furthers its domain of applicability to any given orientation of the B field. However, this introduces a new series of complications related to now having to measure the angle of inclination between the field and the line of sight; measurements that are not always possible. If this can be achieved, then one will be able to solve for not just the plane-of-sky component of the magnetic field, but the magnitude of the full three-dimensional vector representation. The intervening analysis, along with MHD simulations and numerical tests (Kudoh & Basu 2003; Ostriker et al. 2001), originally determined the necessity of a correction factor to Equation (1.43), presuming the field strength is not too low. The primary reason for this was that finite resolution observations smooth the measure of angular dispersion (Ostriker et al. 2001), decreasing α and therefore overestimating B . However, Houde et al. (2009)

showed that this correction factor is linked to the effects of signal integration through the cloud (i.e. the number of turbulent cells probed by the telescope beam).

Another factor that must be considered when applying the CF method is the turbulence of the molecular cloud; if especially massive and turbulent, the ions and neutrals will tend to decouple, leading to an error in the value of the mass density ρ . In this case, one cannot simply adopt the number for the (larger) neutral species, but must reduce this quantity upon utilization of the correction factor. The same applies to the velocity v : it is also slowed by the decoupling process.

When determining the magnetic field strength, there are some key considerations that make the application of the CF technique in molecular clouds much different than when measuring background starlight, as Chandrasekhar and Fermi did. In addition to the enhanced turbulence within a cloud, there may also be differential rotation, sites of gravitational collapse, or expanding HII regions, each of which will serve to increase the dispersion of the field. Hildebrand et al. (2009) refined the analysis of polarization maps so as to determine the plane-of-the-sky turbulent dispersion in molecular clouds, while avoiding any of these non-turbulent effects. They were able to calculate a ratio of the turbulent to large-scale magnetic field strengths using dust polarization measurements, where the total field was defined as $\mathbf{B}(\mathbf{x}) = \mathbf{B}_0(\mathbf{x}) + \mathbf{B}_t(\mathbf{x})$ for a structured, deterministic field \mathbf{B}_0 and a random, turbulent component \mathbf{B}_t . Not only is this important for determining the amount of turbulent energy contained in the magnetic field, but also to be able to employ the CF method (Hildebrand et al. 2009; Houde et al. 2009). In this way, the resulting B -field strength was determined in the Orion Molecular Cloud (OMC-1) to be $760 \mu\text{G}$ (Houde et al. 2009) once the effects of signal integration are properly accounted for (see Figure 2 in Houde et al. (2009)).

1.4 Conclusion

The process of star formation occurs in cold, dense, molecular complexes that are often buried within larger, more massive parent clouds. The physics governing how the clouds will collapse upon themselves at the rate at which they do cannot be understood without a detailed knowledge of the strength and morphology of the magnetic fields that thread them. Unfortunately, direct observational evidence of magnetic fields is lacking, and limited to only a few precise methods. All of these involve the use of polarimetry, which can be used to probe the direction, and occasionally the strength of the field. Such measurements can also lead to a physical understanding of the properties of dust grains, and, on larger scales, the role of magnetic fields over the spatial extent of entire galaxies. Each of these techniques continue to be enhanced and employed across a range of regions as astronomers continue to attempt to solve the star formation enigma.

- Aitken, D. K., Roche, P. F., Bailey, J. A., et al. 1986, MNRAS, 218, 363
- Andersson, B.-G., Pintado, O., Potter, S., Straizys, V., & Charcos-Llorens, M. 2011, A&A, 534, 19
- Carr, J. S. 1987, ApJ, 323, 170
- Chandrasekhar, S., & Fermi, E. 1953, ApJ, 118, 113
- Clarke, D. 2010, Stellar Polarimetry (Wiley-VCH)
- Cortes, P., Crutcher, R., & Watson, W. 2005, ApJ, 628, 780
- Crutcher, R., Troland, T., Goodman, A., et al. 1993, ApJ, 407, 10
- Crutcher, R. M., & Kazès, I. 1983, A&A, 125, L23
- Crutcher, R. M., Troland, T. H., Lazareff, B., Paubert, G., & Kazès, I. 1999, ApJ, 514, L121
- Davis Jr., L., & Greenstein, J. L. 1951, ApJ, 114, 206
- Deguchi, S., & Watson, W. D. 1984, ApJ, 285, 126
- Dolginov, A., & Mytrophanov, I. 1976, ApJ SS, 43, 291
- Draine, B., & Weingartner, J. C. 1997, ApJ, 480, 633
- Falgarone, E., Troland, T., Crutcher, R., & Paubert, G. 2008, A&A, 487, 247
- Goldreich, P., & Kylafis, N. D. 1981, ApJ, 243, L75
- Harwit, M., Houde, M., Sonnentrucker, P., et al. 2010, A&A, 521, L51
- Heiles, C. 2002, in ASP Conference Series, ed. P. G. S. Stanimirovic, D.R. Altschuler & C. Salter, Vol. 278

- Hezareh, T., Houde, M., McCoey, C., & Li, H.-B. 2010, *ApJ*, 720, 603
- Hildebrand, R. H. 1988, *Q. Jl. R. astr. Soc.*, 29, 327
- Hildebrand, R. H., Davidson, J., Dotson, J. L., et al. 2000, *PASP*, 112, 1215
- Hildebrand, R. H., Kirby, L., Dotson, J. L., Houde, M., & Vaillancourt, J. E. 2009, *ApJ*, 696, 567
- Hiltner, W. 1949, *ApJ*, 109, 471
- . 1951, *ApJ*, 114, 241
- Houde, M. 2004, *ApJ*, 616, L111
- Houde, M., Rao, R., Vaillancourt, J. E., & Hildebrand, R. H. 2011, *ApJ*, 733, 109
- Houde, M., Vaillancourt, J. E., Hildebrand, R. H., Chitsazzadeh, S., & Kirby, L. 2009, *ApJ*, 706, 1504
- Kolmogorov, A. 1941, *Akademiia Nauk SSSR Doklady*, 30, 301
- Kudoh, T., & Basu, S. 2003, *ApJ*, 595, 842
- Larson, R. B. 1981, *MNRAS*, 194, 809
- Lazarian, A., & Hoang, T. 2007, *MNRAS*, 378, 910
- Levy, E. 1993, *Protostars and Planets III*, ed. E. Levy & J. Lunine (The University of Arizona Press)
- Li, H.-B., & Houde, M. 2008, *ApJ*, 677, 1151
- MacLow, M.-M., & Klessen, R. S. 2004, *Reviews of Modern Physics*, 76, 125
- McKee, C. F., & Ostriker, E. C. 2007, *Ann. Rev. A&A*, 45, 565

- Mouschovias, T. C., & Spitzer, L. 1976, ApJ, 210, 326
- Ostriker, E. C., Stone, J. M., & Gammie, C. F. 2001, ApJ, 546, 980
- Purcell, E. M. 1979, ApJ, 231, 404
- Shu, F. H., Adams, F. C., & Lizano, S. 1987, Ann. Rev. A&A, 25, 23
- Spitzer, L., & Tukey, J. W. 1951, ApJ, 114, 187
- Stahler, S., & Palla, F. 2004, The Formation of Stars (Wiley-VCH)
- Stokes, G. 1852, Trans. Cambridge Philos. Soc., IX, 399
- Tan, J., Kong, S., Butler, M., Caselli, P., & Fontani, F. 2013, ApJ, 779, 96
- Tielens, A. 2005, The Physics and Chemistry of the Interstellar Medium (Cambridge University Press)
- Troland, T., Crutcher, R., Goodman, A., et al. 1996, ApJ, 471, 302
- Troland, T. H., & Heiles, C. 1982, ApJ, 252, 179
- Vaillancourt, J. E., Darren Dowell, C., Hildebrand, Roger, H., Kirby, L., & Krejny, M. M. 2008, ApJ, 679, L25

Chapter 2

Polarisation Observations of H₂O

$$J_{K_{-1}K_1} = 5_{32} - 4_{41} \text{ 620.701 GHz}$$

Maser Emission with

HERSCHEL/HIFI in Orion KL¹

2.1 Introduction

The Kleinmann-Low nebula in the Orion Molecular Cloud 1 (OMC-1) is a high-mass star-forming region, the nearest such region in our Galaxy at 418 ± 6 pc (Kim et al. 2008). Its line-of-sight velocity relative to the local standard of rest (LSR) is about 8 km s^{-1} (Garay et al. 1989). Since the discovery of the 22.235 GHz water maser transition in the Orion Molecular Cloud (Cheung et al. 1969), the region has frequently been studied also at higher frequency maser transitions. Recently, Neufeld et al. (2013) mapped the theoretically predicted $J_{K_{-1}K_1} = 5_{32} - 4_{41}$ 620.701 GHz transition in the Kleinmann-Low Nebula (Orion KL) with *Herschel*/HIFI. Combining

¹Jones, S. C., Houde, M., Harwit, M. et al. 2014, A&A, 567, A31

their observations with collocated 22.235 GHz Effelsberg data, they were able to verify a maser pumping model arising from collisional excitation and spontaneous radiative decay (Neufeld & Melnick 1991). Hereafter, we will mostly refer to these frequencies as 22 GHz and 621 GHz.

The first astronomical detection of the 621 GHz maser transition of ortho water vapor (Neufeld & Melnick 1991) was made by Harwit et al. (2010). It appeared to exhibit a polarisation of approximately 2% toward the oxygen-rich supergiant star VY Canis Majoris, and was a few times less luminous than the star's ortho-H₂O 22 GHz maser. The aforementioned study of Neufeld et al. (2013) presented the first detection of this transition in an interstellar region (i.e., Orion KL). Their maps of this region revealed a spatially localized source emitting a strong, spectrally narrow emission feature at 621 GHz. Their discovery of this feature gave rise to the present attempt to determine whether the 621 GHz feature might be linearly polarised. In a later search through the *Herschel* archives Neufeld et al. (2013) also found similarly narrow 621 GHz emission features emanating from the Orion South condensation and the W49N region of high-mass star formation. By then, however, the *Herschel* mission was ending and a search for signs of polarisation in these features were no longer possible. To date, the Heterodyne Instrument for the Far Infrared (HIFI) (de Graauw et al. 2010) onboard the *Herschel* Space Observatory (Pilbratt et al. 2010) has been the sole facility capable of linear polarisation studies of spectral lines at this frequency. Complementary circular polarisation studies, however, have remained beyond reach.

Between March 2011 and April 2012, we obtained six sets of observations of the 621 GHz line along a sight line toward Orion KL with the *Herschel*/HIFI instrument. We complemented these with observations of the 22 GHz line taken contemporaneously with the Max-Planck-Institut für Radioastronomie (MPIfR) 100-m telescope in Effelsberg, Germany. In Section 2.2 we report the results of these observations. We next present our polarisation results in Section 2.3, along with a depiction of the

temporal behaviour of the maser line over this year-long period. Finally, Section 4.6 presents our conclusions, while the tabular summaries of our observations, our maps of the 621 GHz water maser, and a further discussion on pointing errors can be found in Appendices A, B, and C.

2.2 Observations

2.2.1 HIFI Observations

HIFI enables observations in fourteen frequency bands. We observed the 621 GHz transition in HIFI Band 1B, which covers the range from 562.6 to 628.4 GHz. Like all of the other HIFI bands, Band 1B houses two channels sensitive to linearly polarised radiation, respectively, in the horizontal (H) and vertical (V) directions. The two channels exhibit peak sensitivities along directions at angles of 82.5° (H) and -7.5° (V), relative to the *Herschel* spacecraft’s y-axis, kept close to perpendicular to the ecliptic plane at all times. On the sky, the H- and V-beams are offset from each other by $6''.6$, a non-negligible fraction of the $34''.4$ full-width-half-magnitude (FWHM) beam at 620.701 GHz. Due to potential beam pointing errors, small offsets in the H- and V-beam from their intended positions may be expected, leading to uncertainty in the mean beam pointing direction. At the time of writing this was constrained to between $0''.8 - 0''.9$ (1σ).

Observations were conducted beginning on 14 March 2011 when a small map was acquired using the HIFI “on-the-fly mapping” (OTF) mode, as part of the HEXOS Guaranteed Time Key Program (PI: E. Bergin). A total of fifteen Nyquist-sampled pointings were implemented in a rectangular, 5 by 3 configuration. Spectral data were obtained with the digital autocorrelation high-resolution spectrometer (HRS) and the wide-band spectrometer (WBS). The map was centered at (R.A.[J2000]=

$05^{\text{h}}35^{\text{m}}13^{\text{s}}.16$, decl.[J2000]= $-05^{\circ}22'00''.5$), and spanned $\simeq 21''.3$ in Right Ascension and $\simeq 53''$ in Declination. Individual pointings were separated by $\simeq 10''.5$ in R.A. and $\simeq 13''$ in Declination. The spectral resolution in the HRS mode was 0.125 MHz, or, equivalently, a line-of-sight velocity resolution of 0.06 km s^{-1} . The WBS resolution was $\approx 1 \text{ MHz}$ or $\approx 0.5 \text{ km s}^{-1}$. All observations used an OFF-source reference position located $14'$ from the maser location.

Following the mapping of 14 March 2011, two pointed observations were obtained that year, respectively, on 26 March and 8 April. Over this period the source rotated by $\approx 14^{\circ}$ about the spacecraft line-of-sight. Observations obtained at different times were necessary since a minimum of two sets of measurements at separate source rotation angles are required for polarisation analyses (Harwit et al. 2010). For pointed observations the central point on the line separating the H- and V-beam centers was directed at two successive positions on the sky, in position switching mode, in order to place the center of the H polarisation beam for a given integration to coincide with the center of the V polarisation beam for the subsequent integration – thus compensating for the misalignment between the beams.

After a preliminary analysis, follow-up observations were executed on 25 February and 14 April 2012. The first of these, performed in position switching mode, were centered at the same position cited above. Thereafter, on 14 April, the last of the pointed measurements was obtained, followed on the same day by a small map of the same dimensions as that of 14 March 2011. While the 2011 observations lasted 888 s, integrations in 2012 were extended to 1683 s in order to reduce the overall noise. The entirety of the investigation is summarised in Table A.1.

2.2.2 Effelsberg Observations

Ground-based observations were undertaken with the 100-m Effelsberg radio telescope in tandem with the HIFI observations of 2011 and 2012. Centered at 22 GHz, the $J_{K_{-1}K_1} = 6_{16} - 5_{23}$ transition of ortho water vapour, our observations consisted of linear polarisation signals obtained from two orthogonal channels of the K -band (1.3 cm) receiver located at the primary focus of the telescope. The Effelsberg beam profile can be approximated as a Gaussian with a FWHM of $41''0$. The frequency resolution of each dataset was 6.104 kHz, corresponding to a velocity resolution of 0.082 km s^{-1} , and the spectra were calibrated using corrections for gain-elevation and atmospheric attenuation.

Our measurements were composed of pairs of scans obtained at different source parallactic angles in each of the years 2011 and 2012. In 2011, the first scan at 17:45 UT on 21 March, lasting one hour, was followed by a second scan recorded at 20:09 UT the same day, the source having rotated by approximately 23° by then. In 2012, pairs of observations were taken on 21 March and 18 April with corresponding source parallactic angle rotations of $\approx 67^\circ$ and $\approx 16^\circ$, respectively. All of these pointed observations were collocated with the HIFI center position. At the same epochs, maps were also produced that were useful in more accurately describing the maser environment. A complete summary of the Effelsberg data is provided in Table A.2.

2.3 Methods/Results

2.3.1 Polarisation Analysis

As explained in Harwit et al. (2010), HIFI does not provide regular 45° spacings with which the computation of the Stokes Q and U parameters is simplest. Instead, we must rely on the position angles (PA) listed in Table A.1 for the vertical polarisation

direction, with the horizontal axis at $PA + 90^\circ$. The Stokes Q and U can then be calculated using the analysis detailed in Harwit et al. (2010), from which the polarisation fraction and angle are evaluated with

$$p = \sqrt{Q^2 + U^2}/I \quad (2.1)$$

$$\theta = 0.5 \arctan(U/Q), \quad (2.2)$$

respectively, with I the total intensity. As explained below, this analysis has been applied to our entire set of HIFI 621 GHz data, with the 2011 and 2012 data sets combined to yield a single polarisation result of sufficient precision. The Effelsberg 22 GHz measurements were not affected by the same constraints and were considered separately for the respective 2011 and 2012 data sets.

2.3.2 HIFI data

The entire suite of observations listed in Table A.1 was considered, although only the center position of each of the maps (ObsIDs 1342215920-1 and 1342244411-2), where the maser intensity was strongest, was selected for analysis. All data were processed with version 8 of the *Herschel* Interactive Processing Environment (HIPE). Following an improvement in the absolute pointing error (APE) of the *Herschel* pointing products effective 19 Feb 2012 (Observation Day 1011) the reported center of the beam is accurate to within $0''.8 - 0''.9$ (1σ) for both position switching and OTF observations. Throughout our observations we found all pointings to lie within $\simeq 0''.4$ in Right Ascension and $\simeq 2''.4$ in Declination.

As shown in Table A.1, the position angles of the telescope ranged more widely across the observing epochs in 2012 than in 2011. When combined with the 2011 data the three additional datasets of 2012 reduced the noise in polarisation intensity

(pI) from $\simeq 85$ mK to $\simeq 17$ mK. Both the Stokes U and Q noise intensities dropped appreciably as well, to $\simeq 32$ and $\simeq 14$ mK, respectively.

Prior to deriving any polarisation measures, however, a marked change in the broad spectral component surrounding the narrow maser feature had to be taken into account. Although each dataset exhibits the broad component, its strength was clearly higher in the 2012 data, by almost as much as 50%. As explained in Appendix C, we believe that this change in the continuum level resulted from small pointing errors and the proximity of the powerfully emitting Orion “hot core”. Such differences, if resulting from pointing errors on an extended source, can render polarisation studies unreliable. Any claim about the polarisation of the maser line, therefore, required that it be separated from the underlying broad feature. To this end, two Gaussians were simultaneously fitted to the broad component and removed, to feature the maser line. From epoch to epoch there remained a substantial variability in the strength of the maser, at levels similar to those seen in the broad component itself. Nevertheless, we undertook a polarisation analysis on the assumption that the maser signals emanate from a single spatially unresolved (i.e., point-like) source in the region. As is discussed in Section 2.3.2.1, this assumption is consistent with the fact that we found no polarisation signatures above three standard deviations in the line, at a level of approximately 2%. Figure 2.1 shows the result of the analysis after removal of the broad component; the lack of polarisation in the maser emission is apparent from the absence of a corresponding signature in polarised flux (pI) in the bottom panel. The aforementioned change in maser intensity was accompanied by a shift in the line center velocity of $\simeq 0.2$ km s $^{-1}$ across both the horizontal and vertical polarisations from observing epoch 2 to 3, a significant fraction of the width of the line ($\simeq 0.9$ km s $^{-1}$).

These temporal changes in intensity and velocity are not surprising since, owing to their location in star forming regions, and in particular at the forefront of stellar

shocks, masers generally have an intensity that varies strongly on relatively short time scales: it is thought that such turbulent environs, with their large velocity gradients, can induce more frequent fluctuations in intensity with changes in the velocity of the emission line (Stahler & Palla 2004).

2.3.2.1 Pointing Effects on Maser Polarisation Measurements

We performed the same polarisation analysis discussed in Section 2.3.1 on a simulated spectrum to quantify the effect of our pointing uncertainties on measured maser polarisation signals. To do so the beam profile was approximated by a Gaussian function matching the FWHM of the HIFI beam at 620.701 GHz ($34''.4$), while the source was considered unpolarised and of no spatial extent (simulating a maser point source). Each simulated measurement was associated with one of our HIFI observations (see Table A.1), including random pointing errors of about $3''$, such as might reasonably be expected for HIFI. The peak intensity of a given measured spectrum would thus decrease as the pointing position drifted away from the source's location. This analysis revealed weak polarisation levels averaging $\sim 0.7\%$, consistent with the aforementioned upper limit resulting from our HIFI observations.

Although we cannot rule out the possibility that the totality of the 621 GHz maser flux we measure originates from the contributions of several spatially unresolved sources, our simple simulation seems to imply a lack of spatial extent for the overall maser emission, as compared to the HIFI beam. This feature allows for precise polarisation measurements when the pointing errors are sufficiently small. However, the same is not true for the broad component of the 621 GHz water line in view of potential source variations with pointing positions, as discussed in Appendix C.

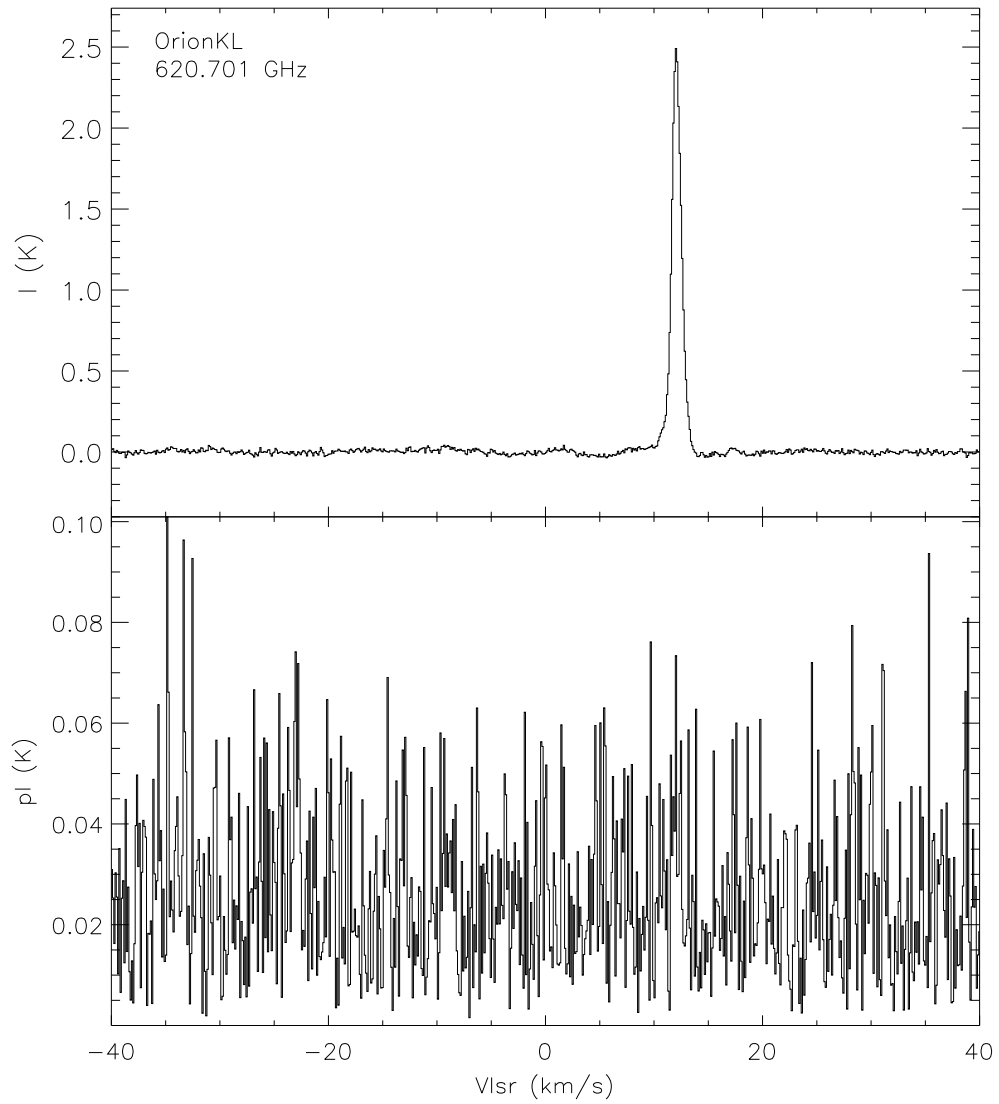


Fig. 2.1.— Stokes I (top) and the polarised flux pI (bottom) for the 621 GHz water maser line based on an analysis of all six epochs combined.

2.3.3 22 GHz (Effelsberg) Data

The 22 GHz Effelsberg data, obtained during the same periods (although not precisely coeval), do not appear to be affected by the same source of emission responsible for the broad component in the 621 GHz transition. However, we also observed significant change in intensity on timescales of one to several months (i.e., between respectively 21 March 2012 and 18 April 2012, and 21 March 2011 and 18 April 2012), which imply some intrinsic source evolution with time. We find that the strongest component at 7.2 km s^{-1} varies from $\simeq 1.2 \times 10^4 \text{ K}$ to $\simeq 2.1 \times 10^4 \text{ K}$ (or from 14 kJy to 26 kJy). These variations are in line with other observations performed at the position of peak intensity of the 22 GHz maser (located some $\simeq 15''$ east and $\simeq 36''$ south from our pointed observations) during approximately the same time period. More precisely, interferometric observations of Matveyenko et al. (2012) revealed significant outburst activity between July 2011 to May 2012 while tracking the evolution of velocity components at 7.0 km s^{-1} and 7.6 km s^{-1} . Previously, in February 2011, Hirota et al. (2011) recorded a flare reaching an intensity of 44 kJy using the VLBI Exploration of Radio Astrometry interferometer. While, unlike our study, these observations were conducted at very high spatial resolutions ($\sim 1 \text{ mas}$), single-dish observations of Otto & Gaylard (2012) at approximately $120''$ resolution also detected strong flares reaching as high as 80 kJy during an eight-month period spanning from March to November 2011.

We performed a polarization analysis on each of our Effelsberg data sets and found that the polarization levels did not appreciably change over the different epochs. Figure 2.2 shows the results of the analysis for the 21 March 2011 data. The top panel displays the Stokes I spectra, along with several linear polarisation measures, while the bottom panel shows the polarisation flux and angles. Most noticeable are the high polarisation levels, of order 75% at the center of the 7.2 km s^{-1} feature. Elsewhere, the polarisation level is rather constant in the 3 – 5% range, except for the second

strongest feature at $\sim 11.7 \text{ km s}^{-1}$, where levels exceed 10%. While there have been previous detections of polarisation of comparable levels (Horiuchi & Kameya 2000; Garay et al. 1989), the aforementioned contemporaneous interferometric observations of Matveyenko et al. (2012) revealed lower polarization levels of about 55% at 7.65 km s^{-1} .

2.4 Conclusion

We have reported the astronomical detection of the 621 GHz $J_{K_{-1}K_1} = 5_{32} - 4_{41}$ transition of the ortho H₂O maser in the star-forming region Orion KL, which was also recently discussed by Neufeld et al. (2013). In observations with the *Herschel*/HIFI instrument the maser was found not to be linearly polarised to a 3σ upper limit of $\sim 2\%$. Low polarisation levels for water masers are not inconsistent with expectations from the mechanism of Goldreich, Keeley and Kwan (Goldreich et al. 1973), at least in the absence of radiative saturation (Watson 2009). These results are also approximately in line with the low polarisations of a few percent found by Harwit et al. (2010).

Polarisation measurements of the HIFI data were complicated by the strengthening of a broad pedestal component in data from 2011 to 2012. We concluded that this feature is likely to be the result of pointing artifacts. Attempts were also made to settle the change in maser line strengths between the two observing epochs but the question remains to be resolved.

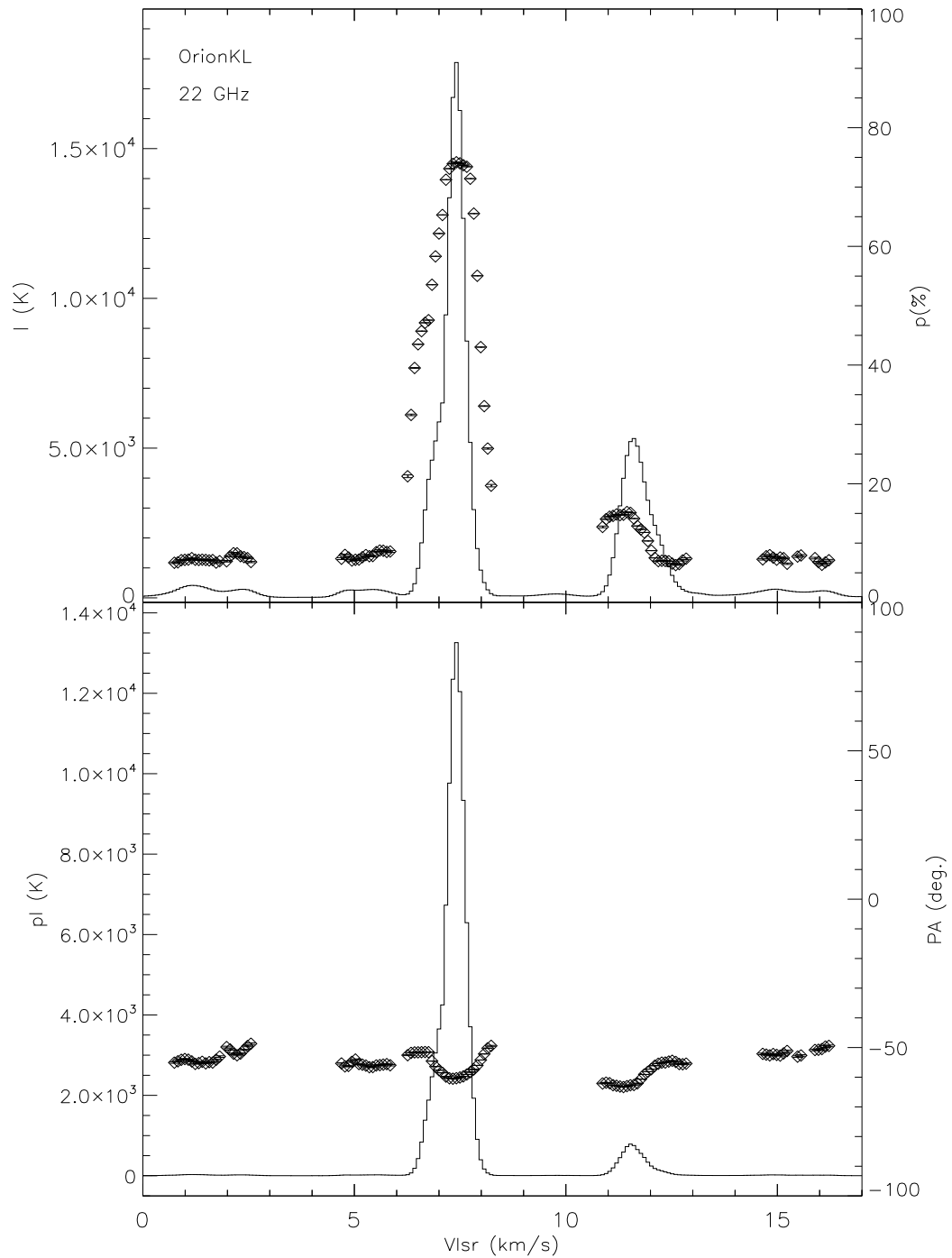


Fig. 2.2.— Polarisation properties of the 22 GHz water maser transition as measured at Effelsberg on 21 March 2011. (*Top*) Overlay of the percent polarisation (symbols, using the scale on the right) relative to the total intensity at a velocity resolution of 0.08 km s^{-1} . (*Bottom*) Polarisation flux and angles (symbols, using the scale on the right).

- Beuther, H., Zhang, Q., Greenhill, L., et al. 2005, *ApJ.*, 632, 355
- Chandrasekhar, S., & Fermi, E. 1953, *ApJ.*, 118, 113
- Cheung, A., Rank, D., Townes, C., Thornton, D., & Welch, W. 1969, *Nature*, 221, 626
- de Graauw, T., Helmich, F., Phillips, T., et al. 2010, *A&A*, 518, L6
- Garay, G., Moran, J., & Haschick, A. 1989, *ApJ*, 338, 244
- Goldreich, P., Keeley, D., & Kwan, J. 1973, *ApJ.*, 179, 111
- Goldreich, P., & Kylafis, N. 1981, *ApJ*, 243, L75
- Harwit, M., Houde, M., Sonnentrucker, P., et al. 2010, *A&A*, 521, L51
- Hildebrand, R. H., Kirby, L., Dotson, J. L., Houde, M., & Vaillancourt, J. E. 2009, *ApJ.*, 696, 567
- Hirota, T., Tsuboi, M., Fujisawa, K., et al. 2011, *ApJ.*, 739, L59
- Horiuchi, S., & Kameya, O. 2000, *Publ. Astron. Soc. Japan*, 52, 545
- Houde, M., Vaillancourt, J. E., Hildebrand, R. H., Chitsazzadeh, S., & Kirby, L. 2009, *ApJ.*, 706, 1504
- Kim, M. K., Hirota, T., & Honma, M. 2008, *PASJ*, 60, 991
- Matveyenko, L., Demichev, V., Ipatov, A., Melnikov, A., & Surkis, I. 2012, *Astronomy Letters*, 38, 764
- McKee, C., & Ostriker, E. 2007, *ARA&A*, 45, 565
- Neufeld, D., & Melnick, G. 1991, *ApJ.*, 368, 215
- Neufeld, D. A., Menten, K. M., Kraus, A., et al. 2013, *ApJ.*, 769, 48

Otto, S., & Gaylard, M. 2012, in Proceedings IAU Symposium No. 287

Pilbratt, G., Riedinger, J., Passvogel, T., et al. 2010, A&A, 518, L1

Stahler, S. W., & Palla, F. 2004, The Formation of Stars (Wiley-VCH)

Watson, W. 2009, in RevMexAA, Serie de Conferencias, 113

Chapter 3

Methods Toward Recovering a Polarization Signal from the Four-Stokes-Parameters Spectral-Line Polarimeter

3.1 Introduction

With the advent of new instrumentation, submillimetre/millimetre (SMM) astronomy has flourished as an essential tool in our study of the interstellar medium (ISM) and its evolution. This advancement has been buoyed by, most notably, the recent construction of the Atacama Large Millimetre Array (ALMA) in the deserts of northern Chile. ALMA is a multi-national interferometric project representing the best opportunity yet to probe the deepest recesses of our Galactic environment. In the coming years, ALMA will hopefully be joined by the Cerro Chajnantor Atacama Telescope (CCAT) and the continued use of the Submillimetre Common-User Bolometer Array (SCUBA-2) at the James Clerk Maxwell Telescope (JCMT) at the forefront of obser-

vational astronomy at these wavelengths. Of especial relevance to SMM astronomy is the study of star formation and evolution, and the cycle of interstellar material, including dust grains and molecules. While optically shielded by dust particles, these stellar nurseries become much more transparent when viewed at SMM wavelengths. In particular, stellar light absorbed by surrounding dust grains is reemitted at longer wavelengths. In many cases, this radiation is linearly polarized, as the anisotropic dust grains are aligned by the local magnetic field. Therefore, the sub-field of SMM polarimetry provides our greatest tool to probe an assortment of magnetically regulated astrophysical effects. For example, magnetic fields have been found to play a role in circumstellar disks and jets (Davis et al. 2000), the formation of non-self-gravitating filaments (Hennebelle 2013), and field structure on a galactic scale (Greaves et al. 2002). They have also been proposed to regulate the star formation process (Mouschovias 2001), especially in the low-mass regime. This point however, remains contentious, as alternative models have been put forth recognizing turbulent flows as the primary driver in cloud and core formation (MacLow & Klessen 2004; Padoan & Nordlund 1999). More recently, work has evolved to incorporate both scenarios in comprehensive theories and simulations (Nakamura & Li 2005; Kudoh & Basu 2008).

In order to fully characterize the magnetic field in a particular region of the ISM, one must be able to ascribe both an orientation and a strength. As was mentioned in Chapter 1 of this thesis, at present there is but one way to directly quantify the field's strength: with Zeeman line-broadening measurements. This technique will normally only provide information on the line-of-sight component of the magnetic field. The so-called normal Zeeman effect yields three components: an unshifted, linearly polarized, π component, and two σ components split symmetrically from the main emission feature by an amount $\Delta\nu_Z = \pm Z|\mathbf{B}|$, where Z is the Zeeman coefficient specific to the spectral transition and $|\mathbf{B}|$ is the magnitude of the magnetic field. These two components are elliptically polarized in opposite directions. Altogether,

the magnitude of $\Delta\nu_Z$, plus the degree of polarization of the σ features and their amplitudes relative to the π component, allows a complete understanding of the magnetic field (Crutcher et al. 1999, 1993; Falgarone et al. 2008; Heiles 1997).

In practice, however, it is much more common that $\Delta\nu_Z \ll \delta\nu$, where $\delta\nu$ signifies the spectral line width. If this is the case, then only information about the line-of-sight component of the magnetic field can be gleaned, after fitting the first derivative of the Stokes I spectrum, $dI/d\nu$, to the measured Stokes V spectrum, due to the σ components. Additionally, many more than two circularly polarized components can be created as a result of magnetic hyperfine splitting. The OH 1665 MHz line for example, has three linearly polarized π lines, two right-circularly polarized σ lines, and two left-circularly polarized σ lines (Stahler & Palla 2004).

The orientation of the field in the plane-of-the-sky can be inferred from the direction of linear polarization as caused by the magnetically aligned dust grains (Hildebrand et al. 1999). Molecular lines can also be polarized as per the Goldreich-Kylafis effect (Goldreich & Kylafis 1981; Glenn et al. 1997), should there be an imbalance in the magnetic sub-level populations parallel and perpendicular to the field. The resulting field direction then depends on which of these two sub-level populations dominate. That is, there can be a 90° ambiguity in the orientation of the magnetic field (see Chapter 1).

3.2 The Four-Stokes-Parameter Spectral-Line Polarimeter (FSPPol)

The Four-Stokes-Parameter Spectral-Line Polarimeter (Hezareh & Houde 2010) was developed for and deployed at the Caltech Submillimeter Observatory (CSO) atop Mauna Kea, Hawaii. The instrument is mounted within the elevation tube, in the

path of the beam between the receiver and the tertiary mirror behind the telescope dish. FSPPol comprises two side-by-side wave plates, a half-wave plate (HWP) to measure linear polarization, and a quarter-wave plate (QWP) to measure circular polarization (see Figure 3.1) since the CSO receivers are linearly polarized. Each are 100 mm in diameter, while the entire instrument is positioned where the 230 GHz telescope beam waist is approximately collimated at 40 mm (see Figure 3.2). Both plates have their own anti-reflection coatings and are placed within concentric rings that permit an external user to be able to rotate either the HWP or QWP to the desired angle relative to the receiver.

Prior to observing, the wave plates must be aligned with the polarization axis of the receiver. To this end, a cold load is placed in front of FSPPol (Hezareh & Houde 2010) while each wave plate is rotated through a large range of angles. The incoming polarization state is fixed by a polarizing grid (Houde et al. 2001) located prior to the entire assembly, later removed for on-sky integrations. Adjustments in the vertical direction within the elevation tube were also made according to the signal received from a small circular cold load, which was manually positioned at different spots in the beam.

The CSO uses a superconducting-insulating-superconducting Nb-AlN-Nb receiver (Kooi et al. 2014). We use the recently commissioned 230/460 GHz heterodyne instrument, operational since May 2012. The polarization axis is oriented north-south in the frame of the sky, independent of the pointing direction of the telescope, which is on an alt-azimuth mount. This is because the receiver assembly is mounted in such a way that it rotates with the telescope in elevation. Therefore, only one polarization state can be measured at a time, meaning that multiple integrations must be performed in order to recover the Stokes parameters. When measuring linear polarization, the HWP can be rotated to each of four angles θ between the plate's slow axis and the polarization axis of the receiver. These are defined by $\theta = (\gamma + \theta' + 90^\circ)/2 = 0^\circ, 90^\circ, 45^\circ$

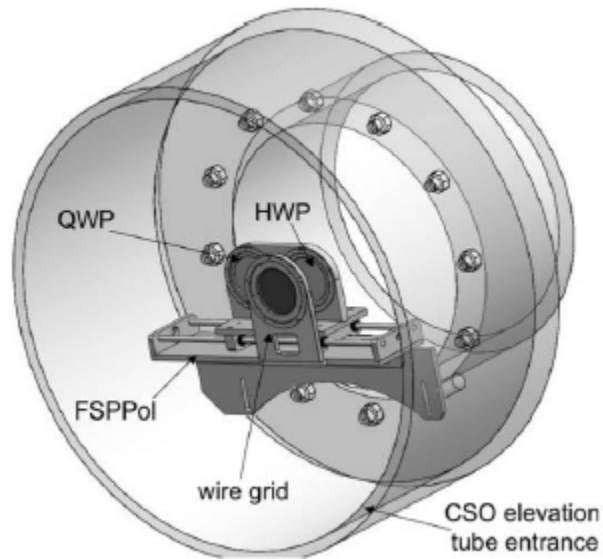


Fig. 3.1.— Schematic of FSPPol within the elevation tube of the CSO. An intervening wire grid is used to maintain a consistent polarization state during alignment but is not used during observations. *Figure taken from Hezareh et al. (2010).*

and 135° , where γ is the parallactic angle of the source on the sky and θ' the angle at which we are attempting a polarization measurement in the frame of the source; see Figure 3.3. By including γ we are able to account for any sky rotation in the source between measurements. Additionally, should γ vary by more than a preset threshold ($\approx 1^\circ$) the wave plate is able to compensate by rotating by the required amount. Once a cycle of four measurements are attained, the linear polarization parameters are given by $Q = I_{0^\circ} - I_{90^\circ}$ and $U = I_{135^\circ} - I_{45^\circ}$.

To obtain a circular polarization result, the QWP is positioned at an angle of $\pm 45^\circ$ relative to the polarization axis of the receiver, such that for $+45^\circ$ we are capturing the right-handed circular polarization (I_{RCP}) and for -45° the left-handed circular polarization (I_{LCP}). In turn, the fourth Stokes parameter, V , can be calculated as $V = I_{\text{RCP}} - I_{\text{LCP}}$, where LCP and RCP follow the conventions as set out in Chapter 1.

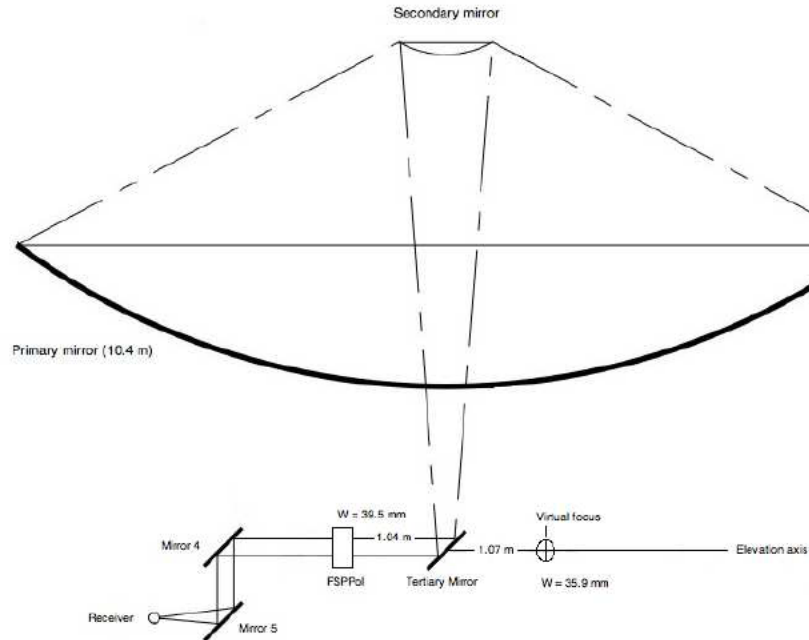


Fig. 3.2.— Schematic of the CSO telescope and the propagation of the beam through the associated optics. FSPPol is placed 1.04 m from the tertiary mirror in the direction of Mirror 4. The receiver is positioned at one of two Nasmyth foci, while a virtual focus of the tertiary mirror lies 1.07 m in the direction opposite to FSPPol. *Figure taken from Hezareh et al. (2010).*

Owing to the fact that we are not able to collect the two polarizations required to deduce the Stokes parameters at the same time, there is the potential for telescope pointing drifts between successive measurements. This presents both a challenge and an opportunity. For one, the existence of pointing errors between, for example, a right-circularly polarized and a left-circularly polarized signal is tremendously detrimental when attempting to make a circular polarization measurement. This is because the process of taking a difference between two signals centred at different positions will introduce an artificial polarization. Our advantage however, is that as we have separate datasets for I_{RCP} and I_{LCP} , we are able to align the two to our satisfaction.

The fact that individual polarization measurements are recorded at different times

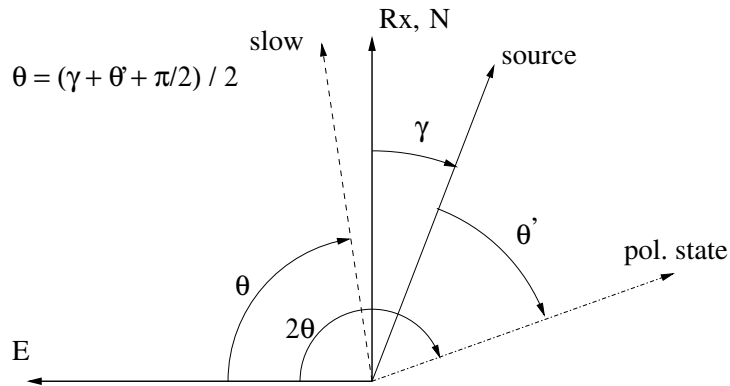


Fig. 3.3.— Illustration of the quantities relevant to determining the angle between the slow axis of the wave plate and the East-West axis on the sky, given by θ . The parallactic angle of the object is given by γ and θ' is the angle at which we wish to measure the polarization state of the source. *Figure adapted from Hezareh et al. (2010).*

is particular to our setup. Nowadays, many facilities are equipped with a digital correlator and dual-polarization receivers that allow simultaneous acquisition of all four Stokes parameters using auto- and cross-correlations. While these types of set-ups are not immune to sources of instrumental polarization (IP), the artificial polarization (AP) that accompanies pointing drifts, or beam squints, can only be diagnosed, and cannot be corrected for through the realignment of maps obtained at complementary polarization states. For example, Heiles (2001a) and Heiles et al. (2001a, 2001b), discuss and characterize the IP arising from three telescopes and their corresponding correlators: the NRAO 140 foot telescope, the Arecibo telescope, and the NRAO 12 m telescope. Each instrument uses autocorrelations to produce Stokes I and Q , while the real part of the cross-correlation gives Stokes U and the imaginary part Stokes V . The first correlation polarimeter put to use in the millimeter, XPOL (Thum et al. 2008), is installed at the IRAM 30-m telescope on Pico Veleta in Granada, Spain. For all of these instruments, the primary concerns are the appropriate gain calibration and spatial alignment between the two orthogonal polarization receivers.

Discrepancies in pointing between orthogonal polarizations as recovered from a

correlator can often be traced to a misalignment of the telescope feeds. While steps are taken so as to eliminate this possibility, ultimately only post-processing analysis of the data can alleviate the problem. This differs from our setup at the CSO, whereupon all observations can be aligned to a chosen standard. That being said, with both setups it is important to also take measurements of an unpolarized target and thereby suitably characterize the full structure of the beam. These methods, and their role in correcting for other sources of instrumental polarization, will be detailed further in Section 3.4.2.

3.2.1 Instrumental Polarization

We have chosen to produce small maps of both a simulated extended Gaussian source, which will be presented here, as well as a particular subregion of the Orion A molecular cloud, the data from which will be deferred to Chapter 4. In both scenarios, the maps are subject to many different forms of IP beyond pointing errors. Here, we are aided by our use of maps on two fronts. Most importantly, we are able to assess the full profile of the 32'' CSO beam as it relates to possible manifestations of IP. In producing a Stokes I map of an extent commensurate with the CSO beam size, we are able to quantify, and hopefully later remove, spurious polarization signals due to the so-called sidelobes of the telescope beam. To our knowledge this has never been attempted at the CSO.

The ideal beam should be describable by a width, Θ_0 , an ellipticity Θ_1 and its orientation ϕ_{beam} , and a coma with a strength α_{coma} and an orientation or position angle ϕ_{coma} (Rohlfs & Wilson 2000). For example, Heiles et al. (2001a) used the Arecibo telescope to make four pointed observations of the unpolarized source B1749+096 at 1175 MHz, about an assumed beam centre, so as to characterize the main beam and first sidelobe. The resulting image was Gaussian least-squares fit and six Fourier coefficients used to reconstruct the sidelobe; see Figure 3.4. The main-beam param-

eters are $(\Theta_0, \Theta_1) = (4'.00, 0'.36)$, in half-power beam-widths (HPBW), $\phi_{\text{beam}} = 91^\circ.1$, $\alpha_{\text{coma}} = 0.048$ and $\phi_{\text{coma}} = 41^\circ.4$, while the first sidelobe has a mean height of 0.029 relative to the intensity of the main-beam.

One of the most common explanations for the existence of sidelobes is blockage and scattering by feed support struts (Kildal et al. 1988; Ng et al. 2005). Computations done at the Dominion Radio Astrophysical Observatory Synthesis Telescope at 1420 MHz (Ng et al. 2005) found that the first sidelobe was highly polarized to levels of up to 50%. The authors here claimed the asymmetry of the antenna at large, off-axis angles was the contributing factor, an effect that is enhanced with the blockage of the feed support struts.

Advantageously, at the CSO, radiation proceeds directly from the primary through to the secondary and tertiary mirrors, before reaching one of two Nasmyth foci and the receiver. The secondary is supported by a quadrupod mount through the centre of the main reflector, ensuring a symmetrical design with no off-axis components. Thus, while an origin might not be able to be conclusively decided upon, the likely presence of sidelobes in the CSO beam cannot be ignored. Also, our method to account for IP, to be given in Section 3.4.2, does not rely on any ability to quantify an ellipticity, coma, or orientation. All this information is encoded in an image of an unpolarized target that will be used to remove IP from the data collected.

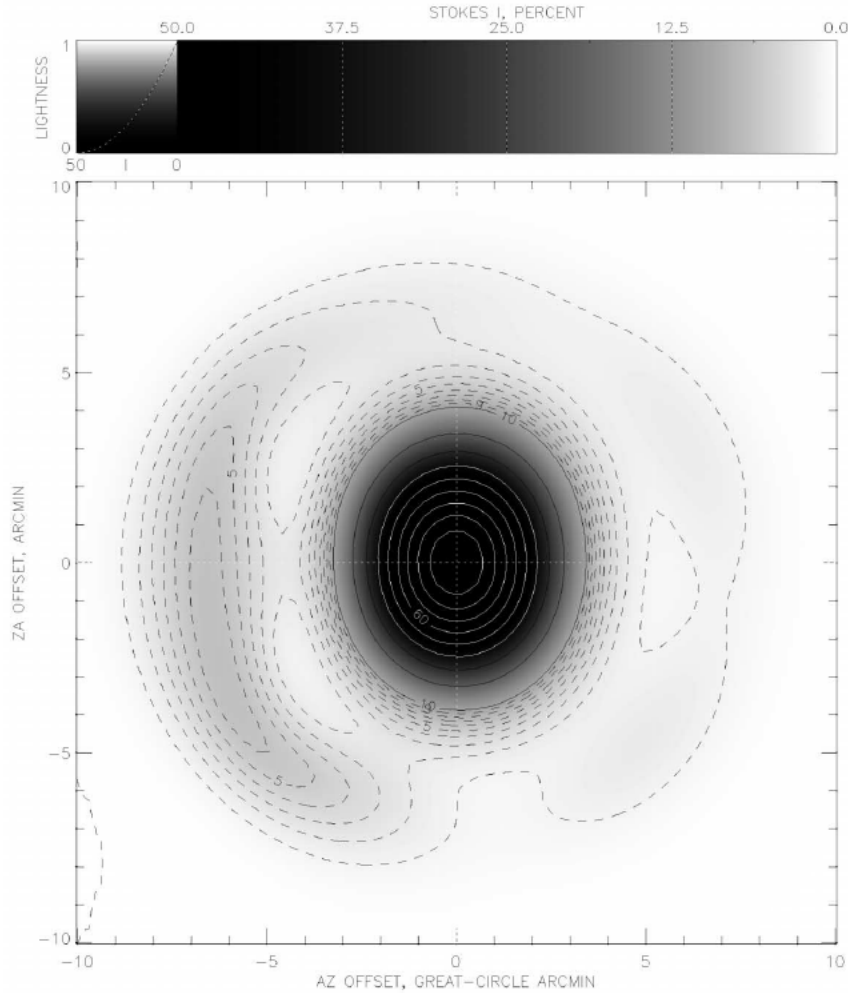


Fig. 3.4.— Contour of Stokes I of the Arecibo telescope reconstructed from parameters from a least-squares fit to the main beam and first sidelobe. Solid contours decrease in 10% increments of the peak, while dashed contours are given in 1% increments. The first sidelobe is polarized at approximately the 10% level. *Figure taken from Heiles et al. (2001a).*

Another possible source of IP is that of a calibration, or gain, error between the orthogonal polarization measurements. Typically, these are determined by observing an astronomical target of known flux. In our case, we rely on frequent temperature calibration scans taken at an off-source position. During this time two measurements

are made: one on the sky and another with a hot load in the beam between the receiver and the secondary mirror. It is these two recordings that allow a determination of T_A^* , the antenna temperature of a given source before any correction for telescope beam efficiency. In this way we can be sure that each polarization measurement is registered properly relative to all others, barring significant time between calibrations. Even still, it is reasonable to assume that any remaining calibration gains are random and thus will cancel out through a sufficiently large set of data.

In all likelihood this is not an exhaustive account of all sources of IP. Perhaps the most difficult situation to model is that of stray light from the optics preceding FSPPol and the detector. The most likely source are oblique reflections from the tertiary mirror. Furthermore, while the anti-reflection coating on the wave plates is effective at reducing standing waves along the beam path, there is no guarantee that they have been completely eliminated. We have also mounted FSPPol such that radiation hits the wave plates at an angle removed from normal by a few degrees (Hezareh & Houde 2010). Nevertheless, it seems prudent to continue to assume that standing waves exist and are contributing to the total IP. In our simulations, these two phenomena have been combined as a flat level of polarization across our maps.

The remaining discussion in this chapter will be focused on the simulation of each type of instrumental polarization, and the manner and effectiveness of the ways with which we can account for them.

3.3 Description of the Simulations

The simulations were designed to approximately mimic the data that will be presented in Chapter 4. Therefore, we will solely consider circular polarization, for which one RCP measurement and one LCP measurement comprise a single cycle. Gaussian spectra of FWHM 3.20 km s^{-1} have been created at all positions across the source,

but of an amplitude that diminishes as the beam moves off the map's centre. At each position the integrated intensity under the line was calculated, and a contour plot of the results produced. The map itself spans $70''$ in each of Right Ascension and Declination, with data points $10''$ apart along both axes. A number of cycles, $N = 6$ was chosen to be able to judge the efficacy of our IP corrections when the different errors introduced are random in nature, but much less than the 26 cycles of data to be presented in Chapter 4. The same setup was established for an unpolarized continuum point source to be used as a calibration standard for instrument polarization removal (see Section 3.4.2). These data covered a slightly larger area, $90'' \times 90''$ in R.A. and Decl., and were of a coarser spatial resolution of $15''$ along both axes to produce a closer representation of the corresponding Jupiter data presented in the next chapter. All of these parameters can be adjusted, and indeed may be as they are presented in the remainder of the chapter. Finally, each simulated map has been ascribed a parallactic angle concordant with the real data of Chapter 4, for purposes of realizing a realistic rotation of the source on the sky (see Section 3.4.2).

3.4 Correcting for Spurious Forms of Polarization

3.4.1 Reduction of Beam Squint through Map Alignment

As stated earlier, at the CSO, polarization states cannot be measured simultaneously, which can be problematic since Stokes parameters are generated from pairs of measurements. Procedurally there are a few ways to mitigate the time-dependent variations in pointing that are likely to arise. For example, circular polarization pairs are collected in alternating order, RLLRRL..., where R stands for I_{RCP} and L for I_{LCP} , as a way to avoid rotating the QWP after every integration. We also are careful to do frequent system temperature calibration scans in a best effort to minimize

any system gain variations between the right- and left-circularly polarized datasets. When doing on-the-fly mapping in the manner discussed in Section 3.3, for example, a temperature calibration is done after each row of spectral scans.

All polarization maps are aligned to the same reference image, the selection of which is mostly arbitrary, although an attempt is made to select a map that appears to visually have minimal pointing error. Unless there were drastic changes in observing conditions, the amount that each map needs to be shifted by should not vary significantly within an ensemble of maps. Afterwards, all polarization pairs can then be considered interchangeably and in any order.

It will now prove useful to define certain fundamental relations that will be necessary later in the image processing descriptions. For two spatial images g and h , their convolution, $g * h$, can be defined as

$$g(x, y) * h(x, y) \equiv \int_{-\infty}^{\infty} \int_{-\infty}^{\infty} g(\tau_1, \tau_2) h(x - \tau_1, y - \tau_2) d\tau_1 d\tau_2. \quad (3.1)$$

We can establish the Fourier transform of an image,

$$G(u, v) = \int_{-\infty}^{\infty} \int_{-\infty}^{\infty} g(x, y) \exp[-2\pi i(ux + vy)] dx dy, \quad (3.2)$$

where u and v are the spatial frequencies associated with the spatial variables x and y , respectively. The result $G(u, v)$, along with the original function $g(x, y)$, form what is known as a Fourier transform pair, denoted by \rightleftharpoons . From Equation (3.1), where $g(x, y) \rightleftharpoons G(u, v)$ and $h(x, y) \rightleftharpoons H(u, v)$, one can then quickly retrieve the convolution theorem

$$g(x, y) * h(x, y) \rightleftharpoons G(u, v)H(u, v), \quad (3.3)$$

meaning that the Fourier transform of a convolution is equivalent to the multiplication

of Fourier transforms.

Similarly, the correlation operation, \star , is expressed as

$$(g \star h)(\tau_1, \tau_2) \equiv \int_{-\infty}^{\infty} \int_{-\infty}^{\infty} g^*(x, y)h(x + \tau_1, y + \tau_2) dx dy, \quad (3.4)$$

where τ_1 and τ_2 are known as the spatial *lags* and $*$ is used to indicate the complex conjugate. In a similar fashion to Equation (3.3), one can derive what is known as the correlation theorem, defined thusly,

$$(g \star h)(\tau_1, \tau_2) \rightleftharpoons G(u, v)H^*(u, v). \quad (3.5)$$

By cross-correlating two maps, where one is the reference kernel and the other is to be aligned to it, we can assess the degree of similarity between them. The cross-correlation product is fit with a two-dimensional gaussian function such that the position of maximum intensity can be identified. The distance of this point from the true centre at $[0, 0]$ then represents the relative pointing misalignment. From here, a grid of bilinear interpolates is acquired at the new position, so long as there is enough surrounding data. Elsewise, a row and/or column at corresponding edges on the map are masked based upon the direction of the required shift. In this way, each map in succession is adjusted relative to the same kernel until all are centred at its position. Finally, we calculate Stokes V , and find an average of all cycles. This process is repeated for a calibration standard, for purposes of determining the amount of instrumental polarization (see Section 3.4.2).

Our simulations (see Section 3.3) will now be employed towards verifying that the methods outlined here can satisfactorily remove the effects of beam squint. An initially unpolarized source was subjected to random pointing errors of $3''$ standard deviation and the alignment method applied. The top panel of Figure 3.5 shows a Stokes V product for one cycle with relative pointing misalignments of $-4''31$ in Right

Ascension and $1''.72$ in Declination. The data span $90''$ in each direction, with each data point $15''$ from the next. Positive-valued contours are shown by the black solid lines, while negative-valued contours are marked by black dashed lines. The corresponding Stokes I map is also shown in red, for comparison. Immediately obvious is the bi-lobed structure about the $[0, 0]$ point, which is to be expected when subtracting two signals with offset intensity peaks. The bottom panel presents Stokes V for the same two maps, after they have been aligned. The cross-correlation was calculated by multiplying the fast Fourier transforms of the reference image and the image to be aligned (right-hand side of Equation (3.5)).

While the appearance of the Stokes V map in the bottom panel of Figure 3.5 enforces that we are able to align two maps with disparate pointings, we must simultaneously be able to realize an improvement in the amount of spurious instrumental polarization as caused by beam squint. Prior to alignment, the Stokes V map has a very high amount of variability relative to the Stokes I map, plotted in red in Figure 3.5. The peak position of each of the symmetric lobes has $\sim 13\%$ and $\sim -18\%$ polarization for the positive and negative lobes, respectively. Afterwards, these same positions decrease to $\sim 3.9\%$ and $\sim -5.4\%$ polarization. At the centre of the map, where much of the outlying flux is being redistributed, a reduction in polarization may not be apparent in a single cycle. However, as Figure 3.6 makes clear, as more cycles are included, we average down to the expected result. Indeed for the data presented in Figure 3.5, the same 3×3 mean about the centre yields $\sim 5.9\%$ polarization prior to correction and $\sim 4.0\%$ post-correction.

After map alignment the discrepancy in pointing from our example in Figure 3.5 has been dramatically reduced to but $-0''.17$ in R.A. and $0''.15$ in Decl. Given the size of our map and the size of the CSO beam of $\sim 32''$, to retain errors of these sizes seems more than acceptable.

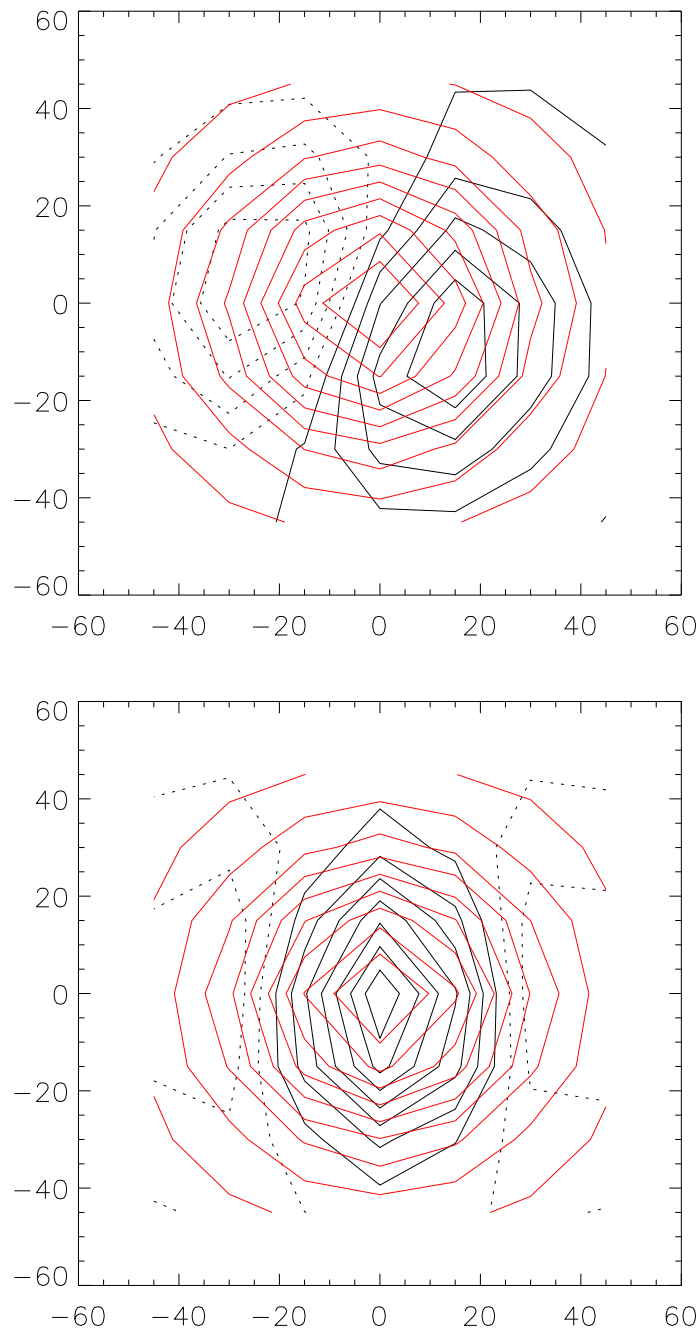


Fig. 3.5.— (*Top*) Stokes V for an unpolarized source subject to pointing errors of $\simeq 3''$. Both positive and negative contours are in roughly 20% increments; positive-valued regions are marked by black solid lines, negative-valued regions by black dashed lines. (*Bottom*) The same Stokes V map once aligned to the reference image. The corresponding Stokes I map is shown on each image in red. The strongest polarization signals were of about 18% before and 5.4% after alignment, respectively.

Significant reductions in polarization, while not always noticeable on a cycle-by-cycle basis, are realized upon averaging over multiple cycles. Eventually it should become apparent that by aligning the maps prior to calculating Stokes V , we are in fact realizing a more accurate polarization result. To test this, an unpolarized source (of dimensions $60'' \times 60''$ and step size $10''$) was used to synthesize twelve cycles of data, and the performance evaluated relative to the magnitude of polarization recovered. These results are shown in Figure 3.6 both prior to, and after correction for pointing errors of standard deviation $3''$. Each data point represents an average of the innermost 3×3 spatial locations in our Stokes V maps over a running average of the number of cycles included. Thus, in each case, whether before correction (asterisks) or after (triangles), these numbers should trend to the expected polarization - here, zero. Upon correcting for beam squint, this trend is established much more quickly, and offers a significant improvement on the pre-corrected values with every cycle.

The spectra in our simulations were imparted with Gaussian, white noise at all velocities, of an rms magnitude equivalent to that of our data to be analyzed. These uncertainties were then propagated through all stages of the analysis. First, for all points in the map, the rms was weighted over a number of channels equal to that contained in the velocity range over which the spectra were integrated to produce the contour maps. For each map, this result is then interpolated by the same amount derived from the alignment process. Thereafter each of the right-circularly polarized σ_{RCP} and left-circularly polarized σ_{LCP} uncertainty maps are averaged, where we are careful to only include those points that have not been masked during interpolation. To find the final Stokes V uncertainty map, σ_V , we are left to then combine σ_{RCP} and σ_{LCP} , and weight this result by the total number of cycles, N ,

$$\sigma_V = \frac{\sigma_{\text{tot}}}{\sqrt{N}} \quad (3.6)$$

where $\sigma_{\text{tot}} = \sqrt{\sigma_{\text{RCP}}^2 + \sigma_{\text{LCP}}^2}$.

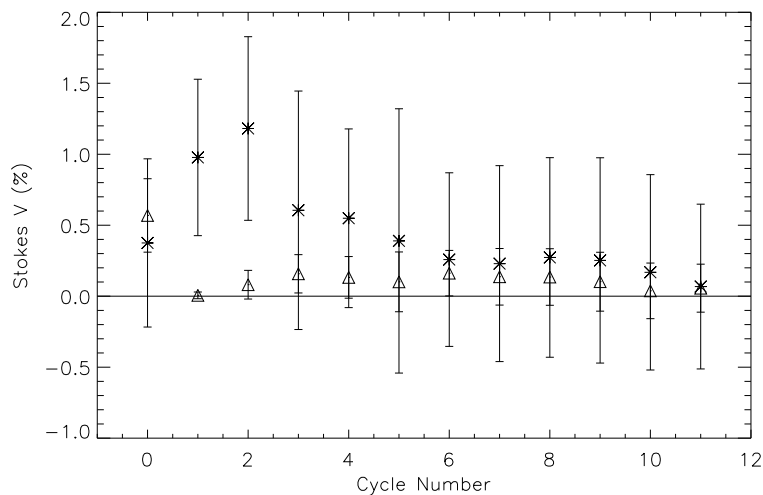


Fig. 3.6.— Average Stokes V polarization flux for the central 3×3 data points of the intensity map before (asterisks) and after (triangles) map alignment. The uncertainties on each point are dispersions about this mean.

3.4.2 Removing Other Forms of Instrumental Polarization

All remaining types of IP are dealt with in the same manner, to be discussed in this section. The first step is to collect an identical measurement on an unpolarized source, in as near to the conditions as were established for the data from the target of interest. From here the structure of the beam can be ascertained prior to its use in measuring polarization from a given source.

The primary benefit to be derived from observations on such an unpolarized source is the ability to identify sidelobes that may affect the uniformity of a true polarization signal. It is largely assumed that these offending features will be more important in the outer edges of the source's intensity pattern, where a possible polarization signal will be weakest and thus hardest to isolate. For example, an observation with the beam

centred on an edge of the source may have a sidelobe overlapping a region of stronger source intensity. This would produce a spurious signal that, in the end, could be interpreted as a polarization signature. It thus becomes imperative to properly map the beam sidelobes and remove their unwanted contribution in the data measurement.

Furthermore, in aligning the images, the data in the row and/or column on the outer edge in the direction where the map needs to be shifted cannot be trusted since an extrapolation would be required in these positions. We thus expect that our cumulative Stokes V maps will in general benefit from a lesser amount of data in the outer edges than elsewhere in the maps. Accordingly, this relative lack of data will result in higher uncertainties in these locations.

For all practical purposes, the CSO beam shape, and thus any persistent sidelobes, does not change across a set of observations since, as previously mentioned, the receiver used for our measurements is mounted in such a way that it rotates in elevation with the telescope. If the source is rotating and changing its parallactic angle, the same amount of rotation must be applied to the normalized beam map (i.e. our map of the unpolarized target) in order to retain the proper position of the beam sidelobes through a set of observations at different parallactic angles. This beam rotation is only needed to account for spurious sidelobe polarization signals, as other sources of IP are independent of the beam structure. For example, any random errors in gain calibration, oblique reflections off mirrors (the tertiary, for example), or polarization conversion errors due to imperfections in the HWP will mostly manifest themselves as constant levels of IP equally affecting all points on our Stokes V maps independent of the parallactic angle. This is because these sources of IP are a function of the total Stokes I intensity in a given measurement, and the fact that this intensity is very weakly dependent on the beam sidelobes.

In order to remove the instrumental polarization from the total polarization signal, it is first necessary mathematically to describe the signal that would be measured

without any spurious polarization. In the equations to follow, $S_{i,n}$ and $B_{i,n}$ designate, respectively, observed and true signals on the sky, $i = 0, 1, 2, 3$ stands for Stokes I , Q , U , or V , while $n = \text{“src”}$ or “P” depending on if we are dealing with signals from the source or the unpolarized target used to characterize the telescope beams. The normalized telescope beams are correspondingly represented with P_i . For example, the uncontaminated Stokes parameters I , Q , U and V , can be expressed as in Hezareh et al. (2013)

$$S_{i,\text{src}} = B_{i,\text{src}} * P_0. \quad (3.7)$$

Each are a function of the telescope normalized beam profile P_0 , as well as the sky brightness $B_{i,\text{src}}$ in each Stokes parameter.

Given the possibility of leakage from the Stokes I signal, Equation (3.7) should be amended to include parasitic IP signals from the telescope beams or reflections, etc., (Hezareh et al. 2013)

$$S_{i,\text{src}} = B_{i,\text{src}} * P_0 + B_{0,\text{src}} * P_i + R_i (B_{0,\text{src}} * P_0). \quad (3.8)$$

Here, $i = 1, 2, 3$ continues to refer to Stokes Q , U and V respectively, while the latter two terms on the right-hand side are, respectively, for the aforementioned IP signals from beam contamination (i.e. through Stokes I leakage) and reflections, etc., parameterized with R_i (assumed much smaller than unity). These two terms must somehow be removed from the measured $S_{i,\text{src}}$ in order to recover $B_{i,\text{src}} * P_0$. This can be accomplished as follows (here we closely follow and augment the analysis described in Hezareh et al. (2013)). We first seek to characterize the telescope beam by observing a known unpolarized standard source; for our purpose we choose an appropriate planet available at the time the observations were realized (the assumption of an unpolarized planet is common and precise enough for our analysis). In that case,

the normalized Stokes maps G_i can be expressed with

$$\begin{aligned} G_0 &= N_{0,P} * P_0 \\ G_i &= N_{0,P} * P_i + R_i * G_0, \quad i = 1, 2, 3, \end{aligned} \quad (3.9)$$

where $N_{0,P}$ is the normalized Stokes I profile of the planet. It should be noted that since the planet is assumed unpolarized, these maps, which are readily obtained from observations, are not only a representation of the IP due to the telescope beams but also contain the other forms of IP through the constant terms R_i . Although $N_{0,P}$ is unknown to us, the corresponding function G_0 is easily determined from the observed map (i.e. $S_{0,P}$) and is all we need for our analysis.

Performing a convolution of G_0 with Equation 3.8 yields

$$\begin{aligned} S_{i,\text{src}} * G_0 &= (B_{i,\text{src}} * P_0) * G_0 + (B_{0,\text{src}} * P_i) * (N_{0,P} * P_0) + R_i (B_{0,\text{src}} * P_0) * G_0 \\ &= (B_{i,\text{src}} * P_0) * G_0 + (B_{0,\text{src}} * P_0) * G_i, \end{aligned} \quad (3.10)$$

where we have interchanged the positions of P_0 and P_i in the second term on the right-hand side in going from the first to the second line. Alternatively,

$$\begin{aligned} (B_{i,\text{src}} * P_0) * G_0 &= S_{i,\text{src}} * G_0 - (B_{0,\text{src}} * P_0) * G_i \\ &\simeq S_{i,\text{src}} * G_0 - S_{0,\text{src}} * G_i, \end{aligned} \quad (3.11)$$

when keeping calculations to first order. Since all the quantities on the right-hand side are obtained through observations of the source and the planet, it follows that the

desired Stokes i ($i = 1, 2, 3$; i.e., $B_{i,\text{src}} * P_0$) signal can be recovered through a simple deconvolution with G_0 .

3.4.2.1 Simulating IP Removal

For the remainder of this chapter, we will be focused exclusively on simulated measurements of circular polarization, Stokes V . The nature of these simulations was detailed in Section 3.3. Their utility will be in quantifying the efficacy of the IP removal of our algorithm. Testing Equations (3.7)-(3.11), implies creating both a simulated source, of some uniform polarization, and an unpolarized calibration target. A simulated ^{12}CO ($J = 2 \rightarrow 1$) gaussian-profiled emission line of FWHM 5 km s^{-1} was integrated so as to produce a contoured source image. The spectrum at the centre was of an amplitude of 31.4 K , while to all spectra were added a noise level of 0.44 K rms . The SNR across the map ranges from ~ 2 near the edges to ~ 70 at the centre. All relevant sources of IP were incorporated, including beam squint (pointing errors), polarized sidelobes, and a spatially flat polarization meant to approximate all other unaccounted for sources of IP characterized by R_i in Equations (3.8), (3.9) and (3.10). The sidelobes were incorporated as concentric rings about the peak of radius $28''.3$ on the source data, with a size half that of the beam width, or $16''$. Their amplitudes varied sinusoidally up to 2% of the normalized beam's peak intensity. More precisely, to the right-circularly polarized data was added a ring oscillating as $\cos(2\Phi)$, with Φ the azimuthal angle mapping the beam map and the left-circularly polarized data $\sin(2\Phi)$. In each case the zero-angle position was oriented along an axis pointed radially outward from the map centre in the direction of increasing R.A.

In Figure 3.7 we outline the data analysis sequence for a set of twelve cycles of simulated data. At left are Stokes I (top) and V (bottom) for a continuum, unpolarized point source simulating a planet. Incorporated with this data are $3''$ random errors in pointing, a 2% spatially flat scaling, or gain difference between the

RCP and LCP images, and sidelobes as previously described. In convolving $S_{i,\text{src}}$ with the planetary data G_0 as in Equation (3.10), the convolution theorem assumes that each of the signal ($S_{i,\text{src}}$) and the response function (G_0) are periodic. In practice, this is not true, and upon convolution the response function will wrap around and spoil the edges of the convolved product. For this reason we are sure to first pad Stokes I and V of the source and unpolarized standard with zeros such that they have the same size. Figure 3.8 shows the spatial coverage of our planetary data, which spans $-45''$ to $45''$ in Right Ascension and Declination, and is extended by zeros in the hatched regions outside these bounds. The size of the CSO beam, marked by the circle, is also shown for reference, where, importantly, it is completely encapsulated by the simulated data itself.

In the middle column of Figure 3.7 are Stokes I (top) and V (bottom) for our hypothetical source of 2% polarization at all points of the map, with the same amounts and types of IP as for our planetary data, including a $3''$ pointing error. The convolution of Stokes V of the normalized unpolarized standard with Stokes I of our source yields the instrumental polarization measure (i.e. the last term on the right-hand side of Equation 3.11), given in the figure's bottom right. Above this is a similar convolution of the first two panels, the circular polarization of the source with Stokes I of the simulated normalized, unpolarized planetary target (left-hand side of Equation (3.10)). Therefore, the subtraction of the data in the bottom right panel from that in the top right will represent our attempt at removing the IP and establishing a possible circular polarization detection. We show the corresponding result in the left panel of Figure 3.9. The final step in the analysis requires a deconvolution of G_0 from the simulated data, in order to recover the original, $32''$ beam resolution. This was done using a Wiener filter and is shown in the right panel of Figure 3.9.

In this example, upon deconvolution a source polarization of $2.0 \pm 0.02\%$ was able to be recovered, averaged over the central three-by-three pixels. Prior to the IP

removal, there was a contaminated, total Stokes V of $3.6 \pm 0.02\%$. Uncertainties here were found in the same manner as alluded to in Equation 3.6, but weighted by the number of points going into the average, nine. Thus, while there has been a dramatic reduction in the amount of instrumental/artificial polarization, we have also not done so at the expense of the source polarization, recovering the input 2% within the 1σ uncertainty.

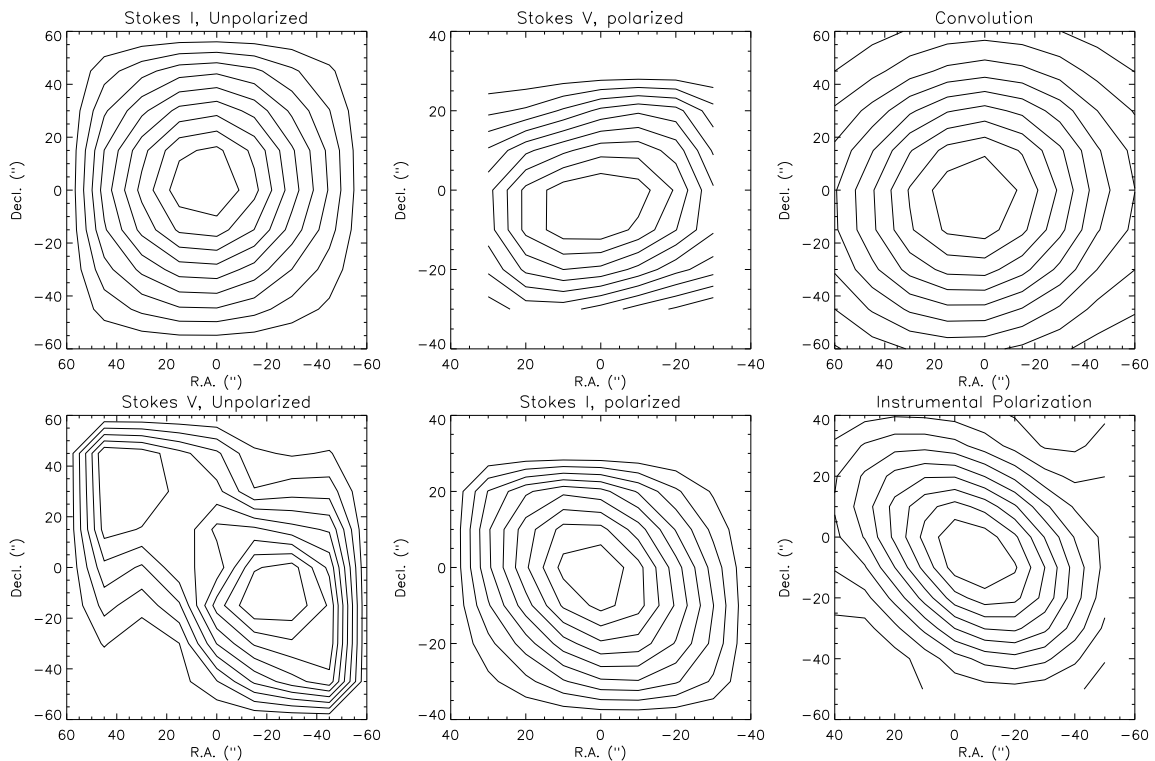


Fig. 3.7.— Sequence of products from twelve cycles of simulated data involved in establishing the amount of instrumental polarization. Each map is displayed on axes of Right Ascension and Declination offsets from $[0, 0]$ along the horizontal and vertical, respectively. The left-most column shows Stokes I (*top*) and V (*bottom*) for the unpolarized standard (maxima 0.05 and 7.3×10^{-4} K km s $^{-1}$), which are convolved with Stokes V and I , respectively, of the polarized source (maxima 3.6 and 101.5 K km s $^{-1}$), shown to their immediate right. The final column at the right gives the corresponding convolution products of the two maps along the top row (maximum 2.2 K km s $^{-1}$), where the plot on the bottom right is the deduced IP (maximum 0.85 K km s $^{-1}$). In all panels contours are spaced at intervals of 10% of the peak intensities.

Assured that we have successfully been able to remove the effects of pointing

errors, Table 3.1 aggregates the results of individually including sidelobes and a flat polarization level with an unpolarized source. The numbers represent averages of the central 3×3 data points of the final, deconvolved product. Although the input source polarization is consistently recovered to a level better than before the implementation of Equations (3.7)-(3.11), the performance is much better for a flat polarization that offsets the two maps comprising a cycle. The most likely explanation for not seeing any further improvement is that the size of the maps, chosen to mimic our data, are not large enough in order to completely characterize the sidelobes that may be lying at the outer edges, away from the source. It is also possible that some uncertainty in the absolute pointing of our source could reduce our ability to account for sidelobe polarization. That is, our alignment technique only corrects for relative misalignments between maps, but not for the absolute positioning of the reference map in relation to that of the unpolarized source used to characterize the beam. The final row of Table 3.1 presents an average of ten runs of twelve cycles, each incorporating all sources of IP and also $3''$ pointing errors. Here we were careful to again correct for beam squint, something that was not done for the sidelobe and flat IP tests in the table.

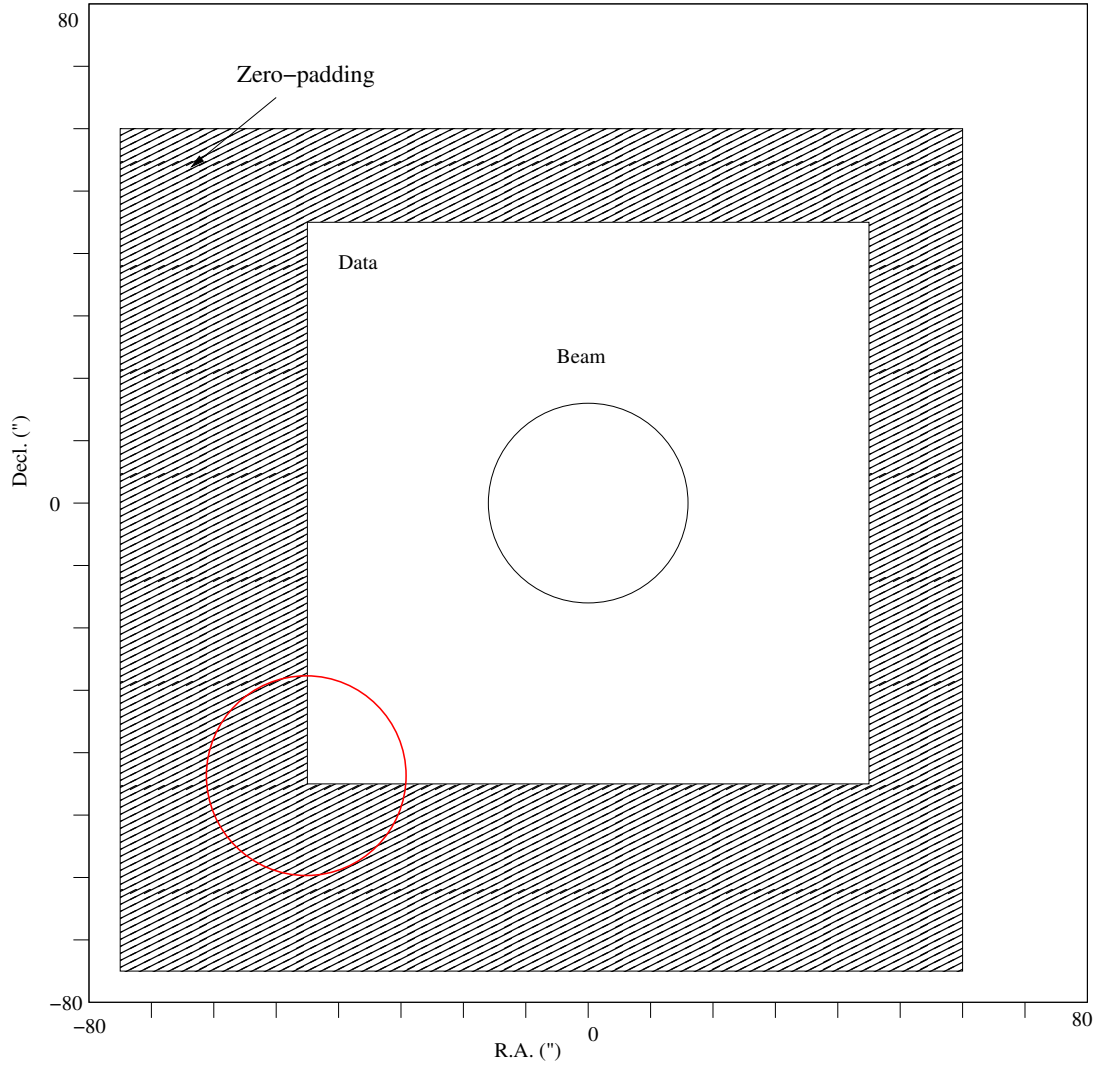


Fig. 3.8.— Schematic of the footprint of our simulated data both prior to (white square) and after zero-padding (hatched square). The CSO beam size is indicated by the circle, neatly constrained by the size of the data. The displaced red beam illustrates how the beam can potentially overlap the zero-padded, “no-data” region, while also including the actual data.

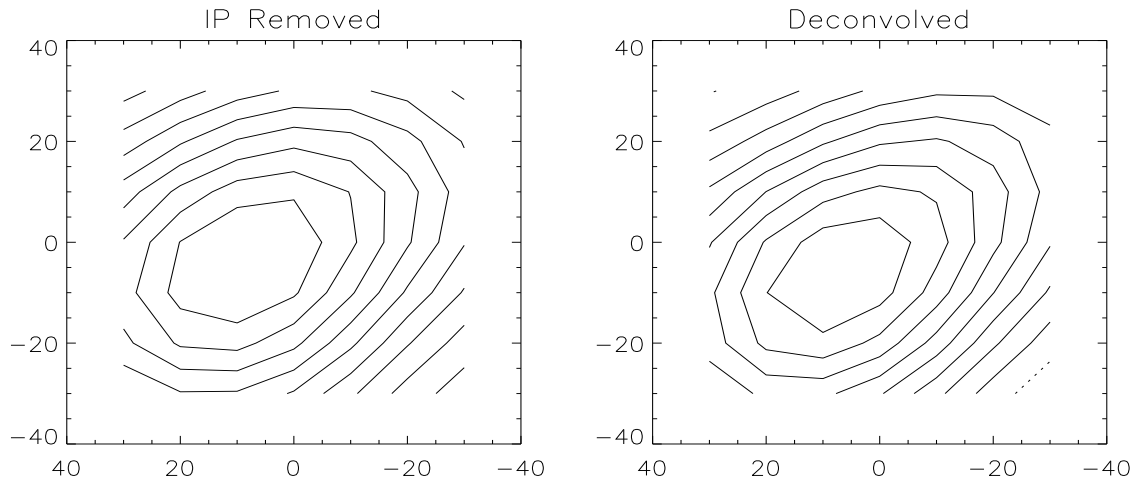


Fig. 3.9.— (*Left*) Stokes V map of our simulated source (maximum 1.4 K km s^{-1}) upon removal of the instrumental polarization, shown in the bottom right of Figure 3.7. (*Right*) The same data product upon deconvolving G_0 , the unpolarized Stokes I product in the top left panel of Figure 3.7 (maximum 2.0 K km s^{-1}). Contours are spaced in intervals of 10% of the peak intensity.

It is important to note that our technique for IP correction works best at points in the centre of our source map. This result is expressed in Figure 3.10, the top panel of which shows the percent polarization recovered for each of the map’s data columns, averaged over the central three points. The same procedure is applied to the data showcased in the bottom panel, but for the Stokes V data alone. In each case it is apparent that the centre, ~ 2 columns nearest approach the expected amount of polarization. Although there is a consistent increase in percent polarization across the map, the variation in each direction is approximately equal, similar to the behaviour seen in the bottom panel. Also noticeable in the top panel is an increase in the uncertainties of the points at the extreme ends, columns zero and six, an indication of the smaller number of valid data points that go into these averages due to pointing adjustments, as alluded to previously. Depending on the direction of misalignment,

Table 3.1: Results of simulations as separated by the type of instrumental polarization, as added to an unpolarized source (but for the last row, where the source is 2% polarized). All numbers are averages of the central 3×3 data points, where the aligning algorithm has been disabled for the sidelobe and flat polarization tests. The final row shows the average of ten runs with a $3''$ pointing error, a 2% sidelobe, and a 2% flat polarization on top of a flat, 2% source polarization. The uncertainty given is the variance about the results from the ten runs.

		Before (%)	After (%)	Error (%)
Sidelobes	1%	0.36	0.18	0.021
	2%	0.39	0.18	0.021
	3%	0.42	0.18	0.021
Flat Level	-1%	-1.00	0.036	0.021
	1%	1.00	0.038	0.021
	2%	2.00	0.073	0.021
	3%	3.00	0.110	0.021
All Together		4.33	1.66	0.31

the terminating columns would need to extrapolate to areas outside the map's bounds. The exclusion of these extrapolated data leads to higher uncertainty on the map edges.

Another detrimental effect due to the zero-padding of our maps further lessens the quality of the data on the edges. As shown in Figure 3.8, performing a convolution near the edges of a map, as needed in Equation (3.10) to apply our IP-removal technique, will include locations when no data are present. That is, at these positions one is forced to use zero data from the padded region instead of the real, missing, data from the source. This is an important shortcoming when dealing with maps of finite sizes that do not reach regions where the intensity of the source is negligible. We are therefore forced to exclude rows and columns at the edges of our maps and disregard the polarization levels measured there when analyzing our data.

The fact that we are adequately able to retrieve our input polarization is confirmed

in the spectral data themselves, shown in Figure 3.11. Reclaiming a spectrum from the deconvolved polarization map of Figure 3.9 meant applying the same series of convolutions shown in Figure 3.7, but on pre-selected velocity bins of data. Rather than integrating across the entire Gaussian spectrum, we produced a contour plot for each 1 km s^{-1} bin from 0 to 10 km s^{-1} from our simulated source spectra at each offset position. The unpolarized target, as it will be seen in the continuum, was exactly identical to the data that we have already shown. The top panel of Figure 3.11 shows the original input Stokes I spectrum for the centre position of the map, and therefore of the highest intensity. Overlaid upon it is the recovered, binned, spectrum having had the IP removed and G_0 deconvolved. We also identify 3σ (filled circles), V/I detections across the spectrum at approximately the 2% level. The bottom panel includes the Stokes V spectrum at the same 1 km s^{-1} resolution. This ability to retrieve spectra for any mapped position will be put to further use in the next chapter when we introduce real circular polarization data.

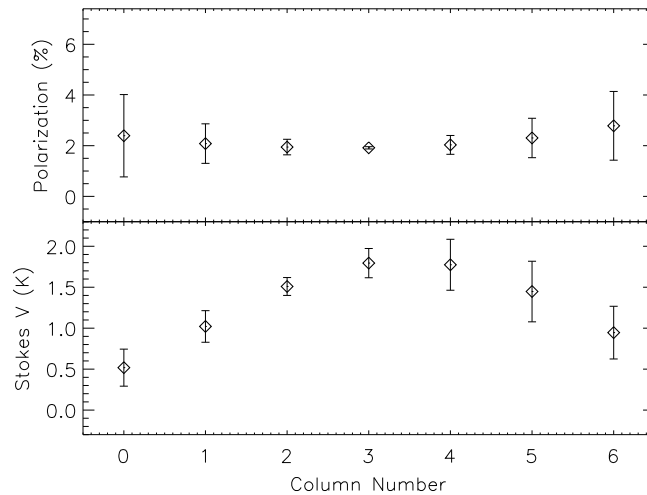


Fig. 3.10.— Variation in polarization levels across the final map product expressed as a percentage (*top*) and the Stokes V signal alone (*bottom*). Each diamond represents an average of the centre three points in the column at each R.A. position.

3.5 Conclusion

This chapter has established both the source of, and the means to account for, artificial polarization that can adversely affect the Four-Stokes-Parameter Spectral-Line Polarimeter at the Caltech Submillimeter Observatory. Comprehensive simulations of a weakly circularly polarized source have been created that include likely manifestations of IP, and pointing errors of a size commensurate with actual observations. We have used twelve pairs of intensity contour maps, each with one left-circularly polarized and one right-circularly polarized dataset, of both an unpolarized standard and an elliptical source of a flat, uniform polarization constructed from Gaussian spectra. The centre-most point of the source data has an SNR of ~ 71 . In order to ensure the spatial alignment of all of the maps, we cross-correlated all of the data with the same reference and charted the decrease in polarization before and after alignment, noting a significant improvement on an unpolarized source. Then, to remove other forms of IP contaminations, we applied an augmented technique based upon that of Hezareh et al. (2013). Overall, the algorithm adequately accounts for each type of IP, as verified in a series of tests that separated the effects of sidelobes, and a flat, constant level of polarization on our ability to recover an initially unpolarized source. Our primary simulation, combining these types of IP with a $3''$ pointing error, resulted in the recovery of a $1.6 \pm 0.31\%$ polarization level on a 2% flat input, where $4.3 \pm 0.29\%$ remained after beam squint correction. The methods of this chapter will therefore be applied with confidence on the circular polarization data of OMC-2 FIR 4, to be presented in the next chapter.

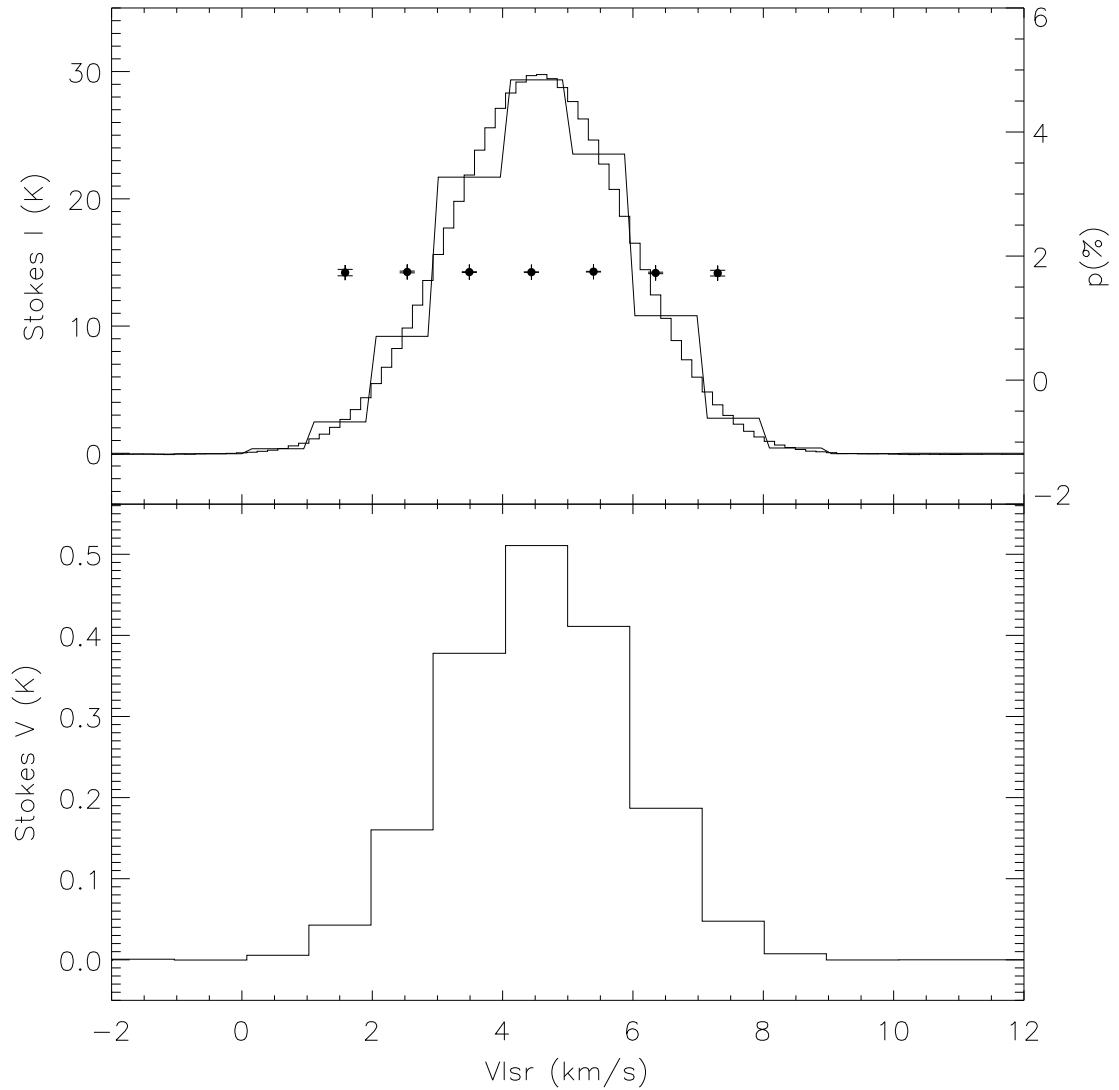


Fig. 3.11.— Stokes I (*top*) and V (*bottom*) spectra upon correction for instrumental polarization for the centre position of the simulated map from the right panel of Figure 3.9. The recovered spectra, in 1 km s^{-1} bins, are displayed, along with Stokes I , prior to the removal of any IP. Identified 3σ polarization detections are overplotted in the top panel as filled circles, at the percentage level given on the right-most axis.

- Born, M., & Wolf, E. 1999, Principles of optics, 7th edn. (Cambridge University Press)
- Chu, T., & Turrin, R. 1973, IEEE Trans., AP-21, 339
- Condon, J., Cotton, W., Greisen, E., et al. 1998, AJ, 115, 1693
- Conway, R., & Kronberg, P. 1969, MNRAS, 142, 11
- Crutcher, R., Troland, T., Goodman, A., et al. 1993, ApJ, 407, 10
- Crutcher, R. M., Troland, T. H., Lazareff, B., Paubert, G., & Kazés, I. 1999, ApJ, 514, L121
- Davis, C., Dent, W., Matthews, H., Coulson, I., & McCaughrean, M. 2000, MNRAS, 318, 952
- Falgarone, E., Troland, T., Crutcher, R., & Paubert, G. 2008, A&A, 487, 247
- Glenn, J., Walker, C., Bieging, J., & Jewell, P. 1997, ApJ, 487, L89
- Goldreich, P., & Kylafis, N. 1981, ApJ, 243, L75
- Greaves, J., Holland, W., & Dent, W. 2002, ApJ, 578, 224
- Heiles, C. 1997, ApJS, 111, 245
- . 2001, PASP, 113, 1243
- Heiles, C., Perillat, P., Nolan, M., et al. 2001a, PASP, 113, 1247
- . 2001b, PASP, 113, 1274
- Hennebelle, P. 2013, A&A, 556, A153
- Hezareh, T., & Houde, M. 2010, PASP, 122, 786

- Hezareh, T., Wiesemeyer, H., Houde, M., Gusdorf, A., & Siringo, G. 2013, *A&A*, 558, 45
- Hildebrand, R., Dotson, J., Dowell, C., Schleuning, D. A., & Vaillancourt, J. 1999, *ApJ*, 516, 834
- Houde, M., Akeson, R., Carlstrom, J., et al. 2001, *PASP*, 113, 622
- Houde, M., Hezareh, T., Jones, S., & Rajabi, F. 2013, *ApJ*, 764, 24
- Kildal, P.-S., Olsen, E., & Anders, J. 1988, *IEEE Transaction on Antennas and Propagation*, 36, 182
- Klein, B. J., & Degnan, J. J. 1976, *Applied Optics*, 15, 977
- Kooi, J. W., Chamberlin, R. A., Monje, R. R., et al. 2014, *IEEE Trans. on Terahertz Science and Technology*, 4, 149
- Kudoh, T., & Basu, S. 2008, *ApJ*, 679, L97
- MacLow, M.-M., & Klessen, R. 2004, *Rev. Mod. Phys.*, 76, 125
- Mouschovias, T. 2001, *ASP*, 248, 515
- Nakamura, F., & Li, Z.-Y. 2005, *ApJ*, 631, 411
- Ng, T., Landecker, T., Cazzolato, F., et al. 2005, *Radio Science*, 40, RS5014
- Padoan, P., & Nordlund, A. 1999, *ApJ*, 526, 279
- Rohlfs, K., & Wilson, T. 2000, *Tools of Radio Astronomy* (Springer Berlin Heidelberg)
- Rybicki, G., & Lightman, A. 1979, *Radiative processes in astrophysics* (Wiley & Sons)
- Sault, R., Hamaker, J., & Bregman, J. 1996, *A&A SS*, 117, 149
- Stahler, S. W., & Palla, F. 2004, *The Formation of Stars* (Wiley-VCH)

Thum, C., Wiesemeyer, H., Paubert, G., Navarro, S., & Morris, D. 2008, PASP, 120, 777

Trippe, S. 2014, JKAS, 47, 15

Troland, T., & Heiles, C. 1982, ApJ, 252, 179

Uson, J. M., & Cotton, W. 2008, A&A, 486, 647

Verschuur, G. 1969, ApJ, 156, 861

Chapter 4

The Detection of Non-Zeeman

Circular Polarization of CO

Rotational Lines in OMC-2 FIR 4¹

4.1 Introduction

Magnetic fields have been suspected to influence the star formation scenario as it unfolds within molecular clouds (Mouschovias 2001), slowing, or even preventing, the free-fall collapse of gaseous condensations. The signatures of this are likely to be imprinted by way of polarizing the radiation emanating from dust grains and/or the polarization of spectral lines. In the former case, the elongated grains will align themselves with their long axes perpendicular to the magnetic field lines, imparting a linear polarization onto any background starlight. Thermal emission will also be linearly polarized, divulging the orientation of the plane-of-the-sky component of the magnetic field.

More subtle are the effects that lead to linear or circular polarization levels in

¹From Jones, S. C., Houde, M., and Hezareh, T. 2015, ApJ, to be submitted

molecular lines. Only the Zeeman effect, which relies on the splitting of a spectral line into two symmetrically shifted, elliptically polarized σ -components and an unshifted, linearly polarized π -component, can lead to a direct determination of the field strength (usually the line-of-sight component). Normally, the fields present within molecular clouds are not sufficient to affect a line splitting and instead cause a line broadening. The result is a net circular polarization manifested as a signature antisymmetric Stokes V profile, which is fit to the derivative of the corresponding Stokes I profile to deduce the magnitude of the magnetic field along the line-of-sight (Crutcher et al. 1999, 1993).

The linear polarization of molecular lines arises as a result of an anisotropic distribution of radiation in the pervading medium. Known as the Goldreich-Kylafis effect (Goldreich & Kylafis 1981), this can be caused either by an anisotropic external source of radiation, or differences in velocity gradients in the gas in directions parallel and perpendicular to the magnetic field. In general, however, in the end they can lead to an imbalance in the populations of magnetic sublevels, of quantum number M , the transitions between which produce the π -($\Delta M = 0$) and σ -($\Delta M = \pm 1$) lines. The former will manifest as radiation polarized parallel to the magnetic field, while the latter will be perpendicular. The prevailing linear polarization will then be determined based upon which of the two transitions dominates.

Recently, (Houde et al. 2013) measured the circular polarization of ^{12}CO ($J = 2 \rightarrow 1$) in Orion KL at the Caltech Submillimetre Observatory (CSO), an unexpected result given the low sensitivity of this species to any Zeeman broadening. They attributed the detection to anisotropic resonant scattering of background radiation states polarized parallel and perpendicular to the magnetic field direction (in the plane of the sky) by foreground molecules. As a result, incident, linearly polarized radiation acquires a relative phase shift between the orthogonal, scattered components, such that the output, observable radiation becomes partially circularly polarized. Thereafter,

Hezareh et al. (2013) firmly established that the aforementioned CO circular polarization can be ascribed to a conversion of linear polarization from the background molecules. The authors were able to insert the detected CO circular polarization signal into the corresponding linear polarization, which was found to completely align the CO linear polarization vectors with that of the dust, confirming the scattering conversion process. A follow-up paper (Houde 2014) then applied this model to SiO $v = 1$ and $v = 2$ masers frequently found in evolved stars. This work proved that incorporating anisotropic resonant scattering from molecules beyond the velocity range of the maser allows one to account for any resulting shape of the Stokes V spectrum and obtain a match to the observed Stokes V spectral lines.

Here we will present circular polarization maps of ^{12}CO ($J = 2 \rightarrow 1$) emission in the OMC-2 FIR 4 molecular cloud, part of the larger Orion A star-forming complex. This source is unique in that it is the site of a severe case of rather poorly understood dust depolarization (Houde et al. 2004; Matthews et al. 2004) with increasing 350 μm continuum flux. More generally, the source is also exceptionally devoid of any significant polarization. Houde et al. (2004) found a Stokes-averaged polarization level of $0.35 \pm 0.08\%$ in OMC-2 FIR 4 with the Hertz polarimeter at the Caltech Submillimetre Observatory, relative to $0.73 \pm 0.14\%$ and $0.91 \pm 0.28\%$ in nearby OMC-2 FIR 3 and OMC-2 FIR 6, respectively. Although this runs counter to the results of Hull et al. (2014) for ^{12}CO ($J = 2 \rightarrow 1$) as obtained with CARMA, the discrepancy can be rationalized by noting that the Hertz beam may have captured a large range of widely varying polarizations. Also, measurements from an interferometer such as CARMA can yield higher polarization levels because of the well-known missing flux issue in Stokes I of interferometry. It remains to be discerned whether these effects carry over to molecular line emission, the relevance of which is important to determine the physical basis for depolarization. For example, should the linear polarization levels of ^{12}CO ($J = 2 \rightarrow 1$) remain unaffected, then it is likely that properties of the

dust are alone responsible for the depolarization. If instead a similar depolarization phenomenon is observed in the molecular lines, then it is more probable that some external effect is driving the depolarization, such as a tangling of the magnetic field lines. Another possibility for the reduction of linear polarization levels could be the aforementioned transfer of linear polarization to circular polarization first observed, and predicted, by Houde et al. (2013) and confirmed by Hezareh et al. (2013) in SNR IC 443. In the end, this polarization conversion process also calls for changes in the orientation (or tangling) of the magnetic field along the line of sight.

The paper is broken down as follows: in §2 we describe our observations; in §3 we detail the data analysis that we were required to perform to properly quantify the amount of instrumental polarization inherent to our data; the results are summarized in §4, and put into context given the consequences for depolarization in §5. Finally, we conclude in §6.

4.2 Observations

We used the Four-Stokes-Parameter Spectral-Line Polarimeter (FSPPol) (Hezareh & Houde 2010) at the Caltech Submillimetre Observatory to acquire our circular polarization data over nine nights in January 2013. FSPPol is comprised of two side-by-side frequency specific wave plates, a half-wave plate (HWP) to measure linear polarization, and a quarter-wave plate (QWP) to measure circular polarization. The instrument is placed in the elevation tube prior to the receiver, where it can be independently controlled from the CSO control room. As the CSO receiver can only measure a single polarization at a time, the two wave plates must be rotated through four (two) distinct angles to completely describe the linear (circular) polarization states. A more detailed explanation of this technique is provide in Chapter 3 (§3.2) of this thesis.

We acquired our circular polarization maps of the ^{12}CO ($J = 2 \rightarrow 1$) transition at 230.538 GHz in OMC-2 FIR 4 (R.A.[J2000] = $05^{\text{h}}35^{\text{m}}26^{\text{s}}.7$, decl.[J2000] = $-05^{\circ}10'1''.0$) in January 2013. With FSPPol, the primary advantage of producing maps in excess of the $32''$ FWHM beam size is that we are able to quantify, and hopefully later remove any spurious contributions by polarized sidelobes in the outskirts of the beam. Overall, the data were collected under a wide range of sky condition, under stable weather ($0.06 < \tau_{225} < 0.19$). A total of 26 cycles, or pairs of integrations, were acquired, at QWP angles of $\theta = \pm 45^{\circ}$, with θ defined as the angle of the wave plate from the axis of polarization at the receiver (see Hezareh et al., 2010 and Chapter 3 of this thesis). In this manner, integrations taken at $\theta = +45^{\circ}$ transpose the right-handed circular polarization (I_{RCP}) onto the north-south axis of the receiver (on the sky), while those at $\theta = -45^{\circ}$ capture the left-handed circular polarization (I_{LCP}). Stokes I and V are then realized as $I = I_{\text{LCP}} + I_{\text{RCP}}$ and $V = I_{\text{RCP}} - I_{\text{LCP}}$, respectively, as per the IAU convention.

The maps are $70'' \times 70''$ with each integration separated by $10''$ in each of Right Ascension and Declination. We moved across the sky at a speed of $1''/\text{s}$, resulting in an on-source integration time of 10 s at each position. The off-source reference position was located at a spacing of one degree in azimuth from the center of each row, while a temperature calibration was taken at the start of each map and after each row of integrations was completed. In this way we can be assured that any fluctuation in gain calibration between polarization measurements is minimized, at least barring any significant changes in sky conditions from one row to the next (~ 1 minute in duration). The spectra themselves have a resolution of 0.159 km/s (0.122 MHz). System temperatures (T_{sys}) varied from $\simeq 300$ K at transit to $\simeq 500$ K at lower ($\simeq 30^{\circ}$) elevations. Upon approximately every two cycles a pointing check was rendered on a bright, nearby standard, often taken to be Jupiter. Meanwhile, for purposes of quantifying the amount of polarization contributed by FSPPol and the

surrounding optics or the beam of the CSO, we also mapped an unpolarized source at the outset of each night. In January 2013, this source was Jupiter, for a total of 4 measurement cycles. These maps were of a coarser resolution of $15''$ and a larger size of $105'' \times 105''$. Half as much time (5 s) was spent at each position, while due to the more restricted source extent, the off-position was only $300''$ away.

4.2.1 OMC-2 FIR 4

The Orion A molecular cloud is home to several well-studied star-forming regions. Among these, OMC-1 lies directly behind the Orion Nebula, while OMC-2 and OMC-3 are about $15'$ and $20'$ north (Castets & Langer 1995), respectively. A lot of the appeal of this region is the colocation of several stages in the star formation paradigm. Observations of the OMC 2/3 subregion have revealed 26 dusty cores from 1.3 mm continuum emission (Nielbock et al. 2003) plus 33 in $850 \mu m$ emission (Lis et al. 1998). Meanwhile, in the infrared, there has been a wealth of work put into the discovery of a set of young stars (Jones et al. 1994; Ali & DePoy 1995), often still with their natal discs. One of the signposts of protostellar evolution, CO molecular outflows, has also been confirmed here (Takahashi et al. 2008).

The OMC-2 cloud is host to a multitude of protostars, among which FIR 4 appears to be the brightest in the submillimetre (Mezger et al. 1990). As a prototypical class 0 source (Reipurth et al. 1999), FIR 4 has an integrated luminosity of $400 L_{\odot}$ and an envelope mass of $35 M_{\odot}$ (Crimier et al. 2009). Two envelope components have been identified through dust continuum and molecular line observations, one with a temperature of 40 K and another, colder component at about 15 K (Mezger et al. 1990; Johnstone et al. 2003).

Located between OMC-3 MMS 8-9 and OMC-2 FIR 6, FIR 4 is unique for its paucity of dust continuum polarization. Additionally, it seems to bridge a boundary

where the polarization angles (PAs) of these two regions abruptly change from $\sim 115^\circ$ in OMC-2 FIR 6 to $\sim 175^\circ$ in OMC-2 FIR 3. This appears to possibly coincide with the location of a strong outflow (Williams et al. 2003). Houde et al. (2004) measured HCN and HCO⁺ spectra of the ($J = 4 \rightarrow 3$) transition at several positions in Orion A to find the inclination angle of the magnetic field relative to the line-of-sight. They achieved this by combining dust continuum polarization data from the CSO with ion-neutral line width comparisons from the aforementioned molecular species (Houde et al. 2002). Ultimately, they arrived at an inclination of $\approx 80^\circ$, which deviated little from findings in the nearby OMC-2 and OMC-3 regions.

4.3 Data Processing

The ¹²CO ($J = 2 \rightarrow 1$) spectral line at each mapped position spans approximately 4 to 18 km s⁻¹ with significant broadening at the peak. Our maps were thus created by integrating across this velocity range and a two-dimensional intensity image produced. Our first area of concern was in assuring that all maps lay at the same spatial position relative to a chosen reference dataset (see Chapter 3). In general, we found small pointing differences for our OMC-2 FIR 4 maps of less than 0".5, increasing to 3 – 5" for Jupiter. Once these were corrected, by way of cross-correlating each map with the reference standard and interpolating to the peak, it became imperative to properly assess the amount of unwanted polarization as contributed by the optics of FSPPol and the CSO, and the telescope beam. These effects are normally manifest as a mixing of the Stokes parameters as signal is leaked from Stokes I to Stokes V .

Specifically, potential IP contamination is thought to come from three sources, beyond the pointing inconsistencies which we can account for through the aforementioned cross-correlation/map-alignment process: polarized sidelobes in the outer areas of the beam structure, unwanted (oblique) reflections, possibly from the tertiary mir-

ror, and imperfect gain calibrations between the right- and left-circularly polarized data. We have assumed that the latter is mitigated by frequent temperature calibrations that determine the antenna temperature prior to any corrections for telescope beam efficiencies and we can reasonably expect it to cancel out over many observations. The removal of the remaining two sources of IP have been extensively tested using simulated source data of a priori known polarization (see Chapter 3). In what follows we will summarize the technique that has been applied towards the removal of the IP, having enhanced that put forward by Hezareh et al. (2013).

The methods of Hezareh et al. (2013) were developed in an effort to identify linear and non-Zeeman circular polarization signals in ^{12}CO ($J = 2 \rightarrow 1$) spectral lines of the supernova remnant IC 443. For an ideal receiver response, the measured flux $S_{i,\text{src}}$ can be given by the convolution (*) product

$$S_{i,\text{src}} = B_{i,\text{src}} * P_0 \quad (4.1)$$

for any Stokes parameter I , Q , U or V , as referenced by the indices $i = 0, 1, 2, 3$. Additionally, $B_{i,\text{src}}$ is the true signal on the sky in the corresponding Stokes parameter and P_0 is the normalized beam profile. Any potential IP contributions are then summarized in the additional terms for $i = 1, 2, 3$ for, respectively, leakage of Stokes I signal into one of the other Stokes parameters, and possible oblique reflections, etc., parameterized by R_i

$$S_{i,\text{src}} = B_{i,\text{src}} * P_0 + B_{0,\text{src}} * P_i + R_i (B_{0,\text{src}} * P_0). \quad (4.2)$$

We must somehow remove these terms from $S_{i,\text{src}}$ in order to recover $B_{i,\text{src}} * P_0$. To this end, an unpolarized standard source must be observed so as to best characterize the telescope beam and any remaining instrumental polarization. For this purpose we have used observations of Jupiter collected regularly over the observing run. In

January 2013, the planet was at nearly peak phase (0.996), with a diameter of $\Theta_J = 45''.8$ on the sky, which is resolved within the $32''$ beam of the CSO at the ^{12}CO ($J = 2 \rightarrow 1$) transition frequency. As per Hezareh et al. (2013), if we define the profile $G_0 = N_{0,J} * P_0$, where $N_{0,J}$ is the normalized Stokes I profile of Jupiter, then the corresponding Jupiter profiles for the other Stokes parameters, and specifically Stokes V , result from

$$G_i = N_{0,J} * P_i + R_i * G_0, \quad (4.3)$$

where R_i has been incorporated from Equation (4.2). Taking the convolution of $S_{i,\text{src}}$ in Equation (4.2) with G_0 yields

$$S_{i,\text{src}} * G_0 = (B_{i,\text{src}} * P_0) * G_0 + S_{0,\text{src}} * S_{i,J}, \quad (4.4)$$

where $S_{i,J}$ is the corresponding Stokes map of Jupiter and $S_{0,\text{src}}$ the Stokes I of our source, OMC-2 FIR 4. For our purposes, the second term on the right-hand side of Equation (4.4) will then become the convolution of Stokes V of Jupiter with the Stokes I of OMC-2 FIR 4, a measure of the instrumental polarization. In order to obtain the real source polarization map, this term is subtracted from the left-hand side of the equation. Finally, we deconvolve G_0 from our remaining map using a simple Wiener filter. The results of this analysis will be presented in the following section.

The relevant Stokes maps for Jupiter, at 1.3 mm (230 GHz) and upon the aggregation of all four cycles, are shown in Figure 4.1. These correspond to a V/I at map center of $\approx -0.5\%$, but exceeding -3% at the map edges. During alignment, a row and/or column at the furthest edge in the direction in which the map needs to be shifted cannot be trusted, as an extrapolation would be necessary to recover the data here. The resulting reduction of data implies that these extremities are also

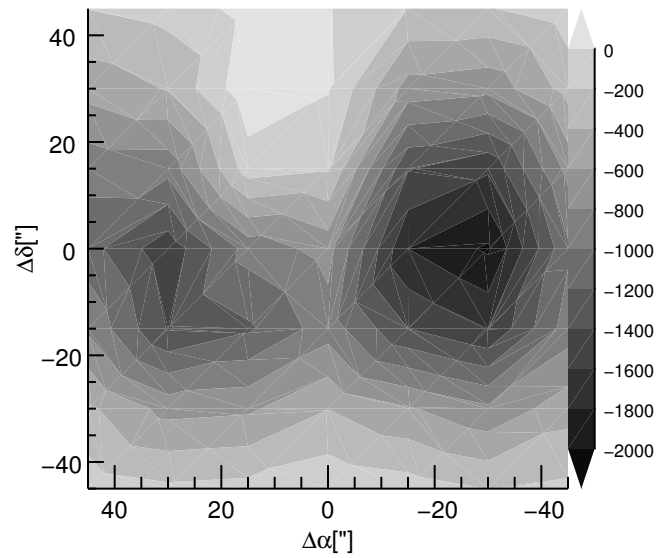
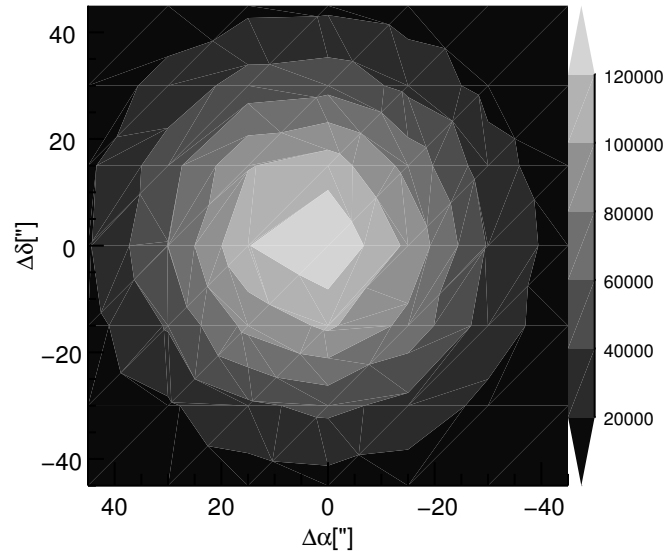


Fig. 4.1.— Integrated intensity maps of Jupiter in Stokes I (top) and V (bottom) at 1.3 mm (230 GHz) for a spectrum spanning a v_{lsr} from -640 km s^{-1} to 660 km s^{-1} . The grey scale on the right of each figure has units of K km s^{-1} .

subject to higher uncertainties in the aggregated map. The remaining adjustment required prior to IP removal is to rotate the Jupiter Stokes maps to the parallactic angle of OMC-2 FIR 4 for every set of observations, since the CSO telescope beam is unchanging, as the receiver rotates in elevation with the rest of the telescope.

4.4 Results

In Figure 4.2 we present the Stokes V and I maps of OMC-2 FIR 4 integrated across the ^{12}CO ($J = 2 \rightarrow 1$) spectral line, having aggregated all 26 cycles. The SNR across each of the maps comprising a single cycle varies from ~ 2.4 at the map edges to ~ 89 at the center. The Stokes V map has been corrected for instrumental polarization and the telescope beam deconvolved to recover the original $32''$ FWHM resolution of the map. As shown in Figure 4.3, the IP peaks towards the center of the map at $\approx -1.4\%$, while the final product (Figure 4.2 (bottom)) reaches a maximum value of $\approx 1.59 \pm 0.05\%$.

In Figure 4.4 we show the Stokes I and V spectra retrieved from the IP-corrected contour map of OMC-2 FIR 4 at an [R.A.,Decl.] offset of $[-20'', 10'']$ from the map center. The same algorithm outlined in Equations (4.1)-(4.4) has been successively applied to a series of 1 km s^{-1} spectral velocity bins comprising the entire width of the ^{12}CO ($J = 2 \rightarrow 1$) line. In the discussion that follows, the polarization p is defined as $p = V/I$ while its uncertainty is $\sigma_p = \sqrt{1 + p^2} \sigma_V / I$. The filled data points represent $3\sigma_p$ Stokes V detections. In Figures 4.5 and 4.6 we present the same datasets for every position of the OMC-2 FIR 4 map, that is, Stokes I and V , respectively. The Stokes I intensity peaks at a temperature of $T_A^* = 35 \text{ K}$ in the fourth column and seventh row of the stamp, i.e. at an [R.A.,Decl.] offset of $[0'', -30'']$. In each panel there are a multitude of $3\sigma_p$ detections, generally exhibiting very low levels of polarization ($< 0.5\%$). The shapes of the Stokes V spectra vary widely, in both intensity and

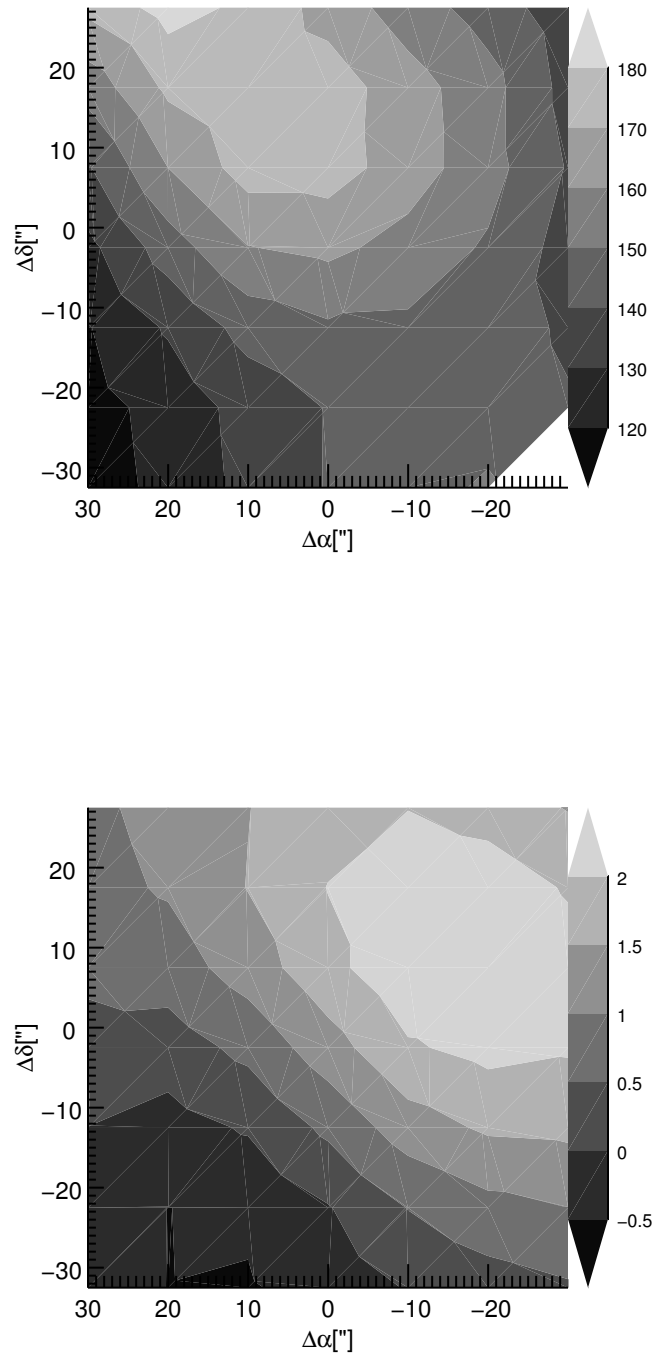


Fig. 4.2.— Stokes I (top) and V (bottom) polarization maps of ^{12}CO ($J = 2 \rightarrow 1$) in OMC-2 FIR 4. The maps have been adjusted such that they are centered at (R.A.[J2000] = $05^{\text{h}}35^{\text{m}}27^{\text{s}}.0$, decl.[J2000] = $-05^{\circ}10'3''.5$), the “FIR 4 clump” position chosen by Shimajiri et al. (2008). The grey scale on the right of each graph is scaled in units of K km s^{-1} .

degree of symmetry. We will use this fact to inform upon the resonant scattering model of Houde et al. (2013; 2014) in the following Section.

4.5 Discussion

The structure of contours shown in the OMC-2 FIR 4 Stokes I map compares favorably to a much broader map made by Chini et al. (1997), who separately parsed the $4.0 - 8.0 \text{ km s}^{-1}$ blue-shifted and $14.0 - 18.0 \text{ km s}^{-1}$ red-shifted components. Although we overlap less with their velocity intervals, which were chosen to map the outflow from FIR 3, there is still some structural similarity. The same is true with contours of the ^{12}CO ($J = 3 \rightarrow 2$) and ^{12}CO ($J = 1 \rightarrow 0$) transitions, as presented by Shimajiri et al. (2008), where the elongation in a northeast-southwest direction is preserved in the same direction as the outflow propagates.

The model that we ultimately hope to test with the observations presented here was used by Houde et al. (2013) to explain the circular polarization identification recorded at the CSO in ^{12}CO ($J = 2 \rightarrow 1$) in 2011. For weakly Zeeman sensitive molecules such as this, they were able to prescribe an anisotropic resonant scattering scenario whereby background linearly polarized radiation strikes foreground molecules, changing the incoming polarization state. A population of molecules, aligned with the magnetic field, can become linearly polarized through the Goldreich-Kylafis effect (Goldreich & Kylafis 1981). Once this radiation encounters molecules of a similar species in the line of sight aligned with a relatively rotated magnetic field, it is scattered with a relative phase shift ϕ between the two radiation states parallel, $|n_{\parallel}\rangle$, and perpendicular, $|n_{\perp}\rangle$, to the magnetic field, establishing circular polarization. Following Houde et al. (2013) and Houde (2014) an incident radiation signal, $|\psi\rangle$, given by

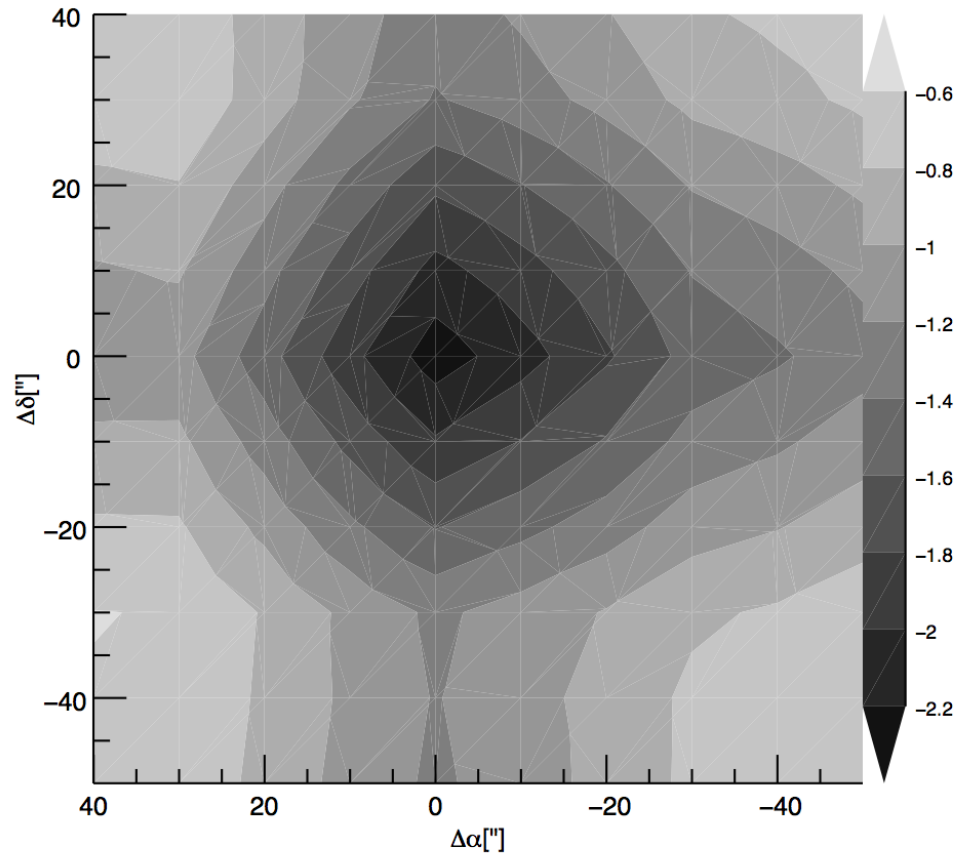


Fig. 4.3.— Instrumental polarization map removed from Stokes V map in the top panel of Figure 4.2. As alluded to in Equation (4.4), deduced from the convolution of the Stokes I of OMC-2 with the Stokes V of Jupiter, the unpolarized standard.

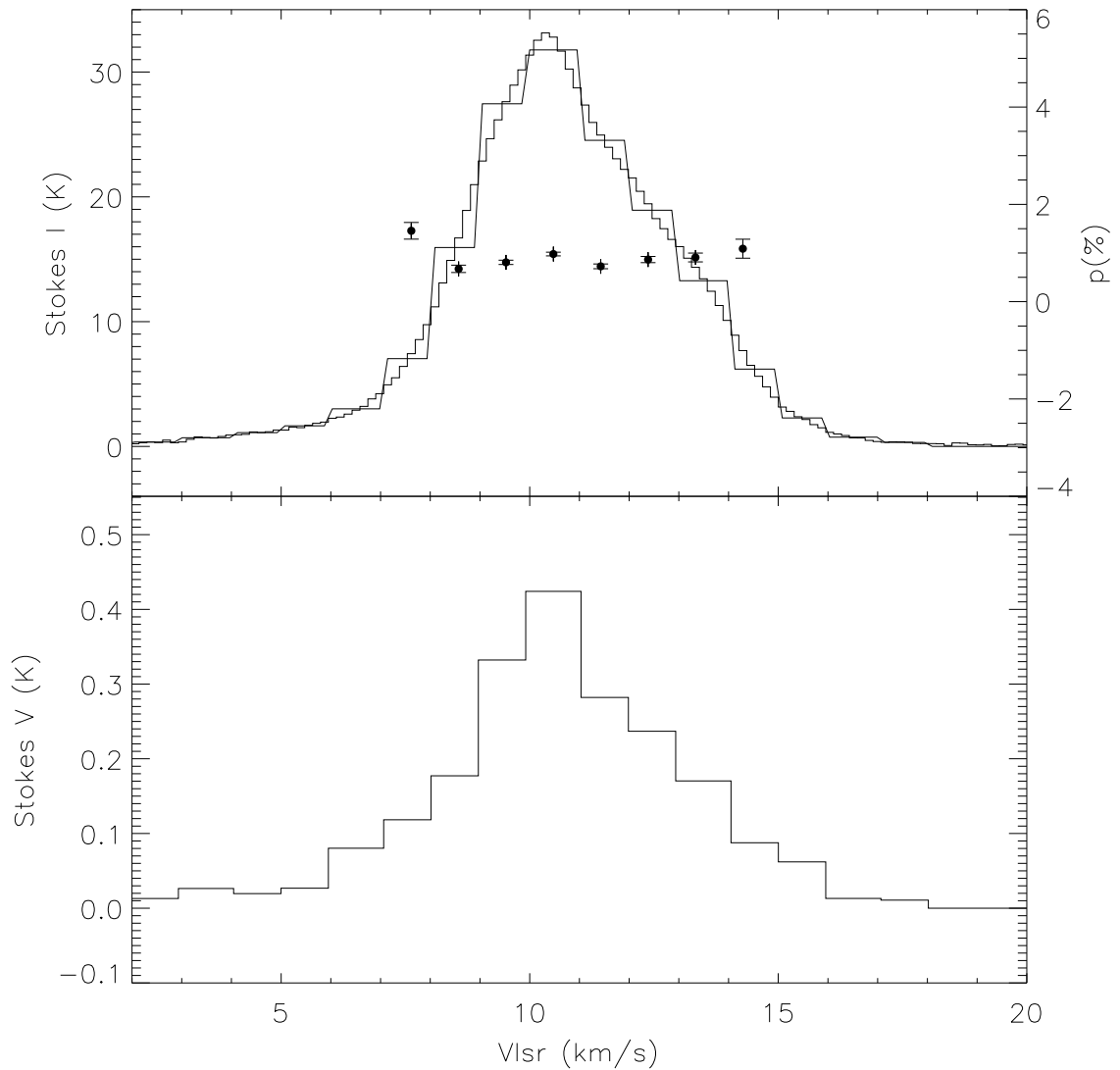


Fig. 4.4.— Stokes I (top) and V (bottom), using the corresponding scales on the left, for the position [R.A., Decl.] = $[-20'', 10'']$ from the center coordinate. We present both the full-resolution Stokes I spectrum and its counterpart binned to 1 km s^{-1} , prior to deconvolution. The closed circles on the top panel represent a fractional polarization, $p = V/I$, where $p \geq 3\sigma_p$, using the scale on the right. Neither dataset has been corrected for telescope efficiency.

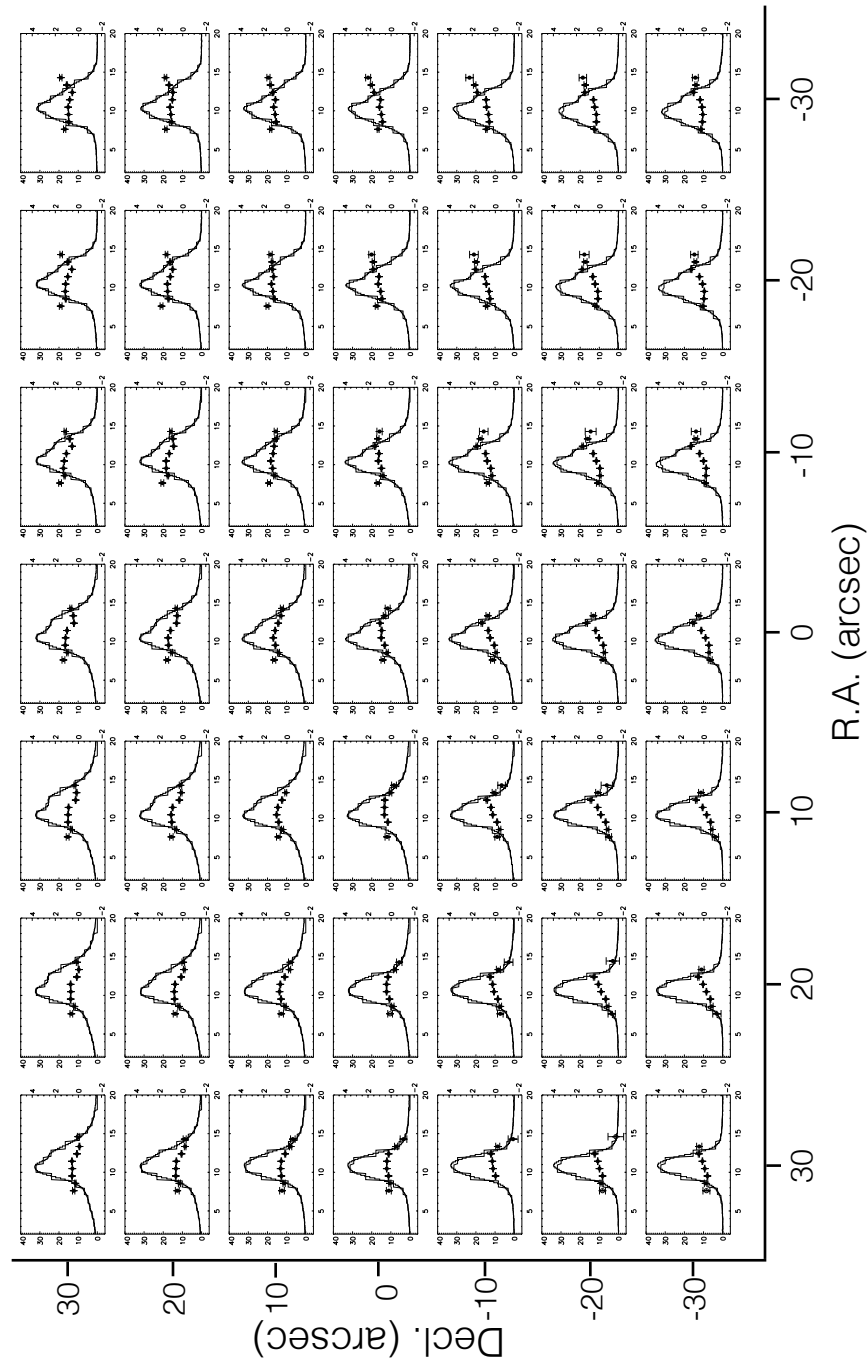


Fig. 4.5.— Stokes I spectra, using the scale on the left, for each offset position from OMC-2 FIR 4 at (R.A.[J2000] = $05^{\text{h}}35^{\text{m}}26^{\text{s}}.7$, decl.[J2000] = $-05^{\circ}10'1''.0$). Instances of a $3\sigma_p$ circular polarization detection are given by filled circles while open circles indicate $2\sigma_p$ detections using the scale on the right. These spectra are presented again, uncorrected for telescope efficiency.

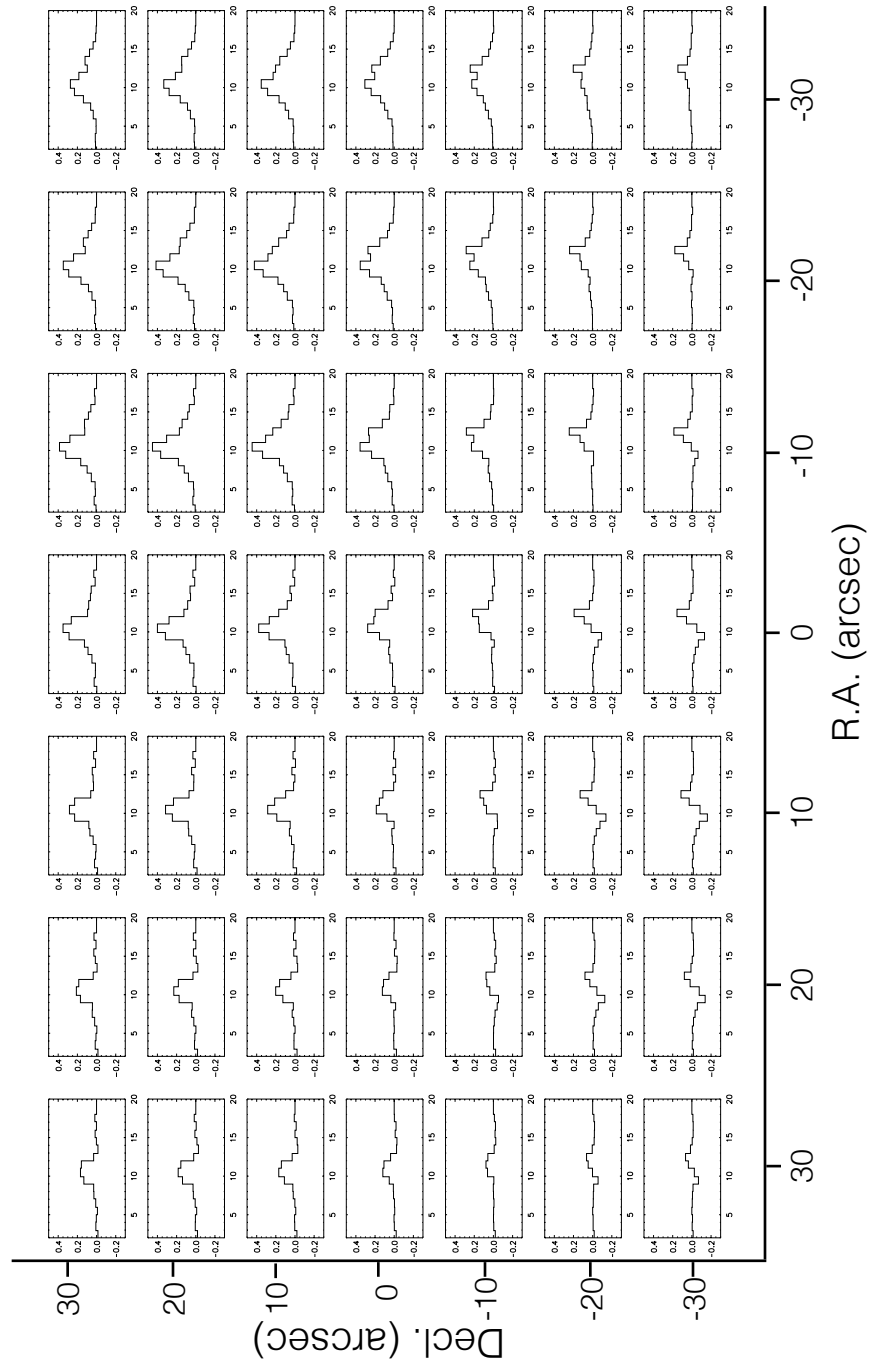


Fig. 4.6.— Stokes V spectra for each offset position from OMC-2 FIR 4 at (R.A.[J2000] = $05^{\text{h}}35^{\text{m}}26^{\text{s}}.7$, decl.[J2000] = $-05^{\circ}10'1''.0$). All datasets are uncorrected for telescope efficiency.

$$|\psi\rangle = \alpha|n_{\parallel}\rangle + \beta|n_{\perp}\rangle, \quad (4.5)$$

where $\alpha = \cos(\theta)$ and $\beta = \sin(\theta)$ and θ representing the polarization angle relative to the foreground magnetic field, the new, scattered state $|\psi'\rangle$ becomes

$$|\psi'\rangle \simeq \alpha e^{i\phi}|n_{\parallel}\rangle + \beta|n_{\perp}\rangle. \quad (4.6)$$

In a reference frame with the $\theta = 0$ and $\pi/2$ axes, respectively, parallel and perpendicular to the magnetic field, the Stokes parameters used to describe the polarization state upon scattering are,

$$q = \alpha_0^2 - \beta_0^2 \quad (4.7)$$

$$u = 2\alpha_0\beta_0 \cos(\phi) \quad (4.8)$$

$$v = 2\alpha_0\beta_0 \sin(\phi) \quad (4.9)$$

where, again, v adheres to the IAU convention. Therefore, if ϕ were to be set to zero, we would then recover the Stokes parameters of the incident radiation, q_0 , u_0 and $v_0 = 0$, prior to scattering. With these definitions we then have

$$q = q_0 \quad (4.10)$$

$$u = u_0 \cos(\phi) \quad (4.11)$$

$$v = u_0 \sin(\phi). \quad (4.12)$$

From Equations (4.10)-(4.12), it is then clear that it is in fact the Stokes U radiation that is being transferred to Stokes V as the relative phase shift ϕ widens, while Stokes Q and I proceed through the cloud unaltered. The phase shift was shown to be a function of the frequency of the incident radiation, ω , as well as several other physical parameters. That is,

$$\phi(\omega) \simeq \omega_z^2 \sin^2(\iota) \tau \mathcal{V}_{\text{int}} \frac{ng_1 e^{-E_1/kT_{\text{ex}}}}{Q(T_{\text{ex}})} \times \frac{3\pi c^3 A_{\text{ul}}}{4\hbar\omega_0^3 \omega^2} \sqrt{u(\omega)u'(\omega)} I(\omega) \quad (4.13)$$

where

$$I(\omega) = \int \{x^2(x - \omega) [3(x - \omega)^2 - \gamma_{\text{ul}} - \omega_z^2] / [(x - \omega)^2 + \gamma_{\text{ul}}^2] + (x - \omega)(\omega^2 - 3x^2) + \gamma_{\text{ul}}^2(3x - \omega) + \omega_z^2(x + \omega)\} \frac{h(x)}{\Delta} dx. \quad (4.14)$$

and $\Delta = [(x + \omega_z - \omega)^2 + \gamma_{\text{ul}}^2] [(x - \omega_z - \omega)^2 + \gamma_{\text{ul}}^2]$. In these two equations, ω_0 is the frequency for the transition between the upper (u) and lower (l) energy levels of the π -transition, ω_z is the Zeeman splitting affected by the foreground magnetic field, γ_{ul} is the relaxation rate of a transition between u and l for the scattering molecules (of density n), A_{ul} is the Einstein coefficient for this same transition, $u(\omega)$ and $u(\omega')$ are the energy densities of the incident (u_0 as described earlier) and scattered radiation, respectively, $h(x)$ is the spectral profile of the molecules comprising the scattering populations and ι is the inclination of the foreground magnetic field as referenced to the line of sight. Further, g_1 is the degeneracy corresponding to the energy level E_1 for the population of scattering molecules in the lower energy state, while for an excitation temperature of T_{ex} the conditions are of LTE and the partition function

is given by Q . Finally, \mathcal{V}_{int} is the volume of interaction between the incident and scattered radiation, i.e. where the scattering actually occurs. The time available for scattering, τ , is then based upon the rate of relaxation intrinsic to the background emitters.

Upon closer inspection of Figure 4.6, it becomes apparent that there are at least three distinct shapes that the Stokes V spectra can assume. Towards positive Right Ascension and negative Declination, at approximately [R.A., Decl.] = [10'', -20''], the spectra have a clear antisymmetric profile, or ‘‘S’’-shape, reminiscent of the traditional Zeeman effect (Crutcher et al. 1999). Meanwhile, directly opposite this, to more negative R.A. and positive Decl. ([-10'', 20'']), not only is there a strong increase in spectral intensity, but now the profile has become almost completely symmetric. Finally, as one moves from here to larger R.A. offsets, at about [20'', 20''], the Stokes V intensity falls off, while at the same time there is a noticeable negative shoulder on the red side of the peak, at $\sim 13 \text{ km s}^{-1}$. Each of these example profiles were almost identically reproduced by Houde (2014) using the aforementioned anisotropic resonant scattering model of Houde et al. (2013), for observations made by Cotton et al. (2011) of SiO $v = 1$ and $v = 2$, ($J = 1 \rightarrow 0$) masers (43.1 GHz and 42.8 GHz, respectively) in the AGB star IK Tau. Here we seek to further validate the resonant scattering model by attempting to match the symmetric and antisymmetric Stokes V scenarios from Figure 4.6 from known physical data of our source, OMC-2 FIR 4.

For both the emitting and scattering regions we have taken representative parameters for our source of $T_{\text{gas}} = 35 \text{ K}$ (Furlan et al. 2014), $n_{\text{H}_2} = 4 \times 10^3 \text{ cm}^{-3}$ (Castets et al. 1990) and a plane of the sky magnetic field strength of $B_{\text{pos}} = 80 \mu\text{G}$, which does not differ exceedingly from the value deduced by Poidevin et al. (2010) of 130 μG . Supplying these values to the Houde et al. (2013) model, we have created two Stokes V spectra, given in Figures 4.7 and 4.8. In each plot, the incident linearly polarized radiation $u(v)$ is given by the dashed profiles and has been set to an inten-

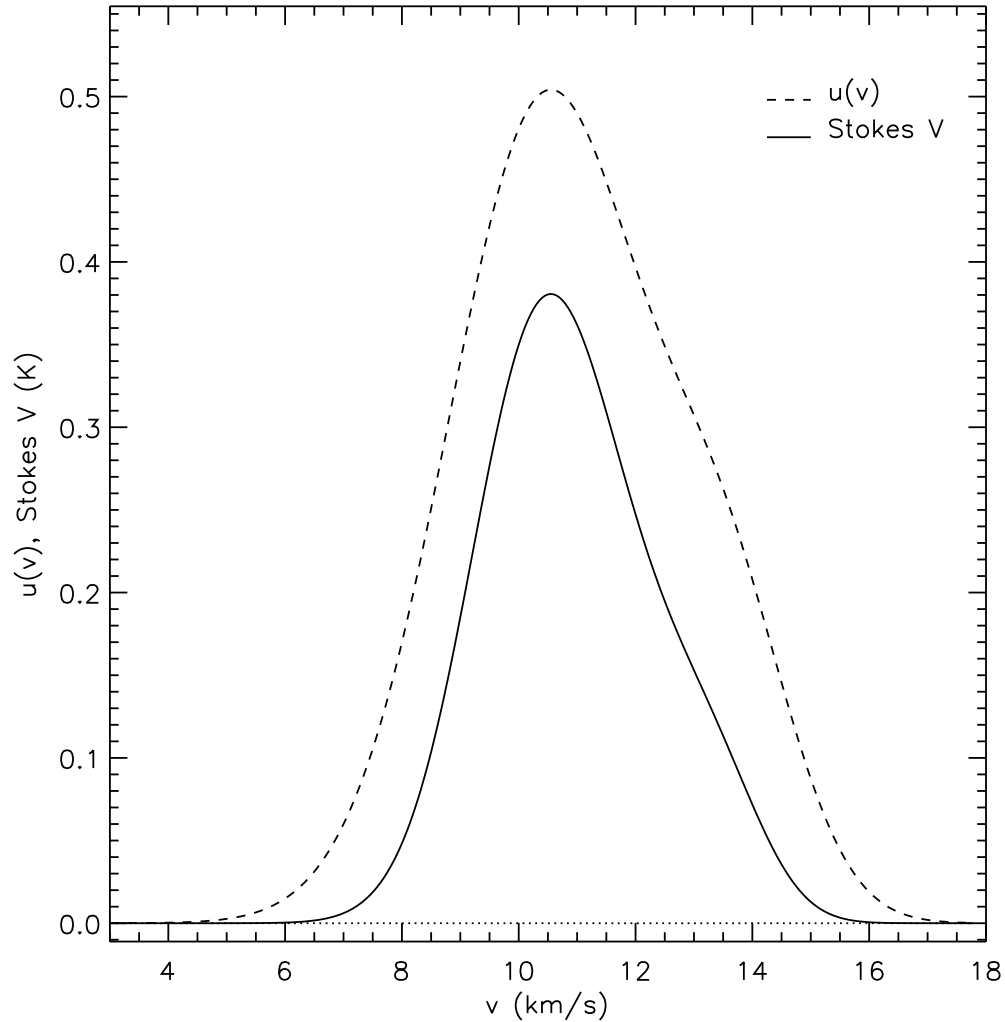


Fig. 4.7.— Circular polarization spectra for the ^{12}CO ($J = 2 \rightarrow 1$) transition as rendered by the anisotropic resonant scattering model of Houde et al. (2013). The dashed dataset is for the incident, linearly polarized radiation, while the solid spectrum is Stokes V after scattering from the foreground molecules. Within the model, every incident photon scatters off molecules occupying a volume of $(5 \text{ AU})^3$ located at a velocity of 1 km s^{-1} from it, spread over a Gaussian-distributed FWHM of 0.5 km s^{-1} . The remaining parameters are set such that $n_{\text{H}_2} = 4 \times 10^3 \text{ cm}^{-3}$, $T_{\text{ex}} = 35 \text{ K}$ and $B_{\text{pos}} = 80 \mu\text{G}$.

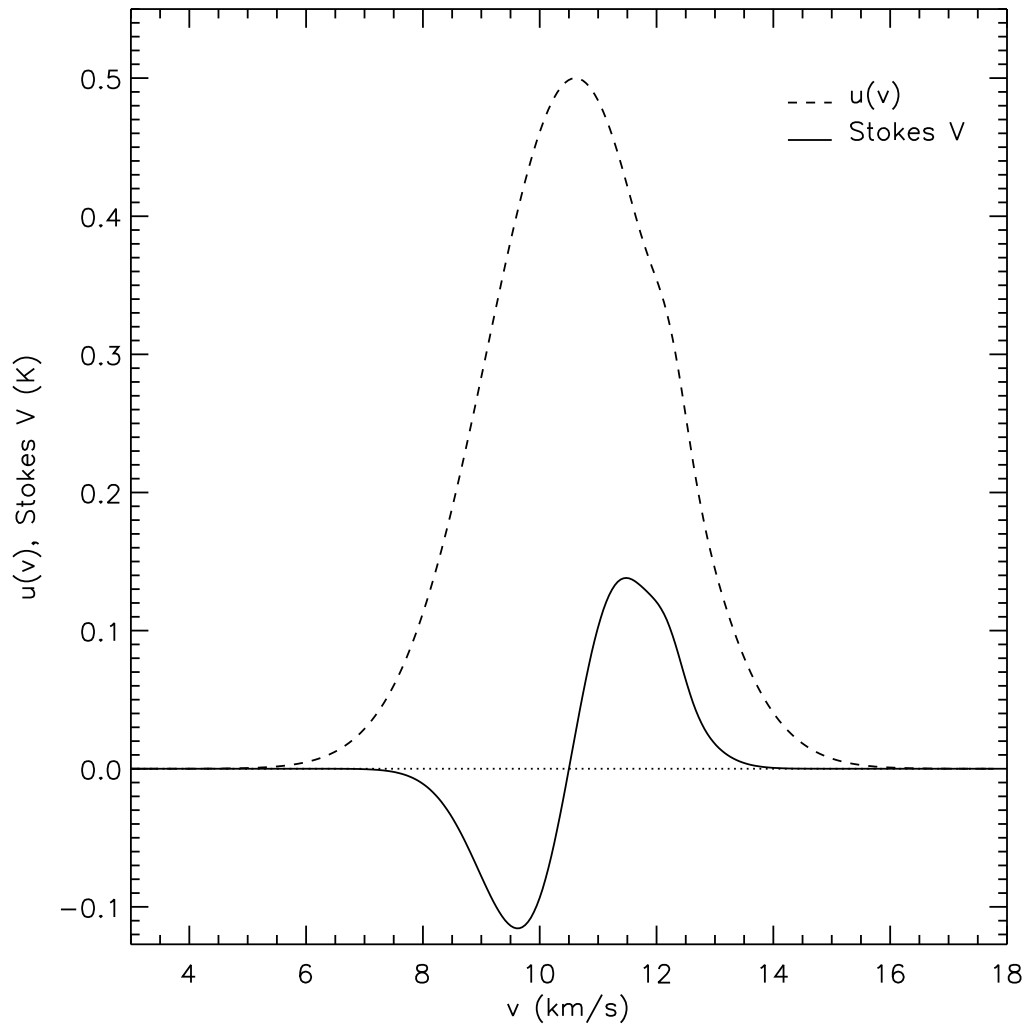


Fig. 4.8.— Same as Figure 4.7 but for scatterers occupying a volume of $(10 \text{ AU})^3$ at a fixed velocity of 0.5 km s^{-1} , spread over a Gaussian-distributed FWHM of 5 km s^{-1} .

sity approximately similar to our Stokes V spectra, and a shape akin to the Stokes I spectra, at the relevant position in Figure 4.6. The linear polarization orientation of the incident radiation was set at 45° from that of the foreground magnetic field, for simplicity. In Figure 4.7, the solid spectrum proceeds from scattering from a volume of $(5 \text{ AU})^3$ and with a Gaussian-distributed breadth of 0.5 km s^{-1} FWHM, located at a velocity separation of 1 km s^{-1} from every photon. In this way we are able to mimic a velocity gradient in the gas that varies with the depth of the cloud along the line of sight, which can produce the observed symmetric Stokes V Zeeman spectra (Houde 2014). This is a feature of the Houde et al. (2013) resonant scattering model that exceeds the capabilities of the Zeeman model – to be able to go back and forth between symmetric and antisymmetric profiles. It must be stated that there is large amount of flexibility in the model’s parameters, leading to a number of conditions whereby the same spectrum can be produced. Importantly, the precise nature of the scattering distribution is not very important. Instead their densities are much more relevant, something that was stated also in Houde et al. (2014).

4.6 Conclusion

We have detected circular polarization signals in the ^{12}CO ($J = 2 \rightarrow 1$) molecular line in the OMC-2 FIR 4 cloud, previously notable for its lack of continuum polarization (Houde et al. 2004). This work was undertaken with the aim of further testing the linear to circular polarization conversion process put forward by Houde et al. (2013) and later further substantiated observationally by Hezareh et al. (2013). In the analysis towards making such a judgment, the quantification of an IP signal became critically important. To this end, we have utilized a rigorous IP removal algorithm based upon the convolution with an unpolarized standard, here chosen to be Jupiter. Subsequently, in our integrated intensity contour maps, a peak circular polarization

of $1.59 \pm 0.05\%$ was found. We went on to recover the spectra themselves at each mapped position by applying the same IP-removal algorithm for a series of narrow velocity bins across the extent of the spectral line. While we managed to secure several detections, generally, the majority of these detections were at a less than 0.5% level. Many of the shapes of the Stokes V spectra mirrored those previously produced by Houde (2014) using the anisotropic resonant scattering model of Houde et al. (2013). Here we showed that this model is successful in mimicking any of the desired symmetric, antisymmetric, or quasi-symmetric cases given a reasonable magnetic field strength of $80 \mu\text{G}$.

- Ali, B., & DePoy, D. 1995, *AJ*, 109, 709
- Castets, A., Duvert, G., Dutrey, A., et al. 1990, *A&A*, 234, 469
- Castets, A., & Langer, W. 1995, *A&A*, 294, 835
- Chini, R., Reipurth, B., Ward-Thompson, D., et al. 1997, *ApJ*, 474, L135
- Cotton, W., Ragland, S., & Danchi, W. 2011, *ApJ*, 736, 96
- Crimier, N., Ceccarelli, C., Lefloch, B., & Faure, A. 2009, *A&A*, 506, 1229
- Crutcher, R., Troland, T., Goodman, A., et al. 1993, *ApJ*, 407, 10
- Crutcher, R., Troland, T., Lazareff, B., Paubert, G., & Kazes, I. 1999, *ApJ*, 514, L121
- Furlan, E., Megeath, S., Osorio, M., et al. 2014, *ApJ*, 786, 26
- Goldreich, P., & Kylafis, N. 1981, *ApJ*, 243, L75
- Hezareh, T., & Houde, M. 2010, *PASP*, 122, 786
- Hezareh, T., Wiesemeyer, H., Houde, M., Gusdorf, A., & Siringo, G. 2013, *A&A*, 558, A45
- Hildebrand, R. H., Kirby, L., Dotson, J. L., Houde, M., & Vaillancourt, J. E. 2009, *ApJ*, 696, 567
- Houde, M. 2014, *ApJ*, 795, 27
- Houde, M., Dowell, C. D., Hildebrand, R. H., et al. 2004, *ApJ*, 604, 717
- Houde, M., Hezareh, T., Jones, S., & Rajabi, F. 2013, *ApJ*, 764, 24
- Houde, M., Bastien, P., Dotson, J. L., et al. 2002, *ApJ*, 569, 803

- Hull, C., Plambeck, R., Kwon, W., et al. 2014, *ApJ SS*, 213, 13
- Johnstone, D., Boonman, A., & van Dishoeck, E. 2003, *A&A*, 412, 157
- Jones, T., Mergen, J., Odewahn, S., et al. 1994, *AJ*, 107, 2120
- Kildal, P.-S., Olsen, E., & Anders, J. 1988, *IEEE Transaction on Antennas and Propagation*, 36, 182
- Lis, D., Serabyn, E., Keene, J., et al. 1998, *ApJ*, 509, 299
- Matthews, B., Wilson, C., & Fiege, J. 2004, *ApJ*, 562, 400
- Mezger, P., Zylka, R., & Wink, J. 1990, *A&A*, 228, 95
- Mouschovias, T. 2001, *ASP*, 248, 515
- Nielbock, M., Chini, R., & Muller, S. 2003, *A&A*, 408, 245
- Poidevin, F., Bastien, P., & Matthews, B. 2010, *ApJ*, 716, 893
- Reipurth, B., Rodríguez, L., & Chini, R. 1999, *AJ*, 118, 983
- Shimajiri, Y., Takahashi, S., Takakuwa, S., Saito, M., & Kawabe, R. 2008, *ApJ*, 683, 255
- Takahashi, S., Saito, M., Ohashi, N., et al. 2008, *ApJ*, 688, 344
- Williams, J., Plambeck, R., & Heyer, M. 2003, *ApJ*, 591, 1025

Chapter 5

Conclusion and Future Plans

As the continuing evolution of modern instrumentation enables deeper and more resolved insights into shrouded natal stellar environs, the study of the point at which gravitational attraction overcomes resisting forces becomes clearer. While the question of whether magnetic fields or turbulent motions provide the dominant opposition has not been resolved, this thesis has taken an incremental step towards qualifying the role that the former might play. The focus has been on different subregions of the Orion Molecular Cloud (OMC), which is of a sufficiently large size to be host to a varied assemblage of stages in the star formation process. While not all observations have resulted in a firm strength of the magnetic field, each of the middle three chapters has addressed the problem in a unique enough way so as to promise further advancements toward this end goal.

Most typically, magnetic fields have been inferred from the alignment of the smallest interstellar dust grains, with their long axes perpendicular to the field lines. As a result, measurements of this kind are very dependent on an accurate knowledge of the velocity dispersions and densities of the surrounding gas. Furthermore, it is important to have a handle on the uniformity of these parameters across the cloud as any perversions can lead, additionally, to polarization of molecular lines vis-à-vis

the Goldreich-Kylafis effect. In Chapter 2 we sought to establish whether such a scenario is occurring in the Kleinmann-Low nebula of the OMC, in particular within the newly discovered $J_{K_{-1}K_1} = 5_{32} - 4_{41}$ transition of the ortho- H_2O maser. We detected this transition with *Herschel*/HIFI to not be polarized to a 3σ upper limit of $\sim 2\%$. These results were complicated by the presence of a broad pointing-driven pedestal component that changed in magnitude from one observing epoch to the next, and had to be removed prior to searching for any polarization. Puzzlingly, we were not able to reconcile this result with coeval observations at the same spatial location of the 22 GHz $J_{K_{-1}K_1} = 6_{16} - 5_{23}$ transition with the 30-m Effelsberg radio receiver, where polarization levels of $\sim 15\%$ at the same line-of-sight velocity were recorded. A nearby maser spot at $\sim 7.2 \text{ km s}^{-1}$ recorded even higher levels of $\sim 75\%$, which, while not unsubstantiated in the literature, the physics of such a discrepancy have not been unraveled.

The focus of the remainder of the thesis centred on observations made at the CSO with FSPPol, a frequency-specific wave plate polarimeter, that has previously been used to make pointed observations of molecular lines. Here we chose to extend these capabilities to the production of small maps about OMC-2 FIR 4, a protostellar region notable for a lack of polarization relative to surrounding sources. This allowed us to, for the first time, measure the relevance of any FSPPol contributions to the total measured polarization signal, here in the abundant ^{12}CO ($J = 2 \rightarrow 1$) molecular transition. In collecting a series of intensity maps, it became possible to examine the structure of the CSO beam off-source, as is hypothesized to be affected by polarized sidelobes. We employed a technique put to use by Hezareh et al. (2013), who, through a series of convolutions of source data and that from an unpolarized point source, was able to remove the instrumental polarization (IP) afflicting their observations. The efficacy of these methods on our data from the CSO was verified in Chapter 3, where we have presented a comprehensive set of simulations and tested

our ability to recover an input source polarization upon accounting for all possible types of IP. In general, we struggle most when dealing with polarized sidelobes that encircle the beam centre, but are able to very cleanly eliminate a polarization meant to mimic the effect of unanticipated reflections from the tertiary mirror and elsewhere. However upon combining all sources of IP, including random pointing errors arising from inconsistencies in sky conditions, a 2% flat polarization is redeemed within the calculated uncertainties.

The polarization levels imparted by sidelobes are likely not of a magnitude to be especially concerning. One conclusion of our simulations is that the method of Hezareh et al. (2013) is most effective when attacking IP-levels significantly in excess of the source polarization that we try to recover. We see this as we increase the amount of sidelobe polarization relative to the amount that is removed. This is also borne out by the result of incorporating all sources of IP at once, equivalent to $\sim 1.6\%$, whereafter nearly all of this is eradicated. More subtly, while we are able to align all maps to the same reference data set, thereby eliminating any relative pointing errors, it may be that there remains an absolute pointing offset between this reference and the unpolarized standard map that we use to represent our beam. We hope to model the effects of this scenario at a later date.

Chapter 4 adopts the methods of Chapter 3 to arrive at a peak circular polarization level of $\approx 1.59 \pm 0.05\%$. The recovered spectra include many $3\sigma_p$ detections at all 49 mapped positions often at a $< 0.5\%$ level. In the future we hope to also substantiate the linear-to-circular polarization conversion process effected by the anisotropic resonant scattering model of Houde et al. (2013), in OMC-2 FIR 4, by obtaining linear polarization data at the same frequency. Using representative physical parameters for the region and a magnetic field strength of $80 \mu\text{G}$, we were able to obtain any Stokes V spectral shape using this same model.

A further test of the non-Zeeman resonant scattering effect (Houde et al. 2013)

may be provided by simultaneous linear and circular polarization data, that did not make it into this thesis, but which were collected with the EMIR/XPOL setup at IRAM in May 2013. All of the existing, aforementioned techniques can be reused with confidence for each of ^{12}CO ($J = 2 \rightarrow 1$) and $J = (1 \rightarrow 0)$ as well as ^{13}CO ($J = 1 \rightarrow 0$).

Appendix A

Summary of Herschel/HIFI and Effelsberg Observations

Table A.1: Summary of HIFI observations conducted in 2011 and 2012.

Observation Number	Observation Day (OD)	Observation ID (ObsID)	Date	System Temperature T_{sys} (K) (V/H)	Position Angle ^a PA (°)	Mode
1V/H	666	1342215918-9	2011 Mar 3	97/98	266.2	OTF Mapping
2V/H	666	1342215920-1	2011 Mar 3	97/97	266.2	OTF Mapping
3V/H	681	1342216838-9	2011 Mar 26	97/97	273.6	Pointed
4V/H	694	1342218904-5	2011 Apr 8	97/98	280.0	Pointed
5V/H	1017	1342239637-8	2012 Feb 25	68/84	258.9	Pointed
6a-V/H	1066	1342244409-10	2012 Apr 14	68/84	284.1	Pointed
6b-V/H	1066	1342244411-2	2012 Apr 14	68/84	284.1	OTF Mapping

^aPosition of the HIFI vertical polarisation axis relative to north, increasing eastward.

Table A.2: Summary of Effelsberg observations conducted in 2011 and 2012.

Observation Number	Date	System Temperature T_{sys} (K) (V/H)	Parallactic Angle (PA) ($^{\circ}$)	Mode
1a-V/H	2011 Mar 21	91/81	6.1	Pointing
1b-V/H	2011 Mar 21	115/103	28.9	Pointing
2a-V/H	2012 Mar 21	108/95	-30.3	Pointing
2b-V/H	2012 Mar 21	134/117	37.0	Pointing
3a-V/H	2012 Apr 18	94/81	19.2	Pointing
3b-V/H	2012 Apr 18	136/118	34.9	Pointing

Appendix B

Herschel/HIFI Maps of 621 GHz

Water Maser

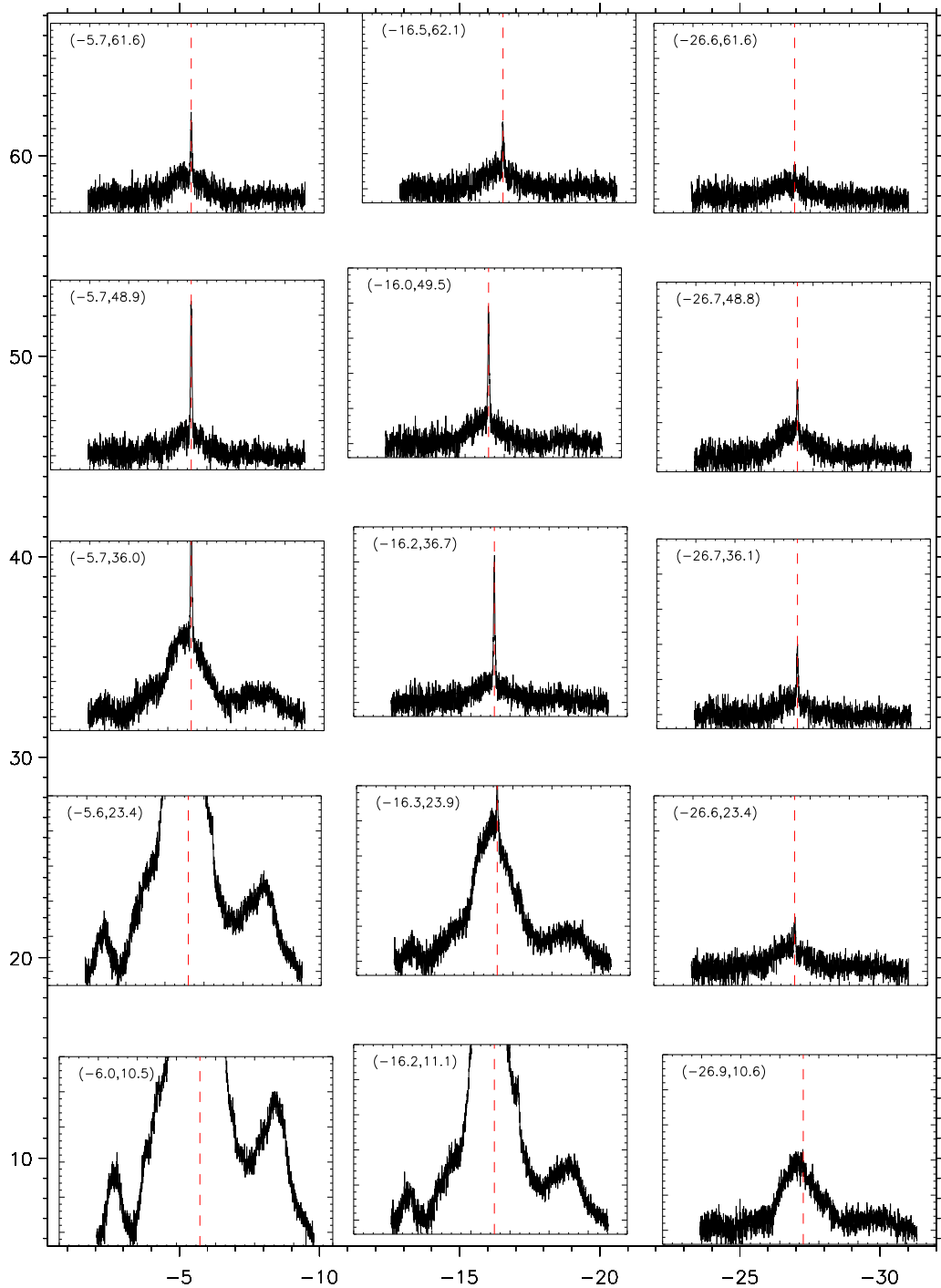


Fig. B.1.— Map of 621 GHz emission corresponding to dataset 2-H in Table A.1. The offsets from (R.A.[J2000]= 05^h35^m14^s.3, decl.[J2000]= -05°22'33".7) are given in the upper left of each panel in seconds of arc. The horizontal and vertical axes bordering the entire set of 15 panels correspond roughly to these respective offsets for the positions at which the spectra shown in the individual panels were observed. The fine vertical scales on the individual panels, run from $[-0.2$ to $2.5]$ degrees Kelvin; the width of the individual panels cover a V_{lsr} range of $[-60$ to $80]$ km s⁻¹ roughly centered on the vertical red line marking $V_{lsr} = 12$ km s⁻¹, the velocity of the narrow 621 GHz maser feature.

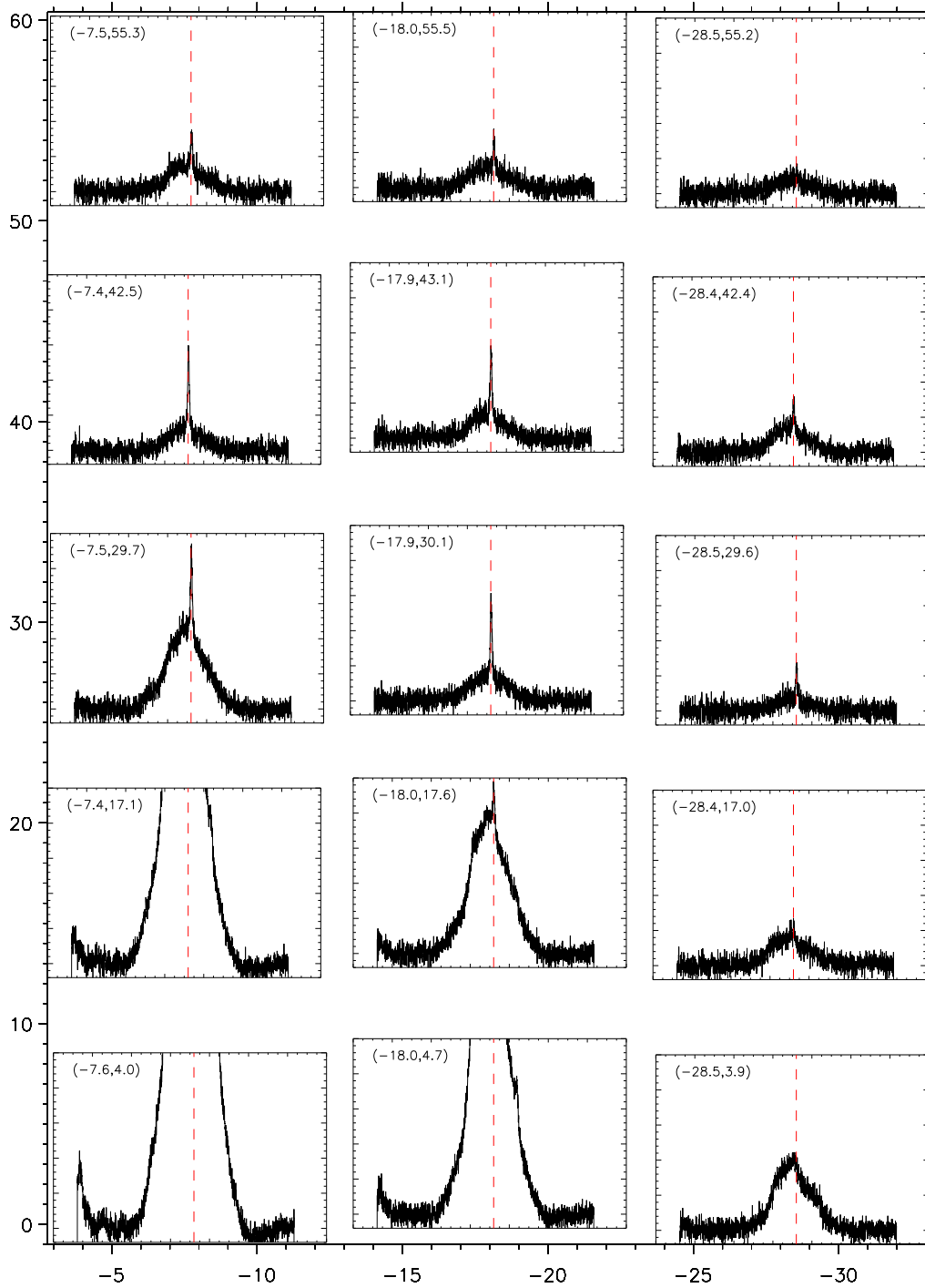


Fig. B.2.— Same as Figure B.1 but for dataset 6b-H in Table A.1.

Appendix C

Discussion on Pointing Errors

The source for the variability of the broad pedestal component in the 621 GHz spectral line requires explanation. More precisely, we need to determine whether some time-varying physical mechanism and/or pointing errors are responsible for the change that occurs in the pedestal between 2011 to 2012.

As the first and last set of observations involved a small map, we examined two possibilities. First, whether the increase in emission from the broad component is common to all areas of the map, and second, if not, whether there is a noticeable offset in the spatial positioning. Figures B.1 and B.2 illustrate the horizontally polarised versions of the two small maps taken during the first and last epochs of our observations. In Table A.1, this corresponds to observation numbers 2-H and 6b-H, respectively. From 2011 and 2012, the intensity of the maser line itself seems to systematically decrease between the maps of Figures B.1 and B.2. At the same time, in many panels toward the map center, the aforementioned broad component appears to get stronger. This trend differs at points farther from the center, where there is more of a decrease, especially in the line wings of the bottom left panels. This latter point seems to indicate systematic changes in the source. However, one possible explanation for the increase in the broad component may be due to the proximity

of the Orion “hot core” (HC) whose molecular line emissions were studied extensively by Beuther et al. (2005). The HC is located at (R.A.[J2000]= $05^{\text{h}}35^{\text{m}}14^{\text{s}}.50$, decl.[J2000]= $-05^{\circ}22'30''.45$) only about 6 arcseconds removed from Orion KL. It is displaced from our pointing direction by only $20''$ in Right Ascension and $30''$ in Declination, and thus lies at an offset of only 36 seconds of arc from our prime pointing direction. This small offset, barely exceeding the FWHM of our beam at 621 GHz, implies that even a relatively small error in pointing could effect a large apparent variability, given that the HC would lie on the flank of our beam profile.

In Section 2.3.2, we stated that the adjustment in the absolute pointing error (APE) improved the pointing accuracy of HIFI but retained some of its uncertainty. This is especially true of the mapped observations, which have additional pointing uncertainties due to relative offsetting and jitter, that may total $1''.5$ - $2''.5$ for OTF maps. Both mapping and pointed modes can be further misdirected from their intended pointing during telescope switching from OFF to ON source. Indeed the APE was verified during *Herschel* photometric operation and was never proven to exactly match while in spectroscopic observations. In general, HIFI has shown itself able to resolve source structure to better than $1''$ at its high-frequency end. Nevertheless pointing errors of order $3''$ have occasionally been observed on *Herschel*.

As we are combining data across several Observation Days, it is easy to conceive of pointing errors of this order. Together with the large source gradient shown in Figures B.1 and B.2 and the presence of the HC in the vicinity of our source, the effect of pointing errors must be considered a likely source of variability in the broad spectral component. Quantitatively, if one is to look more closely at, for example, Figure B.2, there is a drastic, ~ 1.5 K increase in the broad component as one moves $12''.5$ from the center position to that directly beneath. Following the discussion from above, a reasonable pointing error of $3''$, or 23% of the map step size, would thus correspond to an increase of ~ 0.35 K in the broad pedestal. An offset of this magnitude from

the center position would therefore result in the amplitude of the broad component rising to ~ 0.85 K, or ~ 1.7 times the intensity.

Appendix D

Polarization of HCN

In addition to the High-Resolution Spectrometer (HRS) mode, in which our 621 GHz data were obtained, the HIFI instrument, simultaneously collected data with a Wide-Band Spectrometer (WBS) at a frequency resolution of ~ 1 MHz and a bandwidth of 4 GHz at each polarisation (de Graauw et al. 2010). By far the strongest emission signature in the band is from the $J = 7 - 6$ transition of HCN (620.304 GHz). Figure D.1 shows an average of all spectra from both 2011 (black) and 2012 (red). While there is not the same drastic “broad component” variation noted in the H₂O 621 GHz line, we do see a $\sim 20\%$ increase in intensity at all points on the line. This may be a consequence of the same phenomenon that is occurring around 12 km s^{-1} for the 621 GHz water line.

A polarisation analysis was also attempted on the HCN line using data from all six epochs. Levels ranged from 10 – 20%, probably too strong to be due to the molecular GK effect. The HCN line is likely to be subject to variations similar to those that rendered a polarisation analysis of the broad component of the 621 GHz water line unreliable given our pointing errors. But this also underlines the advantage that maser lines present for such analyses (in view of their small spatial extent) and more firmly establishes the lack of polarisation measured in the 621 GHz maser line.

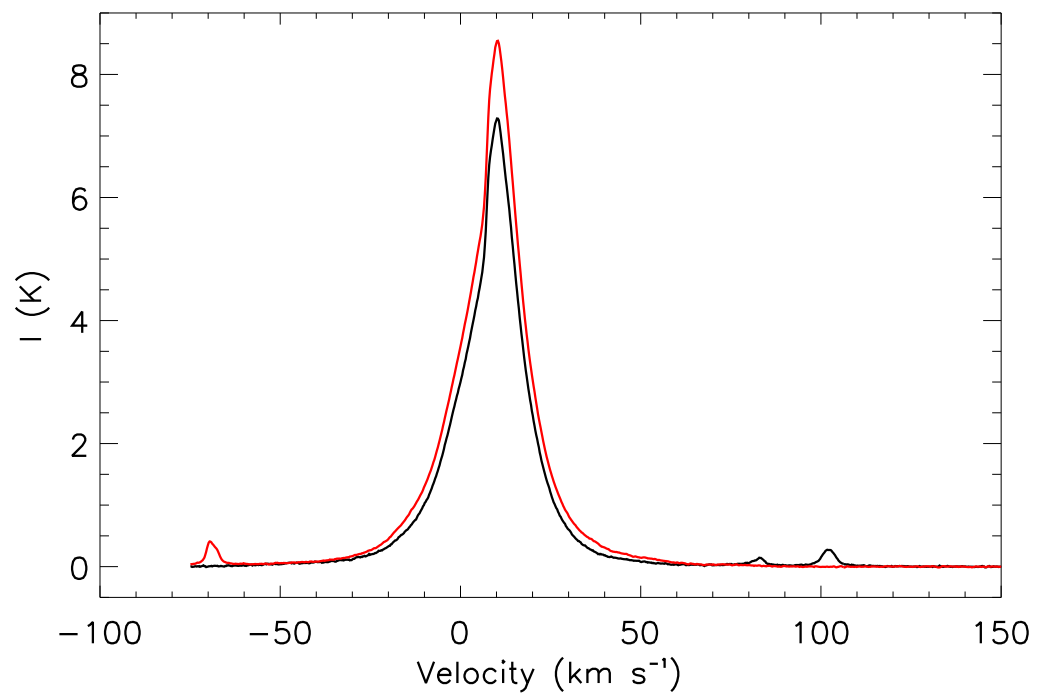


Fig. D.1.— Variation in the wide-band HCN spectrum from 2011 (black) to 2012 (red). Each spectrum represents an average of the three datasets from each year.

Vita

NAME: Scott Jones

PLACE OF BIRTH: Lethbridge, Alberta, Canada

YEAR OF BIRTH: 1986

POST-SECONDARY
EDUCATION AND
DEGREES:

Ph.D. in Astronomy

The University of Western Ontario
London, Ontario 2010-2015

M.Sc. in Physics

University of Lethbridge
Lethbridge, Alberta 2008-2010

B.Sc. in Physics

University of Lethbridge
Lethbridge, Alberta 2004-2008

RELATED WORK
EXPERIENCE:

Graduate Teaching and Research Assistant
The University of Western Ontario
2010-2014

Graduate Teaching and Research Assistant
University of Lethbridge
2008-2010

PUBLICATIONS:

- [1] Jones, S. C., Houde, M. and Hezareh, T. 2015, ApJ, to be submitted
“The Detection of Non-Zeeman Circular Polarization of CO Rotational Lines in OMC-2 FIR 4”
- [2] Jones, S. C., Houde, M., Harwit, M., Kidger, M., Kraus, A., M^cCoey, C., Marston, A., Melnick, G., Menten, K.M., Morris, P., Teyssier, D. and Tolls, V. 2014, A&A, 567, A31
“Polarisation observations of H_2O $J_{K_{-1}K_1} = 5_{32} - 4_{41}$ 620.701 GHz maser emission with Herschel/HIFI in Orion KL”
- [3] Houde, M., Hezareh, T., Jones, S. C., and Rajabi, F. 2013, ApJ, 764, 24
“Non-Zeeman Circular Polarization of Molecular Rotational Spectral Lines”
- [4] Naylor, D., ... (4), Jones, S. C., ... (39) 2010, A&A, 518, L117
“First Detection of the methylidine cation (CH^+) fundamental rotational line with the Herschel/SPIRE FTS”
- [5] Kirk, J.M., ... (5), Jones, S. C., ... (38) 2010, A&A, 518, L82
“Herschel-SPIRE spectroscopy of G29.96-0.02: Fitting the full SED”
- [6] Naylor, D., ... (8), Jones, S. C., ... (12) 2010, Proc. SPIE 7731, 773116
“In-orbit performance of the Herschel/SPIRE imaging Fourier transform spectrometer”

- [7] Abergel, A., ... (21), Jones, S. C., ... (23) 2010, A&A, 518, L96
“Evolution of interstellar dust with Herschel. First results in the photodissociation regions of NGC 7023”
- [8] Habart, E., ... (21), ..., Jones, S. C., ... (23) 2010, A&A, 518, L4
“SPIRE spectroscopy of the prototypical Orion Bar Photodissociation Region”
- [9] Swinyard, B.M., ... (21), Jones, S. C., ... (35) 2010, A&A, 518, L4
“In-flight calibration of the Herschel-SPIRE instrument”
- [10] Miville-Deschênes, M.-A., ... (23), Jones, S. C., ... (22) 2010, A&A, 518, L104
“Herschel-SPIRE observations of the Polaris flare: Structure of the diffuse interstellar medium at the sub-parsec scale”
- [11] Anderson, L.D., ... (24), Jones, S. C., ... (21) 2010, A&A, 518, L99
“The physical properties of the dust in the RCW 120 H II region as seen by Herschel”
- [12] Rodón, J.A., ... (26), Jones, S. C., ... (21) 2010, A&A, 518, L80
“Physical properties of the Sh2-104 H II region as seen by Herschel”
- [13] White, G., ... (26), Jones, S. C., ... (22) 2010, A&A 518, L114
“Herschel/SPIRE spectroscopy of the DR21 molecular cloud core”

[14] Naylor, D.A., Phillips, R.R., di Francesco, J., Bourke, T., Querel, R. and Jones, S. C. 2008, International Journal of Infrared and Millimeter Waves, 29, 1196

“IRMA as a Potential Phase Correction Instrument: Results from the SMA Test Campaign”